

# Aix-Marseille Université

## ED 353: SCIENCES POUR L'INGENIEUR

UFR Sciences

INSTITUT MATÉRIAUX MICROÉLECTRONIQUE NANOSCIENCES DE  
PROVENCE (IM2NP)/UMR CNRS 7334

Thèse présentée pour obtenir le grade universitaire de docteur

Discipline : MÉCANIQUE, PHYSIQUE, MICRO ET NANOÉLECTRONIQUE

Spécialité : Micro et Nanoélectronique

Katawoura BELTAKO

Transport résolu en temps dans les nanodispositifs  
optoélectroniques quantiques

Soutenue le 26/10/2018 devant le jury :

M. Nicolas CAVASSILAS  
Mme Fabienne MICHELINI  
M. Didier MAYOU  
Mme Alexandra OLAYA-CASTRO  
Mme Adeline CRÉPIEUX  
M. Philippe DOLLFUS  
M. Jean-François GUILLEMOLES  
M. Michel LANNOO

MCF-HDR - IM2NP Marseille  
MCF-HDR - IM2NP Marseille  
DR. CNRS - Institut Néel Grenoble  
MCF-HDR - University College London  
MCF-HDR - CPT- Marseille  
DR. CNRS - C2N Saclay  
DR. CNRS - Institut de photovoltaïque d'Ile de France  
DR Emérite. CNRS - IM2NP Marseille

Co-directeur de thèse  
Directeur de thèse  
Rapporteur  
Rapporteur  
Examineur  
Examineur  
Examineur  
Examineur



Cette oeuvre est mise à disposition selon les termes de la [Licence Creative Commons Attribution - Pas d'Utilisation Commerciale - Pas de Modification 4.0 International](#).

## RÉSUMÉ

Les récents progrès en matière de fréquences d'excitation au-delà du gigahertz offrent aujourd'hui la possibilité de sonder la réponse interne d'un système quantique. Résoudre le fonctionnement en temps des futurs composants de la nanoélectronique apparaît aujourd'hui comme le défi majeur de la prochaine avancée en matière de modélisation/simulation. Des tensions de grilles oscillantes, le régime transitoire de l'application d'une tension de polarisation, mais également des pulses d'illumination appliqués, sont des exemples de problématiques essentielles en simulation du transport quantique dans l'urgence de nouveaux angles d'approche autant que de méthodes numériques performantes. C'est le contexte de cette thèse, qui se concentre sur trois axes. Une première partie sur la méthodologie. Nous avons proposé une technique adaptée à la simulation du transport dépendant du temps dans les nanosystèmes interagissant avec un rayonnement lumineux, en nous appuyant sur l'état de l'art des méthodologies de statistiques quantiques avec une attention particulière au formalisme des fonctions de Green hors-équilibre. La deuxième partie de la thèse est consacrée au développement et à la mise en œuvre d'algorithmes efficaces pour simuler des fonctionnements résolus en temps de nanodispositifs optoélectroniques quantiques. Enfin, cette nouvelle méthode et les algorithmes développés nous ont permis d'étudier les processus de transfert de porteurs dans des nanojonctions moléculaires. Cette étude nous a conduit à l'élucidation d'effets physiques insoupçonnés et à des propositions expérimentales captivantes pour la détermination de caractéristiques quantiques internes de ces nanodispositifs. Ce travail nous fournit un outil précieux pour la simulation du transport quantique ultrarapide. Il donne également un aperçu de la pertinence de la dynamique transitoire dans la compréhension du fonctionnement des nanodispositifs optoélectroniques résolu en temps, et ouvre la voie vers la conception de l'optoélectronique ultrarapide.

## ABSTRACT

Recent advances in excitation frequencies beyond gigahertz now offer the ability to probe the internal response of a quantum system. Time dependence in future nanoelectronics has arisen as the major challenge of next advances in device modeling and simulations. Oscillating gate voltages, time-dependent bias but also applied illumination pulses, all are examples of key issues in quantum transport simulations which require novel approaches as well as efficient numerical methods. This is the context of this thesis, which focuses on three areas. A first part concerns the methodology. We proposed a suitable technique to the simulation of time-dependent transport in nano-systems interacting with light radiation, relying on the state of the art in quantum statistical methodologies, with a special attention to the formalism of non-equilibrium Green's functions. The second part of the thesis is devoted to the development and implementation of efficient algorithms to simulate time-resolved quantities for quantum optoelectronic nanodevices. Finally, this new method and the developed algorithms have enabled us to investigate carrier transfer processes in molecular nanojunctions. This study led us to the elucidation of unsuspected physical effects and captivating experimental proposals for the determination of internal quantum characteristics of these nanodevices. This work provides us with a valuable tool for ultrafast quantum transport simulation. It also gives indeed an insight on the relevance of transient dynamics in the understanding of time-resolved optoelectronic nanodevice operations and open avenues towards the design of future ultrafast optoelectronics.

## ACKNOWLEDGEMENT

I would first like to thank my thesis advisor Dr. Fabienne Michelini, Maître de Conférence, at Aix Marseille University. My research and writing would have been impossible without the support and guidance of Dr. Fabienne Michelini. She consistently allowed this thesis to be my own work but steered me in the right direction whenever she thought I needed it.

I would also like to thank my thesis co-advisor Dr. Nicolas Cavassilas, Maître de Conférence, at Aix Marseille University. The door of Dr. Nicolas Cavassilas office was always open whenever I needed help or had a question about my research or writing.

My sincere thanks to DR. Michel Lannoo, Professeur Emérite at Aix-Marseille University, for interesting discussions on excitons in molecules.

I would also like to acknowledge Dr. Elsie Laban Yekwa from Seattle and M. Benjamin Amoah from Lancaster University as readers of this thesis, and I am grateful for their valuable comments on this thesis.

Finally, a heartfelt thanks to my parents and to my spouse for providing me with unfailing support and continuous encouragement throughout my years of study and through the process of researching and writing this thesis. This accomplishment would not have been possible without them. Thank you.

# CONTENTS

<b>Résumé</b>	<b>3</b>
<b>Abstract</b>	<b>4</b>
<b>Remerciements</b>	<b>5</b>
<b>List of Figures</b>	<b>8</b>
<b>List of Tables</b>	<b>10</b>
<b>1 Introduction</b>	<b>11</b>
1.1 Motivation	11
1.2 Ultrafast molecular optoelectronics	11
1.3 Time-dependent many-body methods	13
1.4 Photocurrent spectroscopy	14
1.5 Thesis overview	14
<b>Introduction</b>	<b>15</b>
<b>2 Transport equations and Algorithms</b>	<b>16</b>
2.1 Nonequilibrium Green's function formalism	17
2.1.1 Schrodinger's wave and Green's function	18
2.1.2 Quantum mechanical operators and representations	19
2.1.3 Constructing Green's functions	23
2.1.4 Equation of motion theory	27
2.2 Wave function technique : ballistic transport	28
2.2.1 Schematic description	28
2.2.2 Constructing wave functions	30
2.3 Wave function technique : bound electron-hole pair correlations	33
2.4 Algorithms and numerics	37

<b>3</b>	<b>Dynamical level structure and Photo-induced charge current in organic semiconductor devices</b>	<b>40</b>
3.1	Device structure	41
3.2	Population dynamics	43
3.3	Photocurrent generation	45
3.4	Ultrafast electronic structure dynamics	49
3.5	Proposal of experimental measurement	53
3.5.1	Intramolecular couplings and terahertz frequencies	53
3.5.2	Rabi dynamics and tunneling competition	54
3.6	Discussion	58
<b>4</b>	<b>Driving energy and Ultrafast bound electron-hole pair dynamics</b>	<b>61</b>
4.1	Impacts of electron-hole Coulomb interaction	63
4.1.1	Model and method	63
4.1.2	Impact on time-resolved local density of states	65
4.1.3	Impact on the photocurrent	66
4.2	Analyzing charge transfer	68
4.2.1	Positioning of the study	69
4.2.2	Dynamical driving energy and exciton binding	69
4.2.3	Characteristic timescales of charge transfer	73
4.2.4	Proposal for measuring of the driving energy	76
4.2.5	Conclusions for molecular junction design	77
4.3	Two-pulse photocurrent simulations	78
4.4	Discussion	81
	<b>Conclusion</b>	<b>84</b>
	<b>Bibliographie</b>	<b>85</b>
	<b>ANNEXES</b>	<b>97</b>
A	TRLDOS stationary limit	97
B	List of publications	98

## LIST OF FIGURES

1.1	Donor-acceptor molecular junction, and exciton versus charge transfer dynamics. HOMO= The highest occupied molecular orbital and LUMO=the lowest energy unoccupied molecular orbital.	12
2.1	System described by a Green function of size $N \times N$ for $m$ incoming modes.	29
2.2	System described by wave functions of size $N \times 1$ for $m$ incoming modes.	29
3.1	Vibrational modulation effect. The vibrational part of the photocurrent pump push spectroscopy response, measured at negative delay time from [93].	41
3.2	Schematic representation of the molecular junction. Energies $\varepsilon_1$ and $\varepsilon_2$ are the atomic orbitals of the donor and $\varepsilon_3$ the LUMO orbital of the acceptor.	42
3.3	Pulse-induced light-donor coupling, $M(t)$ , as a function of time (left panel). Fast Fourier transformed signal of the pulse (right panel).	43
3.4	Populations $n_1$ of donor level 1, $n_2$ of donor level 2, $n_3$ of acceptor level 3. Simulation parameters are $\beta = 0.1$ eV, $\Gamma = 0.05$ eV, and $A_0 = 0.5$ eV.	45
3.5	Time-resolved photocurrent expressed in ampere. Simulation parameters are $\beta = 0.1$ eV, $\Gamma = 0.05$ eV, and $A_0 = 0.5$ eV. (A) with the same parameters as in Figure 3.4, (B) except that $\beta = 0.3$ eV instead of 0.1 eV, (C) except that $\Gamma = 0.2$ eV instead of 0.05 eV, and (D) except that $A_0 = 0.05$ eV instead of 0.5 eV.	46
3.6	Time-resolved photocurrents maps: as function of $\beta$ (left panel), and pulse amplitude $A_0$ (right panel), with $\Gamma = 0.05$ eV.	48
3.7	Photocurrent showing three dynamical regions: Raising dynamic (Zone A), Forced dynamic (Zone B) and Damped oscillations dynamics (Zone C).	48



3.8	Time-resolved local (donor) density of states at the donor (in logarithm scale). Simulation parameters are $\beta = 0.1$ eV, $\Gamma = 0.05$ eV, and $A_0 = 0.5$ eV.	50
3.9	(a) Sketch of the dynamical Rabi sidebands. (b) Traces of local maxima of time-resolved local density of states extracted from figure 3.8.	51
3.10	Instantaneous local (donor) density of states for different times ( $t_0 = 10$ fs, $t_1 = 25$ fs, $t_2 = 30$ fs, $t_3 = 35$ fs and $t_4 = 60$ fs), with the same parameters as in figure 3.4.	52
3.11	Proposal of experimental measurement of $\Gamma$ and $\beta$ from off pulse photocurrent (a) exponential fit: $\exp(-0.03 * t/\hbar)$ for $\Gamma = 0.03$ eV, (b) FFT of the off pulse photocurrent for $\beta = 0.1$ eV.	54
3.12	Energy level splitting. For values of $\Gamma$ above the $\Gamma_0$ line, the splitting of the energy level is no more visible. Parameters are $\beta = 0.1$ eV and $A_0 = 0.5$ eV.	55
3.13	Time-resolved local (donor) density of states. For values of $\Gamma = 0.05$ eV (left panel) and $\Gamma = 0.25$ eV (right panel).	55
3.14	Limit values $\Gamma_0$ as function of $\beta$ for two values of the pulse amplitude.	56
3.15	Diagrammatic picture of the internal electronic structure dynamics inside the D-A molecular junction.	57
3.16	Simulated infrared (IR) spectrum for the pentacene molecule (red) and crystal (blue), superimposed on the experimental spectrum for comparison from [93].	57
3.17	Results of pump-push photocurrent experiments on a set of organic photovoltaic [105]. In this plot $\delta PC/PC$ is the same as $dJ/J$ in 3.1.	59
4.1	Interactions that play a role in organic semiconducting junctions. Pentacene donor and fullerene acceptor from [112].	63
4.2	Donor-acceptor junction including coulomb correlations; $\varepsilon_1$ and $\varepsilon_2$ are the atomic HOMO and LUMO of the donor, and $\varepsilon_3$ the LUMO orbital of the acceptor.	64
4.3	Time-resolved local (donor) density of states: $\chi_{ct} = 0$ eV (a) and $\chi_{ct} = 0.3$ eV (b) with $\chi_{ex} = 0.0$ eV.	65
4.4	Time-resolved local (donor) density of states.	66
4.5	Time-resolved photocurrent for $\chi_{ct} = 0.0, 0.3$ and $0.6$ eV with exciton coupling $\chi_{ex} = 0$ eV.	67
4.6	Time-resolved photocurrent for $\chi_{ex} = 0.0, 0.3$ and $0.6$ eV with CT coupling $\chi_{ct} = 0.0$ eV.	67
4.7	Time-resolved photocurrent: exciton and CT state competition with $\chi_{ex} = 0.3$ eV.	68

4.8	CT state and exciton competition seen through energy level corrections. The three left panels ( $\varepsilon_1^{HF}, \varepsilon_2^{HF}$ and $\varepsilon_3^{HF}$ ) represent the time-dependent corrected energy levels induced by e-h pair coupling on $\varepsilon_1, \varepsilon_2$ and $\varepsilon_3$ orbitals. The three right panels ( $\Delta\varepsilon_1^{HF}, \Delta\varepsilon_2^{HF}$ and $\Delta\varepsilon_3^{HF}$ ) are the corresponding energy corrections. We take $\chi_{ex} = 0.3$ eV.	70
4.9	Time-resolved driving energy $\Delta\varepsilon_{32}^{HF}$ for $\chi_{ex} = 0.3$ eV.	71
4.10	Time-resolved photocurrent as a function of LUMO energy offset, $\delta_{DA}$ , for $\chi_{ct} = 0.1$ eV and 0.3 eV, with $\chi_{ex} = 0.3$ eV.	72
4.11	Integrated photocurrent as a function of LUMO energy offset, $\delta_{DA}$ , for $\chi_{ct} = 0.1$ eV and 0.3 eV with $\chi_{ex} = 0.3$ eV	73
4.12	Populations $n_i$ and product distribution $(1 - n_1)n_i$ as a function of time for three different values of $\chi_{ct}$ . Parameter $\chi_{ex}$ is set to 0.3 eV.	74
4.13	Evolution of the photoinduced interfacial electron transfer time, $\tau_{tr}$ , as function of $\chi_{ct}$ , with $\chi_{ex}$ set to 0.3 eV.	75
4.14	Lifetime of CT state, $\tau_{lifetime}$ , as function of $\chi_{ct}$ , with $\chi_{ex} = 0.3$ eV.	75
4.15	Time-resolved photocurrent distribution as function of the gaussian pulse central energy, $\hbar\omega$ for different $\chi_{ct}$ with $\chi_{ex} = 0.3$ eV.	76
4.16	Integrated photocurrent as function of the gaussian pulse central energy, $\hbar\omega$ .	77
4.17	Photocurrent response to a sequence of two pulses for different delays, $\tau_{del}$ , with $\chi_{ct} = 0.1$ eV and $\chi_{ex} = 0.3$ eV .	79
4.18	Maps of the time-resolved photocurrent as function of the delay, $\tau_{del}$ , for two values of $\chi_{ct}$ , with $\chi_{ex} = 0.3$ eV.	80
4.19	Direct current, $I^{dc}$ , for different $\chi_{ct}$ values, with $\chi_{ex} = 0.3$ eV.	81
4.20	Fast Fourier Transform (FFT) of $I^{dc}$ oscillatory part.	81

## LIST OF TABLES

3.1	Comparison of input value $\beta$ to the numerical value extracted from FFT.	53
-----	--	----

## INTRODUCTION

### 1.1. Motivation

The motivation of this work lies in the possibility of controlling electronic, ionic, spin and orbital degrees of freedom of electrons at sub-picosecond time scales for application in ultrafast optoelectronics, and quantum computation and information. The underlying question is how to understand and control the intricate properties of matter, molecules and finally nanodevices that emerge from complex correlations in their internal structure and on their internal time scales? And how could we characterize and control these nanosystems, especially when they are far from equilibrium, where high performances are expected?

Recent striking theoretical and experimental advances in the understanding of nanosystems interacting with light such as carbon nanotubes, organic and/or inorganic hybrid, biological light conversion systems together with the progress in cryogenic technology and ultrafast transient absorption, have generated considerable interest for high-frequency quantum transport in the perspective of ultrafast optoelectronic nanodevices [1–4].

Due to their ultrafast response time, low cost, efficiency, and flexible nature, molecular electronics form a promising alternative for the design of such nanodevices.

### 1.2. Ultrafast molecular optoelectronics

One of the earlier proposals in the ac field was a single-molecule rectifying diode in 1974 by Ratner and Aviram [5]. Since then the field has attracted continued interest from scientists. The first coherent theory of charge transfer in molecular systems was formulated by R. A. Marcus [6], which led to his Nobel prize in 1992. This accomplishment opens the pathway to various experiment and realization made in order to probe the response of electronic devices driven by an

external time-dependent field, such as charge transfer processes in general. Few realizations are the controllable single-molecule junction [7, 8], the coherent single electron source [9, 10] and laser-driven electronic dynamics on a time scale of  $\sim 1$  fs experimentally observed, establishing the possibility to control charge dynamics in nanodevices on their internal time scale.

In single-molecule devices such as switches, pumps, and rectifiers, where charge and energy transfer processes are driven by an external time-dependent radiation field, several complex phenomena are involved: molecular orbital reorganization, destruction of molecule-lead and donor-acceptor tunnel coupling [11–13]. It has been recently found that the initial charge transfer process is ultrafast, on the timescale of tens of femtoseconds [14], or at least ranging from a few femtoseconds to hundreds of picoseconds for photoinduced interfacial electron transfer processes [15].

Intramolecular transfer processes remain a hot debate among the existing open questions of the field, schematically illustrated in Figure 1.1.

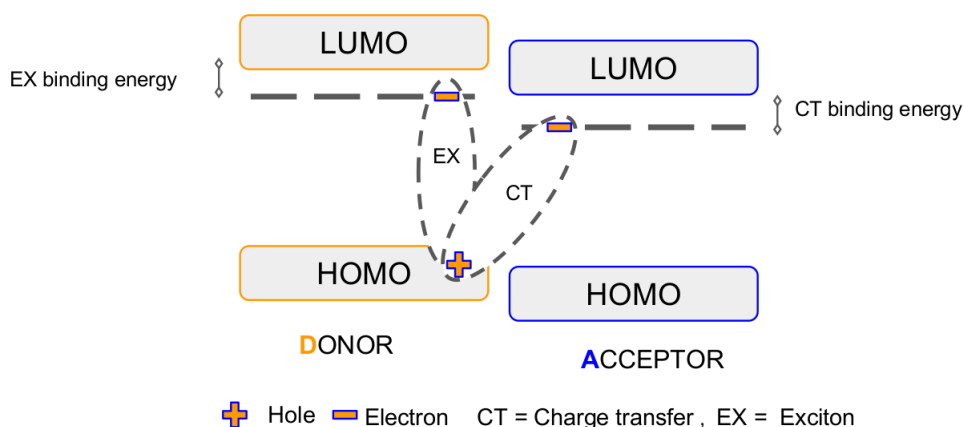


Figure 1.1.: Donor-acceptor molecular junction, and exciton versus charge transfer dynamics. HOMO= The highest occupied molecular orbital and LUMO=the lowest energy unoccupied molecular orbital.

The commonly accepted picture is the following. After a photon energy is absorbed in the material or molecule, usually the donor, a bound electron-hole pair, here regarded as an exciton (EX), is created, due to the low dielectric constant in a molecule, there is a weak dielectric screening of the Coulombic attraction of electrons in the LUMO and holes in the HOMO. The photoinduced exciton migrates to the donor-acceptor interface, where the electron could be transferred to the acceptor and then the reservoirs if the ionization potential of the donor is smaller compared to the electron affinity of the acceptor. In the former configuration with the electron and hole still bounded by the Coulomb potential, the

electron-hole pair is considered to be a charge transfer (CT) state. The interface charge transfer and separation process is still not well understood in the community of organic and molecular device. And it is a really important step towards the improvement of the efficiency of organic solar cells.

Efficient time-resolved numerical simulations are thus required, as perhaps the most powerful tool to understand, predict and conquer the basics of electron-hole pair generation and charge transport on the relevant time scales for an efficiency improvement of these THz and ultrafast nanodevices.

### 1.3. Time-dependent many-body methods

Indeed, time-dependent numerical investigations may offer a flexibility to promote the realization of nanodevices. Various temporal dependence of interacting potentials as oscillating gate voltages and time-dependent coupling modulations could be included into nanodevice simulations [16, 17]. This allows the description of time-resolved physical quantities; transient currents, the local density of states, structural and vibrational dynamics, and the investigation of the nanosystem internal quantum properties, hence the optimization and design of a novel type of nanodevices. One can deal with time-dependent external fields, like light pulse effects on the transport characteristics, and thus investigate ultrafast photo-induced and photo-assisted transport mechanisms [18, 19]. Time-dependent quantum transport simulations requires novel techniques as well as efficient numerical methods.

These last decades have seen the achievement of theories that account for mesoscopic quantum transport in the presence of a time-dependent field-induced perturbation [20, 21]. From Floquet theory for periodically (often monochromatic) driven systems [22, 23] to rigorous quantum-based non-equilibrium Green's functions [24, 25], a wide range of theories have been proposed. Scattering theory [26, 27], reduced density matrix approach [28, 29] and more generally *ab initio* methods are also used. The main theoretical approaches used to tackle time-dependent many-body problems are: Ehrenfest molecular-dynamics (MD), time-dependent density functional theory (TDDFT) [30], path integral for quantum transport [31], master equation approaches [32], and non-equilibrium Green's functions in time domain [33–35].

*Ab initio* methods like density functional theory (DFT and TDDFT) [36–39] even though offer a potential computational scheme, are not appropriate for the treatment of time-dependent field-induced polarization effects like Coulomb blockades [40] or dynamical energy level renormalization [41].

The Non-equilibrium Green's function formalism (NEGF), on which relies this thesis, represents one of the most exact approaches to quantum transport [42], as recently shown in the study of pump-probe shot noise spectroscopy [43] and the treatment of plasmon-exciton coupling [44]. One strong property of NEGF

formalism is indeed to treat exactly the coupling to the reservoirs, in contrast with master equations, which is an essential property in order to study quantum transport. It nonetheless suffers from the heavy computational cost for realistic simulations of time-dependent problems. Derived from NEGF formalism, the wave function technique, referred as NEGF-WF in this thesis, was recently proposed as an efficient algorithm to numerically simulate time-resolved quantum transport in inorganic, organic and hybrid nanodevices [45].

## 1.4. Photocurrent spectroscopy

Finally, time-dependent numerical investigations also afford the possibility to develop highly resolved ultrafast scanning probes, designed to explore ultrafast electron dynamics of solids and organic semiconductors [46–49]. Among them, one of the most recently developed techniques, the *photocurrent pump-probe spectroscopy*, lies at the meeting point of two research fields: nonlinear optical spectroscopy and quantum transport. Indeed, this hybrid spectroscopy combines ultrafast optical and electronic techniques to probe carrier dynamics and interactions in optoelectronic devices [50]. The idea of measuring the internal ultrafast dynamics of molecular junctions through photocurrent, instead of emission [51], has shown to reveal underlying physics of molecular junctions, as the key process of charge transfer and separation at interfaces [52, 53] also involved in energy conversion. Indeed, time-dependent investigations bring new perspectives for high conversion efficiency for solar cells with molecular blends, as suggested by numerical simulations using quantum dots or bulk heterojunctions as models [54, 55]. Further issues to be handled in this direction will be energy transfer and entropy production [56], molecular vibrations, and electron-hole interactions [57, 58].

## 1.5. Thesis overview

In this overarching context, the present thesis addresses several questions. the clarification of the charge transfer at metal-molecule and molecule-molecule interface, the correlation of the photocurrent directionality [59] to the field shape and the internal molecular structure and the intimate nature of such quantum systems, provided features of their electronic structure [60, 61], and energy level dynamics [62].

This thesis work has required to set up a suitable approach to the quantum simulation of time-resolved transport in interacting nanosystems under an externally applied time-dependent field radiation. The theory relies on the state of the art in quantum statistical methodologies with a special attention to the formalism of non-equilibrium Green’s functions [33] widely used for the stationary quan-

tum device simulation [63, 64]. Electron-electron and electron-hole correlations have been introduced as an improvement of the existing nanoelectronics simulation tools in the time domain. This theoretical-numerical simulation should be valuable for deeply understanding charge transport through molecular junctions, and hence, for conducting relevant device design and future directions of molecular electronics [65, 66]. Our investigations focus on donor-acceptor organic semiconducting nanodevices, but discussions open wider on molecular junctions and nanosystems in general.

This manuscript is thus organized as follows:

- In Chapter 2, we focus on the theoretical background of the NEGF based Wave Function technique employed in this thesis. The WF technique in its original form as proposed in reference [45] does not include any kind of interaction. An extension of the WF technique to interacting systems is proposed here, especially the treatment of electron-electron and electron-hole correlation at Hartree-Fock level. Chapter 2 ended up with few algorithms for the numerical implementation of the WF technique and its extended form.
- In Chapter 3, we present an example of an application of the methodology to a non-interacting molecular junction under femtosecond laser pulse illumination. Several physical effects are studied and experimental proposals are made for the measurement of donor-acceptor bridge strength.
- In Chapter 4, we analyze the additional effect of an exciton generated in the donor and charge transfer state at the donor-acceptor interface on the driving energy and their competition in the nanosystem. Finally, the first results on two-pulse photocurrent spectroscopy are proposed.

## TRANSPORT EQUATIONS AND ALGORITHMS

This chapter is devoted to the theoretical technique used in this thesis. Charge transfer through nanoscale junctions and interfaces are complex dynamical processes. Accurate description relies on simultaneously accounting for multiple effects on ultrafast time scales that take into account internal time scales of the system. In molecular junctions, for instance, the complexity is led by the contacts to the electrodes, as well as the simultaneous interplay of Coulomb electron-electron repulsion, electron-hole attraction or exciton and lattice vibration effects, which makes molecular electronics field an interdisciplinary research. Theoretical and numerical treatment of all these correlation effects [67] based on mean field approximation gives good physical models.

Let us recall the idea of the standard mean-field approximation, on which our theory is based. Interacting particles physics is very complicated because of the correlated motions of the individual particles that depend on each other. However, there are several rough approximations, where not full correlations are included, but which gives a good physical result. For instance, when correlations are included not by accounting for individual particle correlation but *the average* correlation of all particles, in such a way that the density, for instance, is included as *mean density*, it raises the idea of *mean field approximation* used here. Mean field approximation reduces a many-body problem to a one body problem. This approximation gives the overall framework of how we treat the light-matter interaction (laser-donor for instance) in this work. Then we have to choose a method to handle the transport.

The commonly used master equations are limited to the weak system-lead coupling regimes [16]. For weakly coupled molecule-electrode for instance, the results obtained by the density matrix approach are often found to be in agreement with the nonequilibrium Green's functions formalism (NEGF) simulation results.

There is also the time-dependent extension of density functional theory (DFT), with its approximations based at present, like others *ab initio* methods, unrefined



to capture some correlation effects like field-induced energy levels renormalization. In fact even though DFT combined with NEGF (NEGF-DFT) is popular for modeling and has shown successful result for metallic contacts and chemisorbed molecules [68, 69], it does not only scale as the size of the system in the computation, but also it overestimates the quantum conductance compared to experiment in weakly coupled systems [70, 71]. The conflict might come from the unsuitable choice of exchange-correlation functionals [72] or the not fully justified application of ground state DFT to non-equilibrium transport [73].

One of the best promising alternatives is NEGF formalism that offers the possibility to treat previously mentioned correlations processes. NEGFs have shown to be powerful and made its proof in transistors, solar cells, and switches simulation [74, 75]. Although NEGF approach is exact and allows to include most of the needed correlation effects, it remains time and memory consuming for direct integration of NEGF transport equation, especially in its time-dependent extension. In the quest for alternatives, a proposal was made by **B. Gaury** [45]. The technique is called *Wave Function (WF)*, but it is denoted nonequilibrium Green's functions formalism-Wave Function (NEGF-WF) in this manuscript to outline close connection to NEGF in the derivation.

The first part of the chapter is devoted to the description of nonequilibrium Green's functions formalism starting from the basis of quantum mechanics. The second part revisits the NEGF wave function technique in its foundations for ballistic quantum transport. The third part will focus on our proposal for the treatment of electron-electron and electron-hole correlations with included efficient algorithms for numerical implementation of the technique.

## 2.1. Nonequilibrium Green's function formalism

Briefly, Green's functions are physical building blocks that are used to describe particle transport in mesoscopic systems. Green's functions are very useful in the theory of ordinary and partial differential equations. In physics, Green's functions are particularly useful for problems involving perturbed systems. When the problem under consideration is described by many-particles, whether electron, phonon, or spin interacting with a bath of other particles, its exact solution is hard to find, especially when the whole system is out of equilibrium due to an external field. NEGF formalism that originates from the seminal works of Martin and Schwinger (1959), Kadanoff and Baym (1962), Keldysh (1965) [76], is one of the most exact approaches to describe quantum transport in interacting and non-interacting systems. Before the introduction of the many-body Green's function in the next section, we first discuss the case of non-interacting particles with and without time dependence in the case of one-particle Schrodinger equation. Next, we introduce quantum mechanical concepts for Green's functions description. Finally, we derive the equation of motion of Green's functions, which are in

fact the propagator of quantum states. Let us recall here that these derivations, follows the usual ones in standard textbooks [33, 76].

### 2.1.1. Schrodinger's wave and Green's function

In this section, we give an overview of how to construct a Green function starting from Schrödinger's equation wave function while considering external perturbations and scattering mechanisms in the stationary case. We will basically follow the derivation from the various pedagogical textbooks in the field of mesoscopic physics [77, 78]. Let us consider the time-independent Schrödinger's equation in matrix representation, describing a given system,

$$H\Psi = E\Psi, \quad (2.1)$$

where  $H$  is the Hamiltonian matrix which eigenvalues are the allowed energies in the given system, and  $\Psi$  the wave function (corresponding eigenvector of equation 2.1). The description of electronic devices can be treated within a one-electron picture by connecting the given system described by Schrödinger equation 2.1) to electrodes. The perturbation induced by these electrodes to the system is taken into account by adding two terms to the Schrödinger equation, accounting for the inflow and outflow from the electrodes [78]:

$$H\Psi + \overbrace{\Sigma\Psi}^{outflow} + \overbrace{s}^{inflow} = E\Psi. \quad (2.2)$$

$\Sigma\Psi$  and  $s$  are the source terms in the system and in the electrodes.  $\Sigma$  is called the retarded self-energy of the reservoirs and also noted  $\Sigma^r$ . Solving this modified Schrödinger equation gives wave function solutions of the form,

$$\Psi = \frac{s}{EI - H - \Sigma^r}, \quad (2.3)$$

with  $I$  is the identity matrix.

Let us set from here on, an object that represents the building block of the transport formalism, a Green's function.

$$G^r = [EI - H - \Sigma^r]^{-1} \Rightarrow \Psi = G^r s. \quad (2.4)$$

$G^r$  is called the retarded Green's function. The real and imaginary parts of  $\Sigma^r$  are respectively the energy level shift and the energy level broadening functions. This last quantity  $\Gamma = i[\Sigma - \Sigma^\dagger]$  is usually considered to be the carrier tunnelling rate (or the hopping parameter) from the lead to the nanojunction. Next step is to construct the object  $\Psi\Psi^\dagger$ , that will give us information on wave function probabilistic distribution and coherence. From  $\Psi\Psi^\dagger$  we can extract carrier density in the device.

We set here another Green's function, that is also important for carrier density measurement,

$$G^< = \Psi\Psi^+ \quad \text{and} \quad \Sigma^< = ss^\dagger, \quad (2.5)$$

where  $G^<$  and  $\Sigma^<$  are respectively the lesser Green's function and the lesser self-energy accounting for carrier distributions and inflow control. Since,

$$G^< = G^r ss^\dagger G^{r\dagger} \iff G^< = G^r \Sigma^< G^a. \quad (2.6)$$

From the previously defined Green's functions, the density of states also called the spectral function,  $A$ , could be built as follow.

$$A = i[G^r - G^a]. \quad (2.7)$$

The deep nature of NEGF is contained in the equations 2.4 and 2.6. Solving these equations together allows getting carriers to transport pieces of information. However, the barrier to the implementation of these equations arises when there are scattering mechanisms (electron-boson, Coulomb and vibrations) in the system during carriers transport. In fact whenever there are scattering mechanisms, the self-energies ( $\Sigma^<$  and  $\Sigma^r$ ) are modified and depend on the Green's functions ( $G^r$  and  $G^<$ ) in such a way that self-consistent approximations (Self consistent Born approximation) are needed to solve equations 2.4 and 2.6. Though these numerical implementation challenges are handled for stationary transport in a certain limit [79], they are less evident for time-dependent cases.

For simplicity only the time-independent case is discussed here, however a similar derivation could be used for the time-dependent version too, and further development is given below.

In the next section, we will work out single-particle Green's function for many body systems. Let us start with the description of quantum mechanics operators involved in the derivation of these Green's functions.

## 2.1.2. Quantum mechanical operators and representations

Green's function formalism is raised from the interaction representation of quantum mechanics, described in the following. Relevant concepts of quantum mechanics are discussed: Schrödinger's, Heisenberg's and Interaction representation. We assume that the reader is familiar with quantum mechanics at least in its basis [76, 77].

### 2.1.2.1. Schrödinger's representation

The basis of quantum mechanics is taught in Schrödinger's representation, in which particles are described by wave function. The evolution of this wave function is given by the time-dependent Schrödinger's equation given below (we

assume here  $\hbar = 1$ ),

$$i\frac{\partial}{\partial t}\Psi(t) = H\Psi(t), \quad (2.8)$$

where  $\Psi(t)$  is the wave function of the given system. Solving the equation 2.8 gives solutions of the following nature:

$$\Psi(t) = e^{-iHt}\Psi(0). \quad (2.9)$$

The characteristics of these solutions in equation 2.9 are that their time dependency is encoded in the exponential factor ( $e^{-iHt}$ ), and all operators are time independent.

### 2.1.2.2. Heisenberg's representation

The Heisenberg's representation of quantum mechanics requires that the wave functions are time-independent and the operators time dependent. It operators are expressed as follows:

$$O(t) = e^{iHt}O(0)e^{-iHt}. \quad (2.10)$$

### 2.1.2.3. Interaction representation

In this representation, both operators and wave functions are time dependent. The Hamiltonian of the system is written as follow:

$$H = H_0 + V. \quad (2.11)$$

The  $H_0$  stands for the solvable or unperturbed part of the Hamiltonian and  $V$  the interactions part. Operators and wave functions are denoted by a hat in this representation:

$$\hat{O}(t) = e^{iH_0t}Oe^{-iH_0t}, \quad \text{and} \quad \hat{\Psi}(t) = e^{iH_0t}e^{-iHt}\Psi(0). \quad (2.12)$$

The need of many-body theories comes from the fact that  $H_0$  does not commute with  $V$  as such the relation  $e^Ae^B = e^{A+B}$  for instance cannot be used.

One can prove that the three representations of quantum mechanics are equivalent. For a system changing state from state 1 to state 2, the average value of a physical observable has the same value in the three representations.

#### 2.1.2.4. Time evolution operator

Accessing the wave function  $\hat{\Psi}(t)$  of a system from a given initial state  $\hat{\Psi}(t_0)$ , enables the computation of physical observables at each time  $t$ . The computation of  $\hat{\Psi}(t)$  can be done through the rate equation of the wave function within the interaction representation:

$$\begin{aligned}
 \frac{\partial}{\partial t} \hat{\Psi}(t) &= iH_0 \hat{\Psi}(t) - ie^{iH_0 t} H e^{-iH t} \Psi(0) \\
 &= iH_0 e^{iH_0 t} e^{-iH t} \Psi(0) - ie^{iH_0 t} H e^{-iH t} \Psi(0) \\
 &= ie^{iH_0 t} (H_0 - H) e^{-iH t} \Psi(0) \\
 &= -i \underbrace{e^{iH_0 t} V e^{-H_0 t}}_{\hat{V}(t)} \underbrace{e^{-H_0 t} e^{-iH t} \Psi(0)}_{\hat{\Psi}(t)} \\
 \frac{\partial}{\partial t} \hat{\Psi}(t) &= -i \hat{V}(t) \hat{\Psi}(t).
 \end{aligned} \tag{2.13}$$

Setting  $U(t) = e^{iH_0 t} e^{-iH t}$  as the *evolution operator*, such that the wave function is obtained by  $\hat{\Psi}(t) = U(t) \Psi(0)$  (with  $\Psi(0)$  the wave function at time  $t = 0$ ) and  $U(0) = 1$ , the evolution equation of  $U(t)$  could be derived from equation 2.13:

$$\frac{\partial}{\partial t} U(t) = -i \hat{V}(t) U(t). \tag{2.14}$$

One way of solving the equation 2.14, is to integrate both sides of the equation with respect to time:

$$U(t) - 1 = -i \int_0^t dt_1 \hat{V}(t_1) U(t_1). \tag{2.15}$$

By iterating over the right hand side of equation 2.15 an infinite number of time one get for  $U(t)$ :

$$U(t) = \sum_{n=0}^{\infty} (-i)^n \int_0^t dt_1 \int_0^{t_1} dt_2 \dots \int_0^{t_{n-1}} dt_n \hat{V}(t_1) \hat{V}(t_2) \dots \hat{V}(t_n). \tag{2.16}$$

Note that in the expansion of equation 2.16, the operators are time-ordered. In their product the operators at earlier times are at the left of operators at later times. We then define an operator  $T$  such that when applied to a product of two operators it will return their time-ordered product:

$$T(A(t)B(t')) = \begin{cases} A(t)B(t') & \text{if } t < t', \\ B(t')A(t) & \text{if } t' < t. \end{cases}$$

Now we can rewrite the expression of equation 2.16 in a more compact way. We replace the limits of each interval so that they span the whole duration  $t$

and we divide by  $n!$  to take into account that we integrate over a larger interval. Then we can write the products of integrals as powers and use the time-ordering operator to take this change into account and recognize the expression for an exponential as follows [76]:

$$U(t) = Texp \left[ -i \int_{t'}^t dt_1 \hat{V}(t_1) \right] \quad (2.17)$$

Another important operator to define before the introduction of Green's function is the S-matrix.

### 2.1.2.5. S-matrix

The S-matrix is in some sense the object (operator) that connects two quantum states picked at different times in the interaction representation. Let us consider two quantum states  $\hat{\Psi}(t)$  and  $\hat{\Psi}(t')$  at times  $t$  and  $t'$ :

$$\hat{\Psi}(t) = S(t, t') \hat{\Psi}(t') = S(t, t') U(t') \hat{\Psi}(0). \quad (2.18)$$

The previous equation 2.18 holds because of the relation of the S-matrix to the  $U$  operator:

$$S(t, t') = U(t) U^\dagger(t'). \quad (2.19)$$

Given the S-matrix (equation 2.19), it obeys the following properties:

$$S(t, t) = U(t) U^\dagger(t), \quad S^\dagger(t, t') = S(t', t), \quad \text{and} \quad S(t, t') S(t', t'') = S(t, t'').$$

The equation of evolution of the S-matrix could also be derived:

$$\frac{\partial}{\partial t} S(t, t') = -i \hat{V}(t) S(t, t'). \quad (2.20)$$

Introducing the time ordering operator  $T$ ,

$$S(t, t') = Texp \left[ -i \int_{t'}^t dt_1 \hat{V}(t_1) \right]. \quad (2.21)$$

We are left with the extraction of the ground state of the system  $\Psi(0)$  (which corresponds to the lowest eigenvalue of  $H$ ). For that, we refer to the work of Gell-Mann and Low (1951) [80] where they have already established the relationship between the  $\Psi(0)$  and  $\psi_0$  ( $\psi_0$  is the ground state of  $H_0$  the Hamiltonian of the

unperturbed system at zero temperature):

$$\Psi(0) = S(0, -\infty)\psi_0. \quad (2.22)$$

By the way, we can also convince ourselves from the discussion above that the ground state  $\Psi(0)$  is the same in the three quantum representations.

### 2.1.3. Constructing Green's functions

We can now define in a given  $\lambda$  basis, the Green's functions  $G(\lambda, t, t')$ :

$$G(\lambda, t, t') = -i\langle |TC_\lambda(t)C_\lambda^\dagger(t')| \rangle, \quad (2.23)$$

where  $| \rangle$  is the ground state,  $C_\lambda$  ( $C_\lambda^\dagger$ ) the particle annihilation (creation) operator of  $H$  in Heisenberg's representation and  $T$  is the time ordering operator. Reminding that the same operators with a hat denote there equivalent expression in the interaction representation. These functions are tools from which all physical quantities are extracted in NEGF [76, 77].

From the relation of annihilation and creation operators to the S-matrix and the evolution operator  $U(t)$ ,

$$C_\lambda(t) = e^{iHt}C_\lambda e^{-iHt} = U^\dagger(t)\hat{C}_\lambda(t)U(t) = S(0, t)\hat{C}_\lambda(t)S(t, 0) \quad (2.24)$$

assuming that  $t \rightarrow \infty$ , we could write back the expression of the Green's functions as follows (details could be found in reference [76]):

$$G(\lambda, t, t') = -i \frac{\langle |T\hat{C}_\lambda(t)\hat{C}_\lambda^\dagger(t')S(\infty, -\infty)| \rangle}{\langle |TS(\infty, -\infty)| \rangle}. \quad (2.25)$$

From the definition of Green's function in equation 2.25, we can introduce here expressions of the four most used Green's functions.

$$G_{\lambda, \lambda'}^>(t, t') = -i\langle |C_\lambda(t)C_{\lambda'}^\dagger(t')| \rangle \quad (2.26)$$

$$G_{\lambda, \lambda'}^<(t, t') = i\langle |C_{\lambda'}^\dagger(t')C_\lambda(t)| \rangle \quad (2.27)$$

$$G_{\lambda, \lambda'}^r(t, t') = -i\Theta(t - t')\langle |[C_\lambda(t), C_{\lambda'}^\dagger(t')]_{b,f}| \rangle \quad (2.28)$$

$$G_{\lambda, \lambda'}^a(t, t') = i\Theta(t' - t)\langle |[C_\lambda(t), C_{\lambda'}^\dagger(t')]_{b,f}| \rangle \quad (2.29)$$

Green's functions defined in equations 2.26, 2.27, 2.28 and 2.29 are respectively called the *greater* ( $G^>$ ), *lesser* ( $G^<$ ), *retarded* ( $G^r$ ) and *advanced* ( $G^a$ ) Greens' functions.  $\Theta(t - t')$  is the Heaviside function, which is null for  $t < t'$ , equal to 1 for  $t > t'$  and 0 for  $t = t'$ . The indexes  $b$  and  $f$  stands for boson and fermions.

In the next paragraph, we discuss few examples of non-interacting (bosons and fermions) and interacting (electron-photon) Green's functions.

### 2.1.3.1. Non-interacting Green's functions

In the case of a non-interacting system, from equation 2.23,  $V = 0$  and  $S(\infty, -\infty) = 1$ , so that the free propagators or the unperturbed Green's functions are written:

$$G_0(\lambda, t, t') = -i\langle T\hat{C}_\lambda(t)\hat{C}_\lambda^\dagger(t') \rangle \quad (2.30)$$

⊗ **Fermionic Green's function :**

The free Hamiltonian of a non-interacting system of fermions is given as follow,

$$H_0 = \sum_{\lambda} \varepsilon_{\lambda} C_{\lambda}^{\dagger} C_{\lambda}, \quad (2.31)$$

where  $\varepsilon_{\lambda}$  is a single particle energy. The annihilation operator  $C_{\lambda}$  can be expressed in Heisenberg representation as:

$$C_{\lambda}(t) = e^{iH_0 t} C_{\lambda} e^{-iH_0 t} \Rightarrow i\partial_t C_{\lambda}(t) = [C_{\lambda}(t), H_0] = \varepsilon_{\lambda} C_{\lambda}(t). \quad (2.32)$$

So we obtain:

$$C_{\lambda}(t) = e^{-i\varepsilon_{\lambda} t} C_{\lambda} \quad \text{and} \quad C_{\lambda}^{\dagger}(t) = e^{+i\varepsilon_{\lambda} t/\hbar} C_{\lambda}^{\dagger} \quad (2.33)$$

The four free Green's functions associated to these fermion operators are,

$$G_{0,\lambda\lambda'}^<(t, t') = i\langle C_{\lambda'}^{\dagger}(t') C_{\lambda}(t) \rangle = ie^{-i\varepsilon_{\lambda}(t-t')} n_{\lambda} \delta_{\lambda\lambda'} \quad (2.34)$$

$$G_{0,\lambda\lambda'}^>(t, t') = -i\langle C_{\lambda}(t) C_{\lambda'}^{\dagger}(t') \rangle = -ie^{-i\varepsilon_{\lambda}(t-t')} (1 - n_{\lambda}) \delta_{\lambda\lambda'} \quad (2.35)$$

$$G_{0,\lambda\lambda'}^r(t, t') = -i\Theta(t - t') e^{-i\varepsilon_{\lambda}(t-t')} \delta_{\lambda\lambda'} \quad (2.36)$$

$$G_{0,\lambda\lambda'}^a(t, t') = i\Theta(t - t') e^{-i\varepsilon_{\lambda}(t-t')} \delta_{\lambda\lambda'} \quad (2.37)$$

where  $n_{\lambda}$  is the occupation in state  $\lambda$ .  $n_{\lambda}$  obey the Fermi-Dirac distribution. Let us recall that at equilibrium  $n_{\lambda} = \langle b_{\lambda}^{\dagger} b_{\lambda} \rangle$  is the Fermi-Dirac distribution function,

$$n_i = \frac{1}{e^{\beta(E_i - E_F)} + 1}. \quad (2.38)$$

These Green's functions provide information about the statistics, electron and holes occupation ( $ImG^<, ImG^>$ ). We can also extract spectral characteristics of the system from Green's function, the local density of states ( $ImG^r$ ).

⊗ **Bosonic Green's function :**

The free Hamiltonian of bosons (photons or phonons for instance) is de-



defined as,

$$H_0 = \sum_{q,\lambda} \omega_{q,\lambda} b_{q,\lambda}^\dagger b_{q,\lambda} \quad (2.39)$$

where  $\omega_{q,\lambda}$  is the energy of mode  $q$  with a polarization  $\lambda$ .  $b_{q,\lambda}^\dagger$  ( $b_{q,\lambda}$ ) are boson creation (annihilation) operators given by,

$$b_{q,\lambda}(t) = e^{iH_0 t} b_{q,\lambda} e^{-iH_0 t} \Rightarrow i\partial_t b_{q,\lambda}(t) = [b_{q,\lambda}(t), H_0] = \omega_{q,\lambda} b_{q,\lambda}(t). \quad (2.40)$$

Hence we deduce their expressions,

$$b_{q,\lambda}(t) = e^{-i\omega_{q,\lambda} t} b_{q,\lambda} \quad \text{and} \quad b_{q,\lambda}^\dagger(t) = e^{+i\omega_{q,\lambda} t} b_{q,\lambda}^\dagger. \quad (2.41)$$

The free bosonic lesser Green's function associated to the Hamiltonian is,

$$\begin{aligned} D_\lambda^<(q, t, q', t') &= -i\langle A_{q',\lambda}^\dagger(t') A_{q,\lambda}(t) \rangle, \quad \text{with} \quad A_{q,\lambda}^\dagger = b_{q,\lambda}(t) + b_{-q,\lambda}^\dagger(t). \\ D_\lambda^<(q, t, q', t') &= -i[e^{-i\omega_{q,\lambda}(t-t')} n_{q,\lambda} + e^{i\omega_{q,\lambda}(t-t')} (n_{q,\lambda} + 1)] \delta_{qq'} \end{aligned} \quad (2.42)$$

Similarly, the other Green's functions can be computed since the expressions of the creation and annihilation operators are known.

One of the main interests of Green's functions in transport theory is the possibility to include correlation effects. In general, each Green's function provide information needed to include phase correlation into theory. In the next paragraph, we make a brief description of Green's functions in open nanosystems.

### 2.1.3.2. Electron-photon interaction Green's functions

The starting point here is the expression of the interacting potential. In the case of electron-phonon or electron-photon, the interaction potential is defined as [76],

$$V = \sum_{\mathbf{q}\mathbf{k}s} M_{\mathbf{q}} A_{\mathbf{q}} C_{\mathbf{k}+\mathbf{q},s}^\dagger C_{\mathbf{k},s}, \quad (2.43)$$

where  $M_{\mathbf{q}}$  is the electron-photon coupling matrix. The challenge is to compute Green's function as defined in equation 2.25 in the interacting systems with the given potential. This can be done by mean of Wick's theorem and the use of Feynman diagrams, a full development could be found here [76, 81]. By considering only connected diagrams, the expression of Green's function in equation 2.25 is simplified too,

$$G(p, t, t') = \sum_{n=0}^{\infty} (-i)^n \int_{-\infty}^{\infty} dt_1 \dots \int_{-\infty}^{\infty} dt_n \langle |T \hat{C}_{p\sigma}(t) \hat{C}_{p\sigma}^\dagger(t') \hat{V}(t_1) \dots \hat{V}(t_n)| \rangle \quad (2.44)$$

We want to expand the equation 2.44 up to order  $n = 2$ .

- The  $n = 0$  term correspond to the unperturbed Green's function  $G^{(0)}$ .
- The  $n = 1$  term is zero because, we have

$$\langle |T \hat{A}_{\mathbf{q}}| \rangle = 0. \quad (2.45)$$

All terms with  $n$  odd vanish because their time-ordered bracket for photons contains an odd number of  $\hat{A}_{\mathbf{q}}$ .

Only even  $n$  terms contribute to the S-matrix expansion for electron-photon interaction. One could then write:

$$\begin{aligned} G(\mathbf{p}, t - t') &= G^{(0)}(\mathbf{p}, t - t') + \frac{(-1)^3}{2} \int_{-\infty}^{+\infty} dt_1 \int_{-\infty}^{+\infty} dt_2 \sum_{\mathbf{q}_1 \mathbf{q}_2 s} M_{\mathbf{q}_1} M_{\mathbf{q}_2} \langle |T \hat{A}_{\mathbf{q}_1}(t_1) \hat{A}_{\mathbf{q}_2}(t_2)| \rangle \\ &\times \sum_{\mathbf{k}_1 \mathbf{k}_2 s s'} \langle |T \hat{C}_{\mathbf{p}\sigma}(t) \hat{C}_{\mathbf{k}_1 + \mathbf{q}_1, s}^\dagger(t_1) \hat{C}_{\mathbf{k}_1, s\sigma}(t_1) \hat{C}_{\mathbf{k}_2 + \mathbf{q}_2, s}^\dagger(t_2) \hat{C}_{\mathbf{k}_2, s'}(t_2) \hat{C}_{\mathbf{p}\sigma}^\dagger(t')| \rangle \end{aligned}$$

By considering the simple case of a single photon Green's function

$$\langle |T \hat{A}_{\mathbf{q}_1}(t_1) \hat{A}_{\mathbf{q}_2}(t_2)| \rangle = i \delta_{\mathbf{q}_1 + \mathbf{q}_2} D^{(0)}(\mathbf{q}_1, t_1 - t_2), \quad (2.46)$$

the electron Green's functions described above and the Fourier transform of each term in equation 2.46, one get the expression of the system Green's function in energy-momentum space,

$$G(p, E) = G^{(0)}(p, E) + G^{(0)}(p, E) \Sigma^{(1)}(p, E) G^{(0)}(p, E) \quad (2.47)$$

where  $\Sigma^{(1)}(p, E)$  is called the self-energy of electron due to electron-photon processes.

$$\Sigma^{(1)}(p, E) = i \int_{-\infty}^{+\infty} \frac{d\omega}{2\pi} \sum_{\mathbf{q}} M_{\mathbf{q}} D^{(0)}(\mathbf{q}, \omega) G^{(0)}(\mathbf{p} - \mathbf{q}, E - \omega) M_{\mathbf{q}} \quad (2.48)$$

In order to account for high order term, an approximation is needed. The most used one is Born's approximation. It consist of replacing the last  $G^{(0)}(p, E)$  by  $G(p, E)$  in equation 2.47 so that it reads,

$$G(p, E) = \frac{G^{(0)}(p, E)}{1 - G^{(0)}(p, E) \Sigma(p, E)}, \quad (2.49)$$

Equation 2.49 is well known as Dyson equation, with

$$\Sigma(p, E) = \sum_j \Sigma^j(p, E) \quad (2.50)$$

the sum over all self-energies. The exact Green's functions are obtained by computing the self-energies. Green's function describes the coherent evolution of carriers from the time they are injected into the system until they lose coherence either by flowing out into the connected reservoirs or by scattering into a different state. Self-energies describe the effect of the reservoirs and the different scattering mechanisms on carrier dynamics. These self-energies are the starting point for the Wave Function technique, discussed in the next sections. Before exposure of the Wave Function technique, since we are interested in the dynamic of carriers, we need first to derive the equation of motion of Green's functions.

### 2.1.4. Equation of motion theory

In order to describe the evolution of systems, we need to derive the equation of motion of Green's functions. For a given basis  $\lambda$ , the total Hamiltonian of the system is given by the sum of the free part  $H_0$  and an interaction part  $V_{in}$  containing all the interactions,

$$H = H_0 + V_{in}, \quad \text{and} \quad H_0 = \sum_{\lambda\lambda'} \varepsilon_{\lambda\lambda'} C_{\lambda}^{\dagger} C_{\lambda}$$

the one particle retarded Green's function can be defined as

$$G_{\lambda\lambda'}^r(t, t') = -i\Theta(t - t') \langle [C_{\lambda}(t), C_{\lambda'}^{\dagger}(t')]_{b,f} \rangle, \quad (2.51)$$

where the indexes  $b$  and  $f$  stand respectively for bosons and fermions anti-commutation.  $\Theta$  denote the Heaviside function. Then the equation of motion of  $G^r$  for fermions, using the derivation property  $\partial\Theta(t - t')/\partial t = \delta(t - t')$ , is :

$$\begin{aligned} i\partial_t G_{\lambda\lambda'}^r(t, t') &= \delta(t - t')\delta_{\lambda\lambda'} - i\Theta(t - t') \langle [-i\partial_t C_{\lambda}(t), C_{\lambda'}^{\dagger}(t')]_{b,f} \rangle \\ \sum_{\lambda''} (i\partial_t G_{\lambda\lambda''}^r(t, t') - \varepsilon_{\lambda\lambda''}) &= \delta(t - t')\delta_{\lambda\lambda'} + I_{\lambda\lambda'}^r(t, t'), \end{aligned} \quad (2.52)$$

where we have used the relation

$$-i\partial_t C_{\lambda}(t) = -[H, C_{\lambda}(t)] = \sum_{\lambda''} \varepsilon_{\lambda\lambda''} C_{\lambda''} - [V_{in}, C_{\lambda}(t)], \quad (2.53)$$

and defined  $I_{\lambda\lambda'}^r(t, t')$  to be,

$$I_{\lambda\lambda'}^r(t, t') = -i\delta(t - t') \langle [-[V_{in}, C_{\lambda}(t)]_{b,f}, C_{\lambda'}^{\dagger}(t')]_{b,f} \rangle. \quad (2.54)$$

In the equation 2.52,  $I_{\lambda\lambda'}^r(t, t')$  account for the modifications induced by the interactions to the free Green's function of the system. Whenever the Hamiltonian of the system does not depend explicitly on time, Green's function depends on

time differences  $t - t'$  and one can work their Fourier transform or steady state stationary response.

Equation 2.52 could be written in matrix form as,

$$i\partial_t G^r(t, t') = \delta(t - t') + H(t)G^R(t, t') + \int dv \Sigma(t, v)G^R(v, t'). \quad (2.55)$$

The last term of equation 2.55 corresponds to the  $I_{\lambda\lambda'}^r(t, t')$  term of equation 2.52 accounting for the interaction induced change to the free Green's function.

## 2.2. Wave function technique : ballistic transport

In mesoscopic transport, Green's functions are powerful and efficient building blocks to discuss stationary current and other properties in nanodevices [82]. This practical formalism originates from the theoretical framework developed by Keldysh to approach many-body problems [83]. However, this formalism has a huge computational cost in memory when used for time-dependent problems[84]. Recently, a technique which requires less memory has been proposed by Gaury and co-authors [45] to obtain NEGFs, currents and other time-dependent properties based on smaller-size building blocks, called wave functions (WFs) due to the fact that they finally obey a Schrödinger-like equation (see equation 2.67). Indeed, for a given  $N$ -size problem, WFs are  $N$ -vectors while NEGFs are  $N \times N$  matrices. Switching from matrices to vectors relaxes the computational burden of time-dependent problems. Nonetheless, the so-called NEGF-WF technique still has to be developed for treating scattering mechanisms beyond mean-field approximations.

### 2.2.1. Schematic description

Figure 2.1 gives a schematic view of a general description of a device represented by its retarded Green's function matrix elements and the leads incoming modes. The computational drawback of Green's functions calculation is matrix inversion because of the scaling of computational time with the size of the system. NEGF-WF proposal is to split the matrix into blocks and then compute each block separately. One can after computation of each block reconstructs the whole matrix schematically represented in Figure 2.1. In this case, each block is made of a single column of the retarded Green's function matrix, and blocks are called *wave functions*.

Wave functions are the projection of the system Green's function onto the incoming modes weighted by their velocities  $v_\alpha(E)$  as shown in Figure 2.2. The system can now be described by  $m$  wave functions of the same size as the system  $N$ . This avoids the computation of useless matrix elements with the Green's function, and also reduces by  $N$  the size of the computation objects and their

number by  $N - m$  (for the case where  $N > m$ ). The size of the system,  $N$ , imposes the size of each wave function and the number of modes,  $m$ , considered define the number of wave functions to compute. Actually,  $m$  represented the number of tunneling paths from the reservoirs to the device region. Generally  $m < N$ :  $m$  is related to the contact surface while  $N$  is related to the volume of the system.

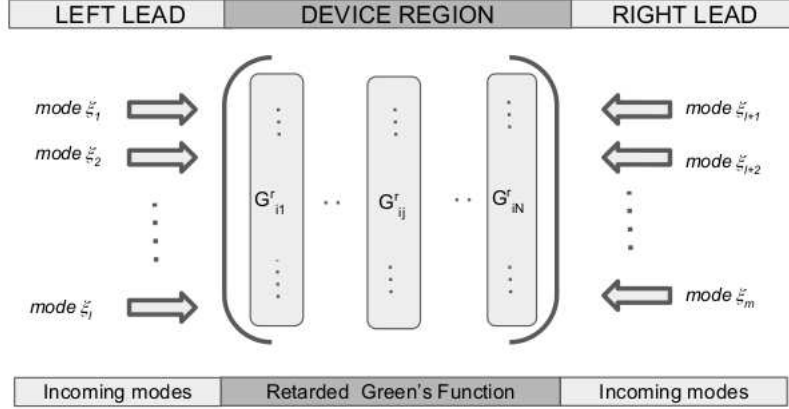


Figure 2.1.: System described by a Green function of size  $N \times N$  for  $m$  incoming modes.

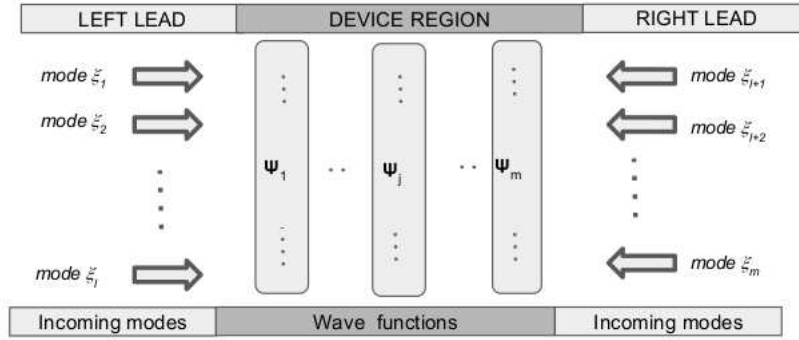


Figure 2.2.: System described by wave functions of size  $N \times 1$  for  $m$  incoming modes.

The next section is dedicated to the technique of computation of these building blocks without making use of Green's function. Clearly the idea is to get rid of matrices in the numerics and use vectors instead so that we gain in memory consumption and CPU time.

### 2.2.2. Constructing wave functions

Let us consider an open quantum system,  $S$ , connected to two semi-infinite leads at left and right sides,  $L$  and  $R$ . This system is identified to be the heart of the nanodevice, also called the active region, and the two reservoirs include the electrical lines. We consider a tight binding type of Hamiltonian of a system  $S$ ,  $H^{tot}$ , made of an active region with its Hamiltonian  $H_{cen}$ , connected to two leads  $L$  and  $R$  represented by  $H_{leads}$ . The device region and the leads are connected through the tunneling Hamiltonian  $H_{tun}$ ,

$$H^{tot}(t) = H_{cen}(t) + H_{leads} + H_{tun}. \quad (2.56)$$

In explicit form it gives,

$$\begin{aligned} H^{tot}(t) = & \sum_{i,j \in S} \varepsilon_{ij}(t) d_i^\dagger d_j + \sum_{\sigma \sigma' \in L, R} \varepsilon_{\sigma \sigma'} c_{\sigma}^\dagger c_{\sigma'} \\ & + \sum_{i \in S, \sigma \in L, R} V_{\sigma, i} c_{\sigma}^\dagger d_i + h.c. . \end{aligned} \quad (2.57)$$

In these expression,  $c_i^\dagger(c_i)$  and  $d_i^\dagger(d_i)$  are the creation (annihilation) operators for a single particle on site  $i$  in the leads and in the system respectively. Elements  $\varepsilon_{ij}$  ( $\varepsilon_{\sigma \sigma'}$ ), represent on-site energies for  $i = j$  ( $\sigma = \sigma'$ ), and inter-site couplings for  $i \neq j$  ( $\sigma \neq \sigma'$ ) in the system  $S$  (leads  $L$  and  $R$ ). Elements  $V_{\sigma, i}$  are system-lead tunneling parameters from site  $i$  in  $S$  to site  $\sigma$  in  $L$  or  $R$ ,  $V_{\sigma, i} \neq 0$  if the two sites  $i$  and  $\sigma$  are connected. In the following, we will use matrix notation in bold style. Matrix elements  $\varepsilon_{ij}$  of system  $S$  form  $\mathbf{H}(t)$  which has a finite dimension, as opposed to the total Hamiltonian that includes semi-infinite leads. In Keldysh's technique, the contact to the lead  $L$  or  $R$  is encoded in a function called self-energy,  $\Sigma_{L, R}$ , which is exactly derived contrary to the usual approximation with master equation. Besides, all properties of the total out-of-equilibrium ground state can be deduced from the lesser ( $<$ ), greater ( $>$ ), retarded ( $r$ ) and advanced ( $a$ ) Green's functions, and the corresponding self-energy components. All these quantities are related to each other and shall obey Dyson's equations [33]. As usually assumed, these reservoirs are non-interacting and at-equilibrium and their associated Green's functions  $\mathbf{g}$  are indeed well-known. In that framework, the expression of  $\Sigma_{L, R}^<$  is given by

$$\Sigma_{L, R}^<(t, t') = \sum_{i \in S, \sigma \in L, R} |V_{\sigma, i}|^2 \mathbf{g}_{\sigma \sigma}^<(t, t'), \quad (2.58)$$

where  $\mathbf{g}_{\sigma \sigma}^<(t, t') = i \langle c_{\sigma}^\dagger(t') c_{\sigma}(t) \rangle$  is the lesser Green's function of reservoir  $L$  or  $R$ . In the present framework, it is assumed that only system  $S$  experiences a time-dependent perturbation. Contact self-energies are thus invariant by translation in time.

Self-energies depend on a single time argument,  $\Sigma_{L,R}^<(t-t')$ , and their Fourier transforms,  $\Sigma_{L,R}^<(E)$ , depend on a single energy argument, via

$$\Sigma^<(t-t') = \sum_{\alpha \in L,R} \int \frac{dE}{2\pi} i f_{\alpha}(E) e^{-i\frac{E}{\hbar}(t-t')} \Gamma_{\alpha}(E), \quad (2.59)$$

where we use the fluctuation-dissipation relation [85]:

$$\Sigma_{L,R}^<(E) = -2i f_{L,R}(E) \Im m \Sigma^r(E)$$

with  $\Sigma_{L,R}^r(E) = -\frac{i}{2} \Gamma_{L,R}(E)$ , and  $f_{\alpha}(E)$  is the Fermi-Dirac distribution function. The real part of the self-energy,  $\Sigma_{L,R}^r(E)$ , that usually account for energy level shift is neglected in this work.

From NEGF formalism to NEGF-WF technique, the mathematical recipe is the diagonalisation of the total contact self-energy  $\Gamma(E) = \Gamma_L(E) + \Gamma_R(E)$ :

$$\Gamma(E) = \sum_{\alpha} v_{\alpha}(E) \xi_{\alpha E} \xi_{\alpha E}^{\dagger}, \quad (2.60)$$

where  $\xi_{\alpha E}$  and  $v_{\alpha}$  are respectively the eigenstates and eigenvalues of the contact self-energy. Besides,  $\xi_{\alpha E}$  are the transverse modes at energy  $E$  and velocity  $v_{\alpha}$  flowing from the leads [45]. Vectors  $\xi_{\alpha E}$  are in general energy dependent, normalized but not necessarily orthogonal [45]. They can become energy independent in specific cases of a wide band limit consideration [86]. The number of propagating modes ( $v_{\alpha} \neq 0$ ) is equal to the number of non-zero tunneling parameters  $V_{\sigma i}$ . Here,  $\alpha$  account for the different modes from all leads. Then, wave functions are defined from the Dyson's equation of  $G^<(t, t')$  as the projection of Green's functions onto the incoming transverse modes of the device, after diagonalization of the lead self-energies in the leads modes space. Wave functions are defined as

$$\Psi_{\alpha E}(t) = \sqrt{v_{\alpha}} \int du e^{-iEu/\hbar} \mathbf{G}^r(t, u) \xi_{\alpha E}, \quad (2.61)$$

details of this derivation can be found in reference [45]. A given WF represents the projection of the Green's function on one of the incoming modes propagating from reservoirs to the system. However, as  $\mathbf{G}^r$  is still unknown at this stage, WFs are not calculated from equation 2.61 but from a differential equation which is practically established from Dyson's equation of  $\mathbf{G}^r$ , as presented in the following.

$$\begin{aligned}
i\hbar\partial_t\Psi_{\alpha E}(t) &= \sqrt{v_\alpha}\int du(i\hbar\partial_t\mathbf{G}^r(t,u))e^{-iEu/\hbar}\xi_{\alpha E} \\
&= \sqrt{v_\alpha}\int du[\delta(t-u)+\mathbf{H}^{tot}(t)\mathbf{G}^r(t,u)+\int dv\Sigma(t,v)\mathbf{G}^r(v,u)]e^{-iEu/\hbar}\xi_{\alpha E} \\
&= \sqrt{v_\alpha}\int du\delta(t-u)e^{-iEu/\hbar}\xi_{\alpha E}+\sqrt{v_\alpha}\int du\mathbf{H}^{tot}(t)\mathbf{G}^r(t,u)e^{-iEu/\hbar}\xi_{\alpha E} \\
&\quad +\sqrt{v_\alpha}\int du\int dv\Sigma(t,v)\mathbf{G}^r(v,u)e^{-iEu/\hbar}\xi_{\alpha E} \\
&= \sqrt{v_\alpha}e^{-iEt/\hbar}\xi_{\alpha E}+\mathbf{H}^{tot}(t)\sqrt{v_\alpha}\int du\mathbf{G}^r(t,u)e^{-iEu/\hbar}\xi_{\alpha E} \\
&\quad +\int dv\Sigma(t,v)\sqrt{v_\alpha}\int du\mathbf{G}^r(v,u)e^{-iEu/\hbar}\xi_{\alpha E} \\
&= \sqrt{v_\alpha}e^{-iEt/\hbar}\xi_{\alpha E}+\mathbf{H}^{tot}(t)\Psi_{\alpha E}(t)+\int dv\Sigma(t,v)\Psi_{\alpha E}(v) \tag{2.62}
\end{aligned}$$

Finally, the equation of motion of  $\Psi$  is given by ( $\hbar = 1$ ),

$$i\partial_t\Psi_{\alpha E}(t)=\mathbf{H}^{tot}(t)\Psi_{\alpha E}(t)+\int dv\Sigma(t,v)\Psi_{\alpha E}(v)+\sqrt{v_\alpha}e^{-iEt}\xi_{\alpha E} \tag{2.63}$$

Actually, the problem is separated into a known stationary problem,  $\mathbf{H}_0$ , and a time-dependent perturbation switched on at  $t = 0$ ,  $\mathbf{H}_p(t)$ :

$$\mathbf{H}^{tot}(t)=\mathbf{H}_0+\mathbf{H}_p(t). \tag{2.64}$$

As a consequence,  $\Psi_{\alpha E}(t)$  also splits in

$$\Psi_{\alpha E}(t)=\Psi_{\alpha E}^p(t)+e^{-iEt/\hbar}\Psi_{\alpha E}^{st}, \tag{2.65}$$

where  $\Psi_{\alpha E}^{st}$  is the stationary wave function related to  $\mathbf{H}_0$ , and  $\Psi_{\alpha E}^p(t)$  is a wave vector that measures the deviation from  $\Psi_{\alpha E}^{st}$  due to the time-dependent perturbation  $\mathbf{H}_p(t)$ . Each term of  $\Psi_{\alpha E}(t)$  complies with the equation of motion of the retarded Green's function  $\mathbf{G}^r$ . As a result,  $\Psi_{\alpha E}^{st}$  is obtained from the stationary transport equation:

$$[E\mathbf{I}-\mathbf{H}_0-\Sigma^r(E)]\Psi_{\alpha E}^{st}=\sqrt{v_\alpha(E)}\xi_{\alpha E}, \tag{2.66}$$

with  $\mathbf{I}$  the identity matrix, and  $\Sigma^r$  the retarded contact self-energy. From the equation of motion of the retarded Green's function [83], one can derive the equation of motion of  $\Psi_{\alpha E}^p(t)$  (see reference [45]):

$$\begin{aligned}
i\hbar\partial_t\Psi_{\alpha E}^p(t) &= \mathbf{H}(t)\Psi_{\alpha E}^p(t)+\int_0^t du\Sigma^r(t-u)\Psi_{\alpha E}^p(u) \\
&\quad +\mathbf{H}_p(t)e^{-iEt/\hbar}\Psi_{\alpha E}^{st}. \tag{2.67}
\end{aligned}$$



Equation 2.67 is the corner stone of the technique and the numerical implementation. Finally, the obtained WFs are used to compute quantities of interest. Lesser and greater Green's functions of system  $S$  are given by

$$G_{ij}^<(t, t') = i \sum_{\alpha} \int \frac{dE}{2\pi} f_{\alpha}(E) \Psi_{\alpha E}(i, t) \Psi_{\alpha E}^{\dagger}(j, t'), \quad (2.68)$$

$$G_{ij}^>(t, t') = -i \sum_{\alpha} \int \frac{dE}{2\pi} (1 - f_{\alpha}(E)) \Psi_{\alpha E}(i, t) \Psi_{\alpha E}^{\dagger}(j, t'), \quad (2.69)$$

where  $\Psi_{\alpha E}(i, t)$  is the  $i^{th}$  component of  $\Psi_{\alpha E}$ . In addition,  $\mathbf{G}^r(t, t') = \Theta(t - t') [\mathbf{G}^>(t, t') - \mathbf{G}^<(t, t')]$ , with  $\Theta(t - t')$  the Heaviside's function. The charge current flowing from site  $i$  to site  $j$  reads:

$$I_{ij}(t) = -\frac{2e}{\hbar} \Im m \left[ \sum_{\alpha} \int \frac{dE}{2\pi} f_{\alpha}(E) \Psi_{\alpha E}^{\dagger}(i, t) H_{ij}(t) \Psi_{\alpha E}(j, t) \right]. \quad (2.70)$$

We discretize equation 2.67 by finite differences and perform the integration with standard integration methods: Euler and Runge-Kutta. The convergence was checked against the number of discretization points along energy and time. Numerical calculations were done on a cluster architecture.

In the present study, numerical calculations were done in the wide band limit (WBL) approximation, which enables one to write  $\Sigma^r(t - u) = i\Gamma\delta(t - u)$ , and thus to simplify equation 2.67. This assumption is valid in mesoscopic systems where energy scales remain smaller than that of the Fermi energy variation in leads, like in the case of metallic electrodes.

## 2.3. Wave function technique : bound electron-hole pair correlations

In this section of the chapter, we extend the NEGF-WF ballistic transport methodology to include electron-electron ( $ee$ ) and electron-hole ( $eh$ ) in the time-dependent numerical simulation. Let us call it NEGF-WF(HF) for the sake of simplicity. Our approach is not restricted to the wide-band limit, even though the presented numerical results rely upon it. We consider a tight binding type of Hamiltonian of a system  $S$ ,  $H^{tot}$ , made of an active region with its Hamiltonian  $H_{cen}$ , connected to two leads  $L$  and  $R$  represented by  $H_{leads}$ . The device region and the leads are connected through the tunneling Hamiltonian  $H_{tun}$ . The electron-electron and electron-hole correlation effects are included to  $H^{tot}$  given equation 2.71. These effects are represented respectively by Hamiltonians,  $H_{ee}$  and  $H_{eh}$ .

$$H_{ee} = \frac{1}{2} \sum_{i \neq j} U_{ij} d_i^\dagger d_i d_j^\dagger d_j, \quad \text{and} \quad H_{eh} = - \sum_{lk} \chi_{lk} d_l^\dagger d_l d_k d_k^\dagger, \quad (2.71)$$

where  $U_{ij}$  and  $\chi_{lk}$  are the electron-electron and electron-hole coupling matrix elements.

The expressions of the others parts of the Hamiltonian,  $H^{tot}$ , are given below,

$$H_{cen}(t) = \sum_{ij} \varepsilon_{ij}(t) d_i^\dagger d_j, \quad H_{leads} = \sum_{\sigma} \varepsilon_{\sigma\sigma'} c_{\sigma}^\dagger c_{\sigma'}, \quad (2.72)$$

$$\text{and} \quad H_{tun} = \sum_{\sigma, i} V_{\sigma, i} c_{\sigma}^\dagger d_i + h.c. \quad (2.73)$$

Let us come back to the expression of the two-particles electron-electron interaction term in its general form [87]:

$$\hat{H}_{ee} = \frac{1}{2} \sum_{ii'jj'} U_{ii'jj'} d_i^\dagger d_{i'}^\dagger d_j d_{j'}. \quad (2.74)$$

In this case  $U_{ii'jj'}$  is the two-particle coupling and  $i, i', j$  and  $j'$  are the site indexes in the single particle basis. The explicit expression of the matrix element  $U_{ii'jj'}$  is,

$$U_{ii'jj'} = \int \int dx_1 dx_2 \phi_i^\dagger(x_1) \phi_{i'}^\dagger(x_2) \frac{e^2}{|x_1 - x_2|} \phi_{j'}(x_1) \phi_j(x_2), \quad (2.75)$$

$\phi_j$  is a localized basis function around site  $j$ . Since wave functions of two different states, with the same spin are orthogonal in real space, their contribution in the matrix element is zero. So that the maximum overlap corresponding to the dominant terms in both  $x_1$  and  $x_2$  integrals are those with  $i = j'$  and  $i' = j$ . Keeping only these terms we can write the electron-electron scattering as a density-density interaction:

$$\hat{H}_{ee} = \frac{1}{2} \sum_{i \neq j} U_{ij} d_i^\dagger d_i d_j^\dagger d_j = H_{ee} \quad (2.76)$$

A similar reasoning can be done to find the expression of the  $H_{eh}$  (see reference [87] for more details).

The total Hamiltonian of the system is the sum of each subpart plus the correlations:

$$H^{tot}(t) = H_{cen} + H_{leads} + H_{tun} + H_{ee} + H_{eh}. \quad (2.77)$$

Once the Hamiltonian settled, we went through the technique of derivation of the equation of motion of the retarded Green's function. First from equation 2.72, one can show that,

$$\begin{aligned}
i\dot{d}_{i'} &= \sum_j \varepsilon_{i'j} d_j + \sum_\sigma V_{\sigma,i'}^* c_\sigma + \sum_j U_{i'j} d_{i'} d_j^\dagger d_j \\
&+ \sum_l \chi_{li'} d_l^\dagger d_l d_{i'} - \sum_k \chi_{i'k} d_{i'} d_k d_k^\dagger.
\end{aligned} \tag{2.78}$$

Using equation 2.78, we obtain the equation of motion of  $G^r$  from its definition,

$$\begin{aligned}
i\partial_t G_{ij}^r(t, t') &= \delta(t - t') \delta_{ij} + \sum_\gamma \varepsilon_{i\gamma}(t) G_{\gamma j}^r(t, t') + \sum_\sigma V_{\sigma,i}^* G_{\sigma,j}^r(t, t') \\
&+ \sum_\gamma U_{i\gamma} G_{i\gamma,j}^{r(2)}(t, t') + \sum_{l \in CB} \chi_{li} G_{il,j}^{r(2)}(t, t') \\
&- \sum_{k \in VB} \chi_{ik} G_{ik,j}^{r(2k)}(t, t')
\end{aligned} \tag{2.79}$$

where the four functions  $G_{ij,j}^{r(2)}$ ,  $G_{ii,j}^{r(2)}$ ,  $G_{il,j}^{r(2)}$  and  $G_{ik,j}^{r(2k)}$  defines unknown higher order Green's functions as :

$$G_{ij,j}^{r(2)}(t, t') = -i\Theta(t - t') \langle \{d_i d_j^\dagger d_j(t), d_j^\dagger(t')\} \rangle \tag{2.80}$$

$$G_{ii,j}^{r(2)}(t, t') = -i\Theta(t - t') \langle \{d_i^\dagger d_i d_i(t), d_j^\dagger(t')\} \rangle \tag{2.81}$$

$$G_{ik,j}^{r(2)}(t, t') = -i\Theta(t - t') \langle \{d_i^\dagger d_l d_i(t), d_j^\dagger(t')\} \rangle \tag{2.82}$$

$$G_{ik,j}^{r(2k)}(t, t') = -i\Theta(t - t') \langle \{d_i d_k d_k^\dagger(t), d_j^\dagger(t')\} \rangle \tag{2.83}$$

Equation 2.79 is not a closed set of equations for  $G_{ij}^r$  because of the presence of the four unknown higher order Green's functions  $G_{ij,j}^{r(2)}$ ,  $G_{ii,j}^{r(2)}$ ,  $G_{il,j}^{r(2)}$  and  $G_{ik,j}^{r(2k)}$ . In order to get a closed set of equations, approximations regarding these last Green's functions are needed. There are several methods of approximations and the one that will be used here is the *Hartree-Fock approximation (HF)*.

Within the HF approximation, the following factorization is made [88, 89].

$$G_{ij,j}^{r(2)}(t, t') = -i\Theta(t - t') \langle d_j^\dagger d_j \rangle \langle \{d_i(t), d_j^\dagger(t')\} \rangle = n_j(t) G_{i,j}^r(t, t') \tag{2.84}$$

$$G_{ii,j}^{r(2)}(t, t') = -i\Theta(t - t') \langle d_i^\dagger d_i \rangle \langle \{d_i(t), d_j^\dagger(t')\} \rangle = n_i(t) G_{i,j}^r(t, t') \tag{2.85}$$

$$G_{ik,j}^{r(2)}(t, t') = -i\Theta(t - t') \langle d_l^\dagger d_l \rangle \langle \{d_i(t), d_j^\dagger(t')\} \rangle = n_l(t) G_{i,j}^r(t, t') \tag{2.86}$$

$$G_{ik,j}^{r(2k)}(t, t') = -i\Theta(t - t') \langle d_k d_k^\dagger \rangle \langle \{d_i(t), d_j^\dagger(t')\} \rangle = (1 - n_k(t)) G_{i,j}^r(t, t') \tag{2.87}$$

From the previous factorization, equation 2.79 can be rewritten in a simplified

form,

$$\begin{aligned}
[i\partial_t + \sum_{k \in VB} \chi_{ik}(1 - n_k) - \sum_{l \in CB} \chi_{li}n_l - \sum_{\gamma} U_{i\gamma}n_{\gamma}(t)]G_{ij}^r(t, t') \\
- \sum_{\gamma} \varepsilon_{i\gamma} G_{i\gamma}^r(t, t') = \delta(t - t')\delta_{ij} \\
+ \sum_{\sigma} V_{\sigma,i}^* G_{\sigma,j}^r(t, t'). \quad (2.88)
\end{aligned}$$

Let us now implement these new interacting terms in the NEGF-WF formalism, starting from equation 2.63.

$$H^{tot}(t) = H_{st} + H_p(t) + \Sigma^c(t) - \Sigma^{c,0} \quad (2.89)$$

$$H_{st} = H_0 + \Sigma^{c,0} \quad (2.90)$$

where we define the interacting Hartree-Fock self-energy as,

$$\Sigma^c(t) = - \sum_{k \in VB} \chi_{ik}(1 - n_k(t)) + \sum_{l \in CB} \chi_{li}n_l(t) + \sum_{\gamma} U_{i\gamma}n_{\gamma}(t), \quad (2.91)$$

and its stationary value  $\Sigma^{c,0} = \Sigma^c(t = 0)$ . We have added and subtracted  $\Sigma^{c,0}$  from the expression of  $H^{tot}(t)$  in order to fullfill the condition of cancellation,  $\tilde{H}_p(t = 0) = 0$ , with  $\tilde{H}_p(t)$  defined as,

$$\tilde{H}_p(t) = H_p(t) + \Sigma^c(t) - \Sigma^{c,0}(E) \quad (2.92)$$

From the equation 2.63, we derive as previously the equation of motion of  $\Psi^p(t)$ .

$$\begin{aligned}
i\partial_t \Psi^p(t) &= H^{tot}(t)\Psi^p(t) + \int_0^t du \Sigma(t - u)\Psi^p(u) \\
&+ \left[ H_p(t) + \Sigma^c(t) - \Sigma^{c,0}(E) \right] e^{-iEt} \Psi^{st} \quad (2.93)
\end{aligned}$$

Actually, equation 2.93 gives the equation of motion of  $G^r$  within the simple framework we propose to handle electron-electron and electron-hole interaction in nanodevices. This equation is similar to the one proposed for ballistic transport but with a modified source term. From here, equation 2.93, has to be solved self-consistently at every single time point in direct link with the values obtained for the self-consistent stationary wave function  $\Psi^{st}$ ,

$$[E - H_{st} - \Sigma(E)]\Psi^{st} = \sqrt{v_{\alpha}}\xi_{\alpha E}, \quad (2.94)$$

where now  $H_{st}$  include  $\Sigma^{c,0}$  term. The numerical implementation consist of two self consistent schemes with the coupled equations 2.94 and 2.93.

## 2.4. Algorithms and numerics

In this section, the numerical implementation algorithms are given. Depending on the discretization method used, the computation can be faster. In our case a simple Euler meshing with a refine slicing in time does the trick. A hundred seconds is needed to get a full transient photocurrent data. So computing an integrated photocurrent requires  $100 \times N_{mesh}$  seconds. With  $N_{mesh}$  the number of meshing points. We recall that not all the algorithms used during this thesis are given here. For instance, the algorithm for the integrated current and beyond wide band limit is not given.

---

### Algorithm 1 NEGF-WF ballistic calculation

---

```

 $N_t \leftarrow \langle \text{the number of time points} \rangle$ 
 $N_e \leftarrow \langle \text{the number of energy points} \rangle$ 
 $n \leftarrow \langle \text{the number of modes} \rangle$ 
for  $i \leftarrow 0$  to  $N_e$  do
  : Stationary calculation
   $\Psi_{1,i}^{st} \leftarrow [EI - H_0 - \Sigma^r] \Psi_{1,i}^{st} = \sqrt{v_1} \xi_1$ 
   $\Psi_{2,i}^{st} \leftarrow [EI - H - \Sigma^r] \Psi_{2,i}^{st} = \sqrt{v_2} \xi_2$ 
   $\vdots \leftarrow \vdots$ 
   $\Psi_{n,i}^{st} \leftarrow [EI - H - \Sigma^r] \Psi_{n,i}^{st} = \sqrt{v_n} \xi_n$ 
  for  $j \leftarrow 0$  to  $N_t$  do
    : Time dependent calculation
     $\Psi_{1,j}^p \leftarrow i\partial_t \Psi_{1,j}^p = [H(t) + \Sigma^r] \Psi_{1,j}^p + H_p(t) e^{-iEt_j} \Psi_{1,i}^{st}$ 
     $\Psi_{2,j}^p \leftarrow i\partial_t \Psi_{2,j}^p = [H(t) + \Sigma^r] \Psi_{2,j}^p + H_p(t) e^{-iEt_j} \Psi_{2,i}^{st}$ 
     $\vdots \leftarrow \vdots$ 
     $\Psi_{n,j}^p \leftarrow i\partial_t \Psi_{n,j}^p = [H(t) + \Sigma^r] \Psi_{n,j}^p + H_p(t) e^{-iEt_j} \Psi_{n,i}^{st}$ 
    : Constructing wave functions
     $\Psi_{1,j}^{tot} \leftarrow \Psi_{1,j}^p + e^{-iEt_j} \Psi_{1,i}^{st}$ 
     $\Psi_{2,j}^{tot} \leftarrow \Psi_{2,j}^p + e^{-iEt_j} \Psi_{2,i}^{st}$ 
     $\vdots \leftarrow \vdots$ 
     $\Psi_{n,j}^{tot} \leftarrow \Psi_{n,j}^p + e^{-iEt_j} \Psi_{n,i}^{st}$ 
    : Constructing Green's functions and observable
     $G^<(E, t) \leftarrow \sum_k f_k(E) \Psi_{k,j}^{tot} \Psi_{k,j}^{tot*}$ 
     $I(E, t) \leftarrow \sum_k f_k(E) \Psi_{k,j}^{tot} H^{tot} \Psi_{k,j}^{tot*}$ 
  end for
  : Constructing integrated observables
end for

```

---

---

**Algorithm 2** NEGF-WF-HF Coulomb interactions

---

$N_t \leftarrow \langle \text{the number of time points} \rangle$   
 $N_e \leftarrow \langle \text{the number of energy points} \rangle$   
 $n \leftarrow \langle \text{the number of modes} \rangle$   
 $k \leftarrow \langle \text{the mode index} \rangle$   
**while** <convergence criteria> **do**  
  **for**  $i \leftarrow 0$  to  $N_e$  **do**  
    : Stationary self consistency  
     $\Psi_{k,i}^{st} \leftarrow [EI - H_0 - \Sigma^{c,0} - \Sigma^r] \Psi_{k,i}^{st} = \sqrt{v_k} \xi_k$   
    : Compute convergence observable  
     $G^<(E) \leftarrow \sum_k f_k(E) \Psi_k^{st} \Psi_k^{st*}$   
    : Store converged wave functions  
     $M_k(:, i) \leftarrow \Psi_k^{st}(i)$   
  **end for**  
  : Compute Hartree – Fock self energy  
   $\Sigma^{c,0}(E) \leftarrow \Sigma_i^{c,0}(E)$   
  : Check convergence  
**end while**  
  +++++++ Time self-consistency ++++++  
  **for**  $j \leftarrow 0$  to  $N_t$  **do**  
    : Time dependent self consistency  
    **while** <convergence criteria> **do**  
      : Construct the Hamiltonian  
       $H^{tot}(t_j) \leftarrow H_0 + H_p(t_j) + \Sigma^c(t_j)$   
      **for**  $i \leftarrow 0$  to  $N_e$  **do**  
        : Collect back the stored stationary wave function  
         $\Psi_{k,i}^{st} \leftarrow M_k(:, i)$   
        : Time dependent calculation  
         $\Psi_{k,j}^p \leftarrow i\partial_t \Psi_{k,j}^p = [H_j + \Sigma^r] \Psi_{k,j}^p + [H_{p,j} + \Sigma_j^c - \Sigma^{c,0}] e^{-iEt_j} \Psi_{k,i}^{st}$   
        : Contructing wave functions  
         $\Psi_{k,j}^{tot} \leftarrow \Psi_{k,j}^p + e^{-iEt_j} \Psi_{k,i}^{st}$   
        : Compute convergence observable  
         $G^<(E, t) \leftarrow \sum_k f_k(E) \Psi_{k,j}^{tot} \Psi_{k,j}^{tot*}$   
         $I(E, t) \leftarrow \sum_k f_k(E) \Psi_{k,j}^{tot} H^{tot} \Psi_{k,j}^{tot*}$   
      **end for**  
      : Compute Hartree – Fock self energy  
       $\Sigma^c \leftarrow \Sigma_j^c$   
      : Check convergence  
    **end while**  
    : Constructing integrated observables  
  **end for**

---

## Conclusion

In this chapter, we introduced the theoretical background as a foundation of the NEGF-WF technique for ballistic transport and beyond for the case of electron-hole pairs correlations. After review of the mathematical concept of Green's functions formalism through its quantum mechanical basis, we presented the NEGF-WF technique for ballistic time-dependent numerical simulations, by showing the switching key from Green's functions to wave functions. The construction of wave functions and the computation of commonly known observables like the current and the time-resolved electron density in the proposed framework are shown. Our main contribution to NEGF-WF is the proposed theoretical approach to include electron-electron and electron-holes correlations at Hartree-Fock level into the dynamical simulation. We have also proposed efficient algorithms for numerical simulation implementation for both ballistic NEGF-WF and NEGF-WF (HF). Briefly, we brought our touch to the technique by introducing a novel efficient theoretical and numerical method to treat correlations at the Hartree-Fock level for time-dependent quantum transport in optoelectronic devices. The next stage of the theoretical and numerical development of this framework is the treatment of the molecular vibrations and bosonic interaction. Including these interactions will provide us with a powerful numerical tool for a more precise description of ultrafast quantum transport phenomena in nanosystems.

## DYNAMICAL LEVEL STRUCTURE AND PHOTO-INDUCED CHARGE CURRENT IN ORGANIC SEMICONDUCTOR DEVICES

Nanoscale molecular electronic devices and machines are emerging as promising functional elements for next-generation technologies since they are naturally flexible, efficient and operate on subpicosecond time scales. A deeper understanding of electron transfer processes in molecular junctions is expected to benefit many fields ranging from nanoelectronics to bio-engineering. Several advances are registered in the field. From the intra-molecular coherence control of molecular devices [90] to the generation of terahertz frequencies through a UV light modulated photo-conducting graphene nano-ribbon [91], a lot is done in molecular electronics development like the realization of interference-based molecular transistors [92]. In fact, the control of quantum dynamics on subpicosecond time-scale is of high impact on compact terahertz-radiation devices for organic compounds as well as observation of living matter. It has also been recently shown that it is possible to reconstruct the absorption spectrum of a molecular junction by mean of photocurrent pump push spectroscopy, which is exactly the usual pump-probe spectroscopy where the probe is an infrared (IR) light pulse and photocurrent measurement is performed (see Figure 3.1) [93]. In Figure 3.1,  $\frac{dJ}{J}$  is the relative difference of the push induced photocurrent with respect to the pump-induced photocurrent. These advances are the insight into the field. The remaining questions are on what control charge, energy transfer processes and transport mechanisms in such junctions on these timescales. The answer might come from a step by step investigation of the optoelectronic properties of molecular junctions on a subpicosecond time scale. In this Chapter, we investigate the dynamical optoelectronic properties of a donor-acceptor molecular junction subject to an externally applied Gaussian laser field. The aim is to extract the underlying physics, quantum properties and characteristics of the nanojunction. The numerical simulations rely on the NEGF-WF framework pro-



posed in Chapter 2 and ignoring the electron-electron and the electron-hole correlations in this first part of the study of photoinduced charge transfer processes. These correlations are treated in the next chapter. This ballistic study will provide us with the basics but most important internal quantum properties of nanojunctions. Such insights into the dynamical optoelectronic properties of molecular junctions are of strong interest for ultrafast spectroscopy, and opens avenues toward the possibility of analyzing and controlling switching mechanisms, photocatalytic processes and the internal properties of quantum nanodevices.

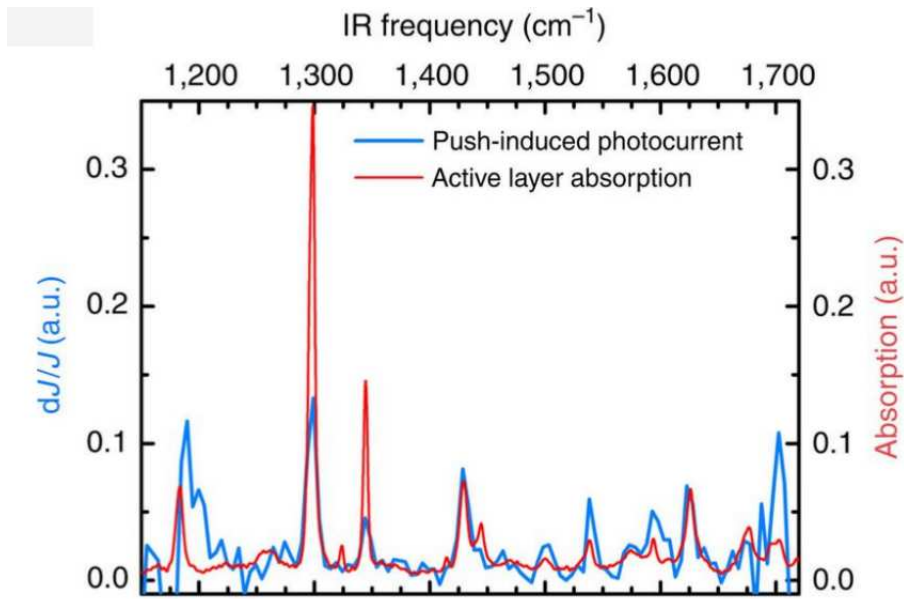


Figure 3.1.: Vibrational modulation effect. The vibrational part of the photocurrent pump push spectroscopy response, measured at negative delay time from [93].

### 3.1. Device structure

We consider an unbiased molecular junction laterally connected to two metallic electrodes, as schematically depicted in Figure 3.2. The molecular complex consists of a donor (D)-bridge-acceptor (A) chain, which represents a key molecular model for organic semiconductors and biological applications [16]. The numerical calculations are implemented by means of the time-dependent NEGF base WF technique presented in chapter 2. The notations in this chapter are the same as in the previous one.

We model the overall device as a three-level system made of the highest occupied molecular orbital (HOMO) and the lowest unoccupied molecular orbital (LUMO) of the donor, coupled to the LUMO of the acceptor through a coupling

parameter  $\beta$  that globally describes the bridge effects. The molecular complex forms system  $S$ . It is connected on the left and the right sides to metallic leads through the same energy-independent contact self-energy  $\Sigma_{L,R} = -i\Gamma$ .

In this model of the molecular junction,  $H_0$  and  $H_p(t)$  are  $3 \times 3$  matrices with non-zero elements  $H_{0_{ii}} = \varepsilon_i$ ,  $H_{0_{23}} = H_{0_{32}} = \beta$ , and  $H_{p_{12}}(t) = M(t)$  is the pulse-induced light-donor coupling. The time-dependent electromagnetic field is included in  $M(t)$  that couples the HOMO to the LUMO of the donor. The pulse-induced light-donor coupling  $M(t)$  is defined as  $M(t) = \Theta(t)A(t) \cos(\omega t)$  with  $\Theta(t)$  the Heaviside function and  $A(t) = A_0 \exp(-(t - t_c)^2/2\tau^2)$ , where  $A_0$  is the maximum amplitude and  $g(t) = \exp(-(t - t_c)^2/2\tau^2)$  the Gaussian envelope of the pulse. The full width at half maximum is given by  $FWHM = 1.66\tau$  and  $\omega$  is the central frequency of the pulse. In the present study, we fix  $\varepsilon_1 = -0.7$  eV,  $\varepsilon_{2,3} = +0.7$  eV,  $\hbar\omega = \varepsilon_2 - \varepsilon_1 = 1.4$  eV, and  $\tau = 5.0$  fs. The temperature is also fixed to 10 K. The coupling  $M(t)$  is shown in Figure 3.3.

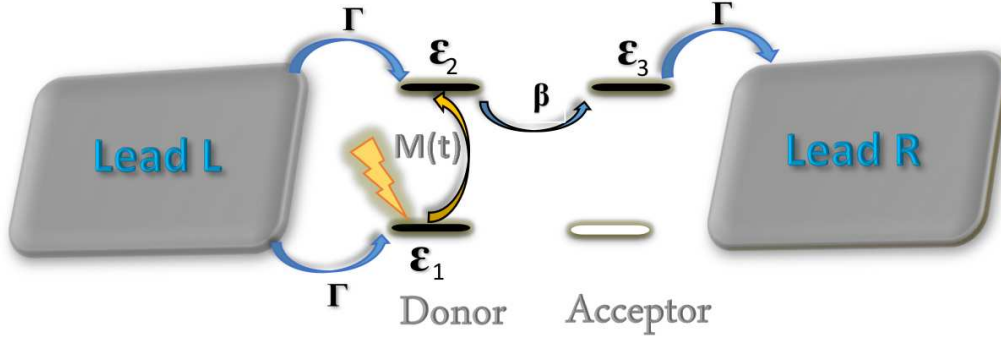


Figure 3.2.: Schematic representation of the molecular junction. Energies  $\varepsilon_1$  and  $\varepsilon_2$  are the atomic orbitals of the donor and  $\varepsilon_3$  the LUMO orbital of the acceptor.

The FWHM of the pulse irradiance,  $\Delta t$  in Figure 3.3 (A) and the width of its Fourier transformed frequency  $\Delta\nu$  on Figure 3.3 (B), should obey Heisenberg's uncertainty principle,

$$\Delta t \Delta\nu \geq 1. \quad (3.1)$$

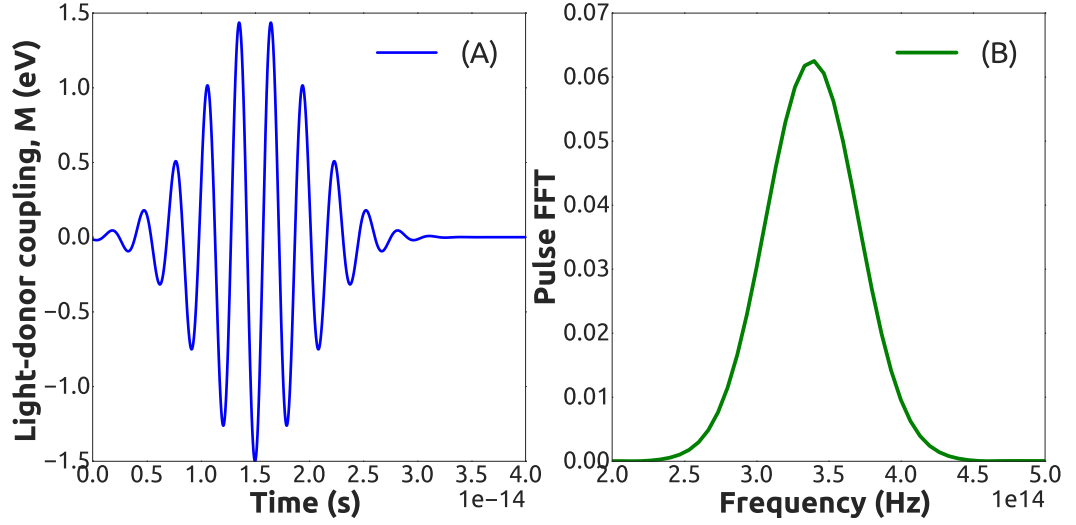


Figure 3.3.: Pulse-induced light-donor coupling,  $M(t)$ , as a function of time (left panel). Fast Fourier transformed signal of the pulse (right panel).

The aim is to understand carrier dynamics at the interface of a D-A molecule sandwiched between two metallic electrodes, by analyzing the time-resolved photocurrent flowing through the D-A junction when the donor is excited by a femtosecond Gaussian-shape laser pulse. The time-dependent electromagnetic field induces carrier absorption and emission from the LUMO and HOMO inside the donor. The excited electrons and holes are transferred to electrodes, it results in a photocurrent through the molecular junction as a unique consequence of electron excitation by ultrafast laser pulse radiation.

## 3.2. Population dynamics

We first analyze the dynamics of carriers inside the molecular complex. The intramolecular orbital populations are numerically computed by integrating over energy the time-resolved spectral lesser Green's function associated to each molecular level  $i$ :

$$n_i(t) = \text{Im} \frac{1}{\pi} \int G_{ii}^<(E, t) dE, \quad (3.2)$$

where  $G_{ii}^<(E, t) = \int e^{\frac{iE(u-t)}{\hbar}} G_{ii}^<(u, t) du$ .

Populations of Figure 3.4 point out carrier pathway just after the perturbation is initiated. In the beginning, the pulse induces a *HOMO-LUMO* transition at the donor (levels 1 to 2 of Figure 3.2), followed by intermolecular tunneling oscillations between donor and acceptor *LUMOs* (level 2 and 3 of Figure 3.2). Meanwhile, in the donor, there are noticeable interferences of propagating modes.

Therefore, the pulse field induces population oscillations with two characteristic frequencies.

The first oscillation is only patterned during the light-donor interaction in populations  $n_1$  and  $n_2$ . Corresponding frequency is about  $\sim 2\omega$  ( $\omega$  being the central pulse frequency). This "on-pulse" oscillation is the result of absorption and wave function interferences inside the donor. The second oscillation occurs at the end of the pulse train: both populations  $n_2$  and  $n_3$  show damped oscillations of relaxation Figure 3.4. These oscillations, called here "off-pulse" oscillations for simplicity, essentially involve the donor and acceptor LUMOs. These oscillation frequencies are controlled by both the pulse amplitude  $A_0$  and the intramolecular donor-acceptor coupling  $\beta$ . However, their amplitude is proportional to the  $\beta$  value for the case of the on-pulse oscillation and its inverse for the off-pulse oscillations. These two characteristic frequencies represent important physical effects in a driven nanodevice: induced interferences pattern and intramolecular LUMOs tunneling oscillations.

The induced off-pulse oscillation fringes result from spectral interference of two slightly different frequencies components of the wave function emitted at two different times. The time at which the laser pulse have the same amplitude on the leading and the trailing edges of the pulse envelope, these two excitations generate waves of the same instantaneous frequency that may interfere constructively or destructively depending on the phase difference. A predictive study of the positions of the destructive or constructive interference pattern even though interesting will not be discussed in this thesis. A sketch of an analytical perturbative study to the first order, using a monochromatic field instead of a laser pulse, by mean of the *Rotating Wave Approximation (RWA)*, reveals that the tunnel oscillating frequency is of order

$$\omega' = \frac{\sqrt{4\beta^2 + A_0^2}}{2\hbar}. \quad (3.3)$$

This frequency depends on both the field parameter  $A$  and the intermolecular coupling  $\beta$ . On the other hand, off-pulse oscillation have a characteristic frequency depending on the whole junction since it is of order  $\sim \frac{\beta}{\hbar}$ . The internal quantum tunneling frequency of the device is accessible once the current is measured, implying that molecular coupling  $\beta$  can be measured from the current. The discussion will be deepened in section 3.5.1.

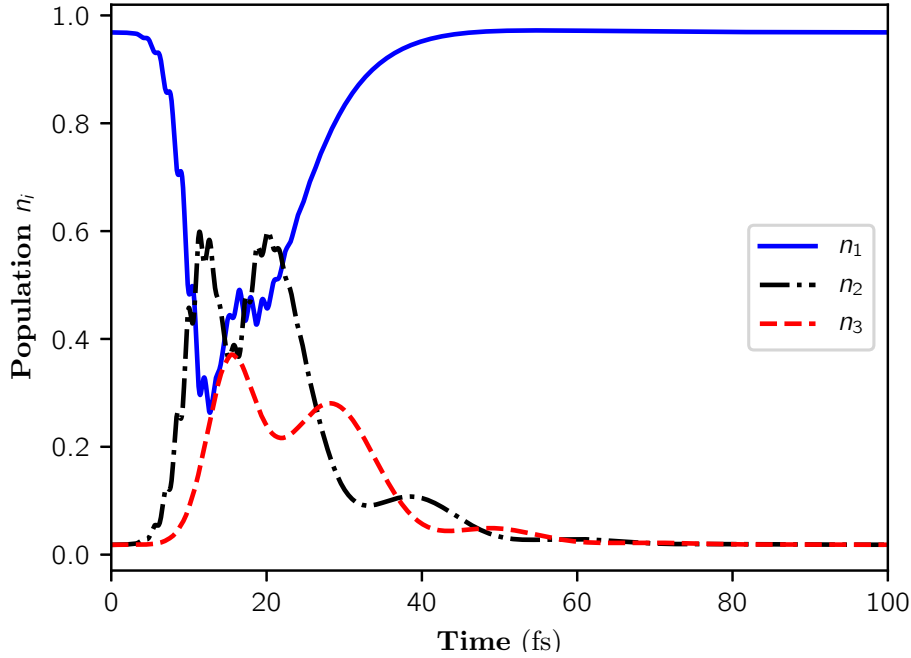


Figure 3.4.: Populations  $n_1$  of donor level 1,  $n_2$  of donor level 2,  $n_3$  of acceptor level 3. Simulation parameters are  $\beta = 0.1$  eV,  $\Gamma = 0.05$  eV, and  $A_0 = 0.5eV$ .

### 3.3. Photocurrent generation

The dynamics of populations results in a transient photocurrent within the relaxation time set by the donor-acceptor and molecule-lead couplings. The time-resolved photocurrent flowing from donor to acceptor  $I_{DA}(t)$  reflects indeed this dynamics of populations and their characteristics, as depicted in Figure 3.5(A). Both on-pulse and off-pulse population oscillations are remarkably visible on the photocurrent variation. In cases where on-pulse oscillations have been obtained [45, 94], their low amplitude brought to the conclusion that they could not be experimentally measurable due to capacitive effects [94]. However, beyond the fact that this frequency is proportional to that of the field, its relative amplitude depends on the donor-acceptor coupling strength  $\beta$ , as illustrated in Figure 3.5(B) where  $\beta$  is three times the value used in Figure 3.5(A). We thus infer that it might be possible to detect this frequency in the case of strongly connected donor-acceptor, with the right choice of bridge. In terms of charge transfer, the off-pulse oscillation owns a characteristic frequency of forth and back-tunneling between levels  $|2\rangle$  and  $|3\rangle$ . This frequency is related to the intramolecular D-A

coupling, as shown in Figure 3.5(B). However, it can also be seen that the amplitude of this off-pulse oscillations are reduced for a high  $\beta$  value in opposition to the case of the on-pulse oscillation. It comes out that a high  $\beta$  value induces high on-pulse oscillation amplitudes but low off-pulse oscillation amplitudes. An intermediate value of  $\beta$  could collapse the on- and off-pulse so that observation of oscillations could be critical. The previous discussion will lead the choice of the bridge in building the donor-acceptor junction in molecular devices.

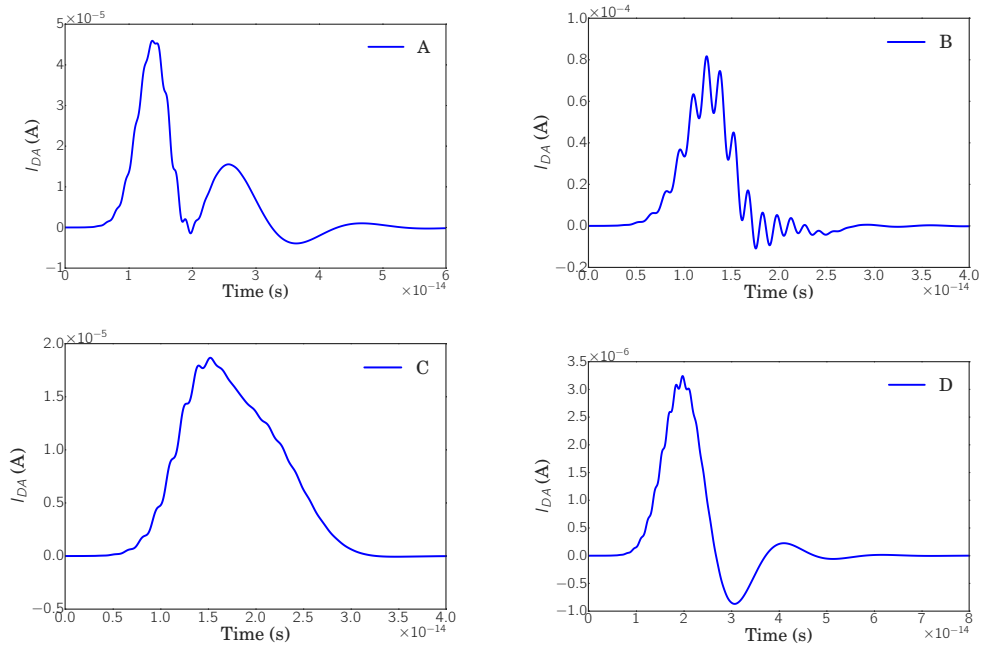


Figure 3.5.: Time-resolved photocurrent expressed in ampere. Simulation parameters are  $\beta = 0.1$  eV,  $\Gamma = 0.05$  eV, and  $A_0 = 0.5$  eV. (A) with the same parameters as in Figure 3.4, (B) except that  $\beta = 0.3$  eV instead of 0.1 eV, (C) except that  $\Gamma = 0.2$  eV instead of 0.05 eV, and (D) except that  $A_0 = 0.05$  eV instead of 0.5 eV.

The off-pulse oscillation amplitude is also strongly damped due to the relaxation of the system to equilibrium induced by the molecule-lead coupling  $\Gamma$  (see again Figure 3.2). In figure 3.5(C),  $\Gamma$  is increased compared to Figure 3.5(A): one can no more observe the intramolecular oscillation neither in population (not shown) nor in photocurrent. The off-pulse oscillations are progressively damped as  $\Gamma$  increases and finally disappear at strong  $\Gamma$ . The intramolecular dynamics only survives when carriers are long lived in the system, which means for a sufficiently weak coupling to leads or whenever the characteristic time for the proper dynamics of the molecule is smaller than the relaxation time of the open system,  $\tau_r = \hbar/\Gamma$ . Finally, the light-donor coupling amplitude  $A_0$  has been

divided by a factor ten in Figure 3.5(D). Compared to Figure 3.5(A), the photocurrent amplitude is also reduced by about the same factor. Moreover, the negative oscillation within the on-pulse regime is amplified, which might affect the directionality of the integrated current. We thus quantify this directionality by defining the following ratio:

$$r = \frac{\int I(t)dt}{\int_{I(t)>0} I(t)dt - \int_{I(t)<0} I(t)dt}, \quad (3.4)$$

whose sign indicates the current directionality:  $r = 1$  if  $\int_{I(t)<0} I(t)dt = 0$  so that charges flow towards the right side of the junction,  $r = -1$  if  $\int_{I(t)>0} I(t)dt = 0$ , charges flow towards left, and  $r = 0$  if  $\int_{I(t)>0} I(t)dt = \int_{I(t)<0} I(t)dt$ , there is no charge transfer in average between the two metallic electrodes. Comparing the four device configurations of Figure 3.5(A,B,C,D), we obtain  $r = 0.76$  in Figure 3.5(A),  $0.82$  in Figure 3.5(B),  $r = 1.00$  in Figure 3.5(C), and finally  $0.58$  in Figure 3.5(D). Such a control over the inversion and suppression of current was already pointed out in classical single level tunneling structure [59]. We here confirm the crucial role of the field amplitude inside the light-donor coupling  $M(t)$ , as well as the D-A intermolecular coupling. For strong coupling to reservoir, the inversion of  $I(t)$  is suppressed. Electrons do not spend enough time inside the molecule to oscillate between levels  $|2\rangle$ - $|3\rangle$  and experience strong induced emission. This discussion on carrier dynamics and photocurrent suggests that we can generate, shape and control signals of different frequency through the design of molecular junctions.

The populations in Figure 3.4 and corresponding photocurrent in Figure 3.5(A) are in agreement with the results obtained using density matrix approach in Ref. [16], which is valid to second order in the molecule-leads coupling. Actually, off-pulse oscillations and damping are also present. The magnitude of these two phenomena is stronger in the present work due to the fact that we explore strong system-lead couplings, which permits NEGF formalism.

An extended view of what has been said so far on the  $\beta$  coupling and the field amplitude  $A_0$  effect is shown by the mapping of the photocurrent in Figure 3.6. In the left panel the photocurrent spectral view as a function of time and the intramolecular coupling  $\beta$ , where the increase of the on-top oscillations and the decrease of the off-pulse oscillations amplitudes with  $\beta$  is confirmed. In the right panel, the photocurrent is represented as a function of time and pulse amplitude  $A_0$ . Additionally to the effects described in Figure 3.5, we notice that as  $A_0$  increases, the maximum of the transient photocurrent is reached faster. Meaning that device responds faster with  $A_0$ . This might be induced by the rising time of the field envelope, that is reduced by the increase of  $A_0$ . Further analysis is possible in that direction for switching process applications.

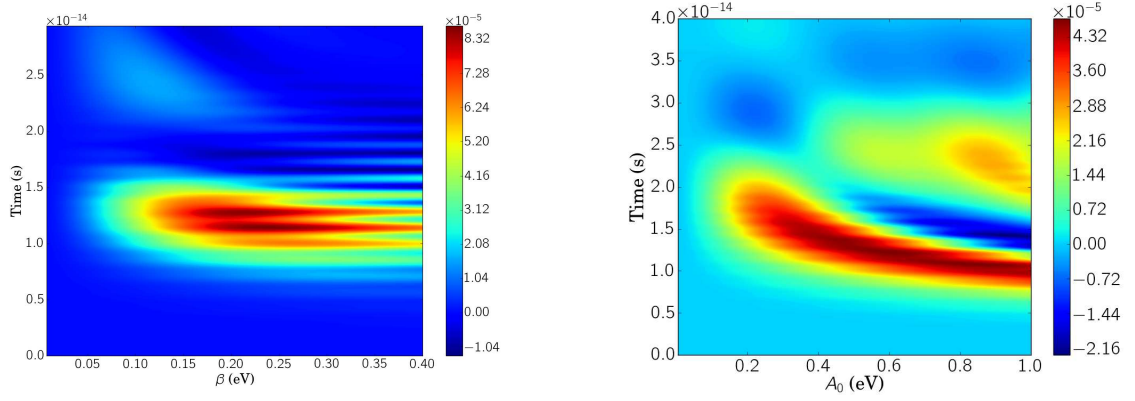


Figure 3.6.: Time-resolved photocurrents maps: as function of  $\beta$  (left panel), and pulse amplitude  $A_0$  (right panel), with  $\Gamma = 0.05eV$ .

Finally, we propose an analytical model for photocurrent analysis. Let us summarize the overall dynamics into three zones, as shown in Figure 3.7. In fact there a first zone, *Zone A*, that is a mixte of stationary dynamics and the raising dynamics of the system. The faster the raising time, the better the photodetection applications.

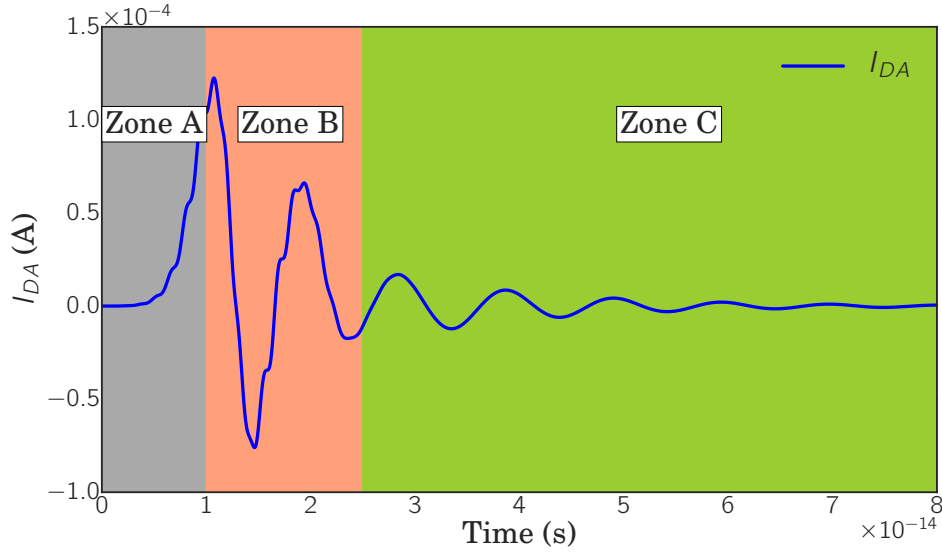


Figure 3.7.: Photocurrent showing three dynamical regions: Raising dynamic (Zone A), Forced dynamic (Zone B) and Damped oscillations dynamics (Zone C).

The second zone, *Zone B*, is the forced dynamic zone, where the dynamic is forced by an external impulse or field. *Zone C* shows the dynamic of the freed



oscillations, will no external influence, but damp. This last regime is more interesting due to the fact that it mostly depends on the system parameters and less on the external ones. The photocurrent in *Zone B* and *C* could be approximated with the following functions:

$$I_B(t) = I_{0B}e^{(-\Lambda_B t)} \cos(\omega_B t) + I_s \quad (3.5)$$

$$I_C(t) = I_{0C}e^{(-\Lambda_C t)} \cos(\omega_C t), \quad (3.6)$$

where,  $\Lambda_B$  is the damping function that depends on  $\Gamma$ ,  $\beta$  and the field amplitude,  $A$ . Similarly,  $\Lambda_C$  is a damping function in the off pulse photocurrent. As shown in Figure 3.11a, in some cases  $\Lambda_C$  can be approximated as  $\Lambda_C \hbar \sim \Gamma$ .  $\Lambda_C$  weakly depends on  $\beta$  and  $A$ .  $\omega_B$  and  $\omega_C$  are oscillating frequencies as defined previously with the particularities that  $\omega_B$  is time-dependent and  $\omega_C$  is not and could be approximated as  $\omega_C \hbar \sim \beta$ . Finally  $I_s$  is the source term induced current, the forcing current.  $I_s$  could be found by taking the average value of the *Zone B* photocurrent.

### 3.4. Ultrafast electronic structure dynamics

In order to deepen the analysis, we define a time-resolved local density of states (TRLDOS) at site  $i$ :

$$TRLDOS_i(E, t) = \text{Im} \sum_{\alpha} \left[ \frac{i}{2\pi} \Psi_{\alpha E}(i, t) \Psi_{\alpha E}^{\dagger}(i, t) \right]. \quad (3.7)$$

This definition reduces to the standard one of  $LDOS(E)$  in the stationary case, as demonstrated in the appendix A.

Such a time-, energy- and space-resolved quantity provides insights into the dynamical photoelectronic structure produced by the time-dependent electromagnetic field, as shown in Figure 3.8.

Firstly we observe a time-dependent energy level shift, known as dynamical Rabi shift. Indeed, in a quantum system driven by an external field of time-dependent amplitude, the near-degenerated dressed states undergo time-dependent splitting  $\omega'(t) = \sqrt{4\beta^2 + \hbar^2 \omega_r^2(t)}/2$  where  $\omega_r(t)$  is the instantaneous Rabi frequency given by  $\omega_r(t) = A(t)/\hbar$ . This dynamical Rabi shift generates redshifted and blueshifted sidebands at instantaneous frequencies  $\omega - \omega'(t)$  and  $\omega + \omega'(t)$  which are schematically drawn on Figure 3.9a. Actually, in Figure 3.8, the  $TRLDOS_D$  shows the three stationary molecular hybridized orbitals before the pulse is set on, which takes about  $t = 10$  fs. As soon as the pulse is set on, the energy levels are no more constant over time but dynamically shifted with respect to their stationary values. The shift results in dynamical Rabi sidebands: the three initial stationary states dynamically shifted, plus a lower-energy level

appearing after  $t = 10$  fs, as illustrated in Figure 3.9a. This additional dynamical level is generated due to the fact that the pulse replicates the two upper energy levels inside the lower-energy part of the donor spectral function which then also splits into two Rabi sidebands [61]. Along the time axis, oscillation generation is also visible at almost all energies. After the pulse, for  $t = 40$  fs to  $t = 100$  fs, the system relaxes back to its stationary configuration with the three atomic orbitals surrounded by interference patterns damped due to the molecule-lead coupling.

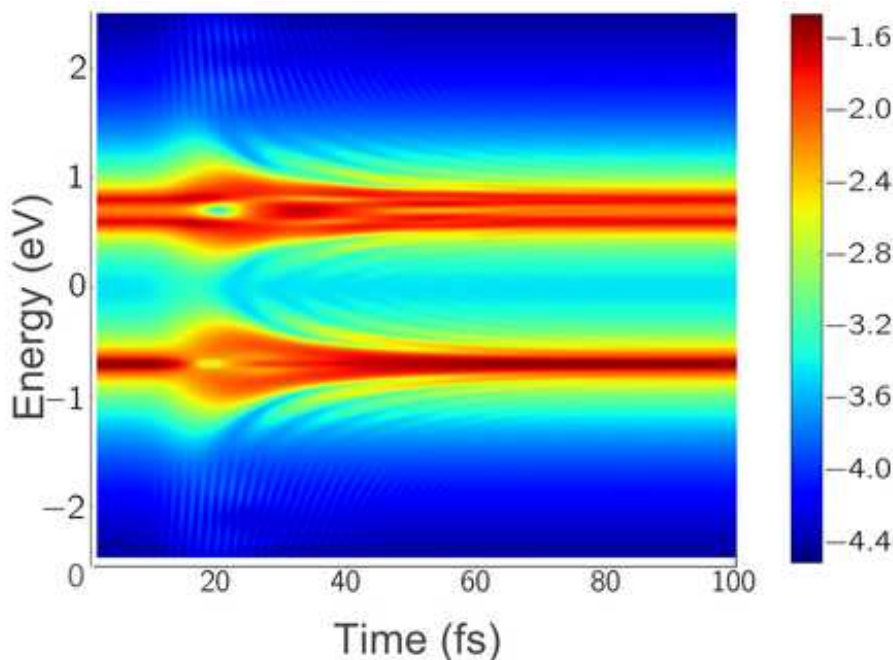


Figure 3.8.: Time-resolved local (donor) density of states at the donor (in logarithm scale). Simulation parameters are  $\beta = 0.1$  eV,  $\Gamma = 0.05$  eV, and  $A_0 = 0.5$  eV.

Additionally, we observe low-amplitude satellite maxima from a closer look around  $\pm 2$  eV of Figure 3.8, that we identified as Floquet-like states. In order to examine these features of TRLDOS appearing in the system, we have numerically extracted and plotted the energy and time coordinates of TRLDOS local maxima which are represented in Figure 3.9b (this figure also remarkably shows the dynamical Rabi shift).

We notice that these satellite states appear at energies of about  $E_i \pm \hbar\omega$ , and we have checked that states follow this trend when we change  $\omega$ . We thus infer that these satellite states are Floquet-like states.

Let us make a brief recall here about Floquet-states. In fact, it has been shown for a symmetric Hamiltonian under time translation  $H(t) = H(t + \tau)$ , ac-bias application for instance, that the system splits into multiple states with quasi-energies  $E \pm \hbar\omega$  [95]. For the one dimensional case, the time dependent

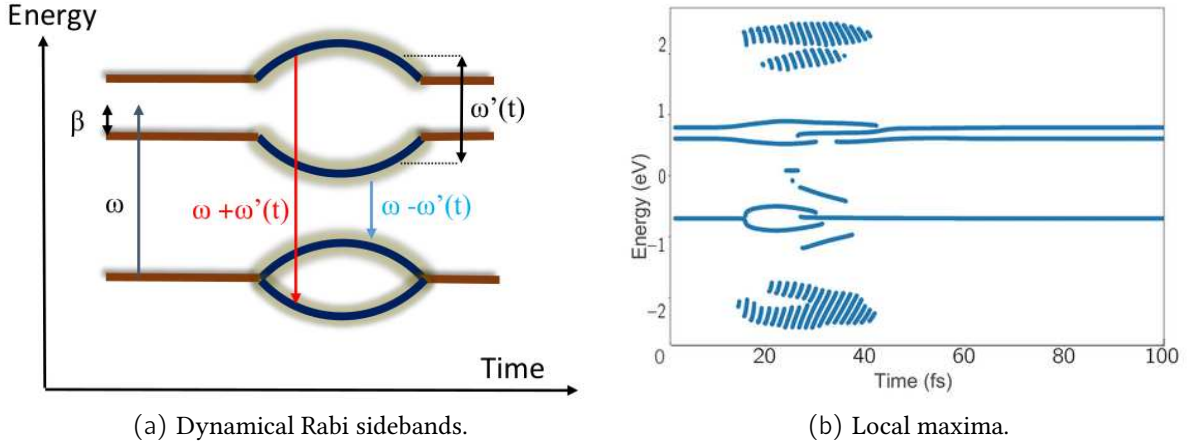


Figure 3.9.: (a) Sketch of the dynamical Rabi sidebands. (b) Traces of local maxima of time-resolved local density of states extracted from figure 3.8.

Schrödinger equation gives:

$$(H(t) - i\hbar \frac{\partial}{\partial t})\Psi(t) = 0, \quad \text{and} \quad H(t) = H_0 + H_{ex}(t). \quad (3.8)$$

$H_0$  is assumed to have a complete orthogonal basis set of eigenfunctions  $\psi_n$  with the corresponding eigenenergy  $E_n$ :

$$H_0\psi_n = E_n\psi_n. \quad (3.9)$$

According to Floquet theorem [18], there exists solutions to the time-dependent equation 3.8, called Floquet states solution

$$\Psi_\alpha(t) = \exp(-i\varepsilon_\alpha t/\hbar)\Phi_\alpha(t), \quad (3.10)$$

where  $\Phi_\alpha(t)$  is the periodic Floquet mode and  $\varepsilon_\alpha$  is the quasi-energy unique up to an integer multiple of  $\hbar\omega$  ( $\omega = 2\pi/\tau$  is the  $H_{ex}(t)$  frequency).

$$\varepsilon_\alpha \mapsto \varepsilon_\alpha + n\hbar\omega.$$

In the case studied here, the electromagnetic field is not monochromatic, due to its Gaussian shape, and hence, the Hamiltonian is not periodic, but we still observe the presence of these states with almost similar quasi-energies. Nevertheless, the presence of these Floquet-like states might be due to a weak rate of change of the field envelope with respect to its frequency. In fact, if the field envelope varies slowly compared to the cosine period, the field can be approximated by a monochromatic field. In such a case, the Hamiltonian should be quasi-symmetric by time translation, then time modulated Floquet states might appear.

The Floquet like states appearance as explained above depends on the field shape. In fact, Floquet states appear here in the approximation that the rate of change in the field amplitude  $dg$  is smaller with respect to the central oscillating laser field frequency  $\omega$ . This is an approximated regime in between the time-translational symmetric Hamiltonian and non-symmetric Hamiltonian. As example for  $A = 0.5$ , the rate of change in the field envelope is  $dg \sim \frac{1}{42}\omega$ . Reducing the FWHM of the laser field will reduce the ratio  $\frac{dg}{\omega}$  and the system tends to the translational symmetry breaking with an effect of cancellation of the Floquet states.

Finally, we decipher the internal dynamics of this molecular system interacting with a time-dependent electromagnetic field. Cuts at different times of TRLDOS are represented in Figure 3.10.

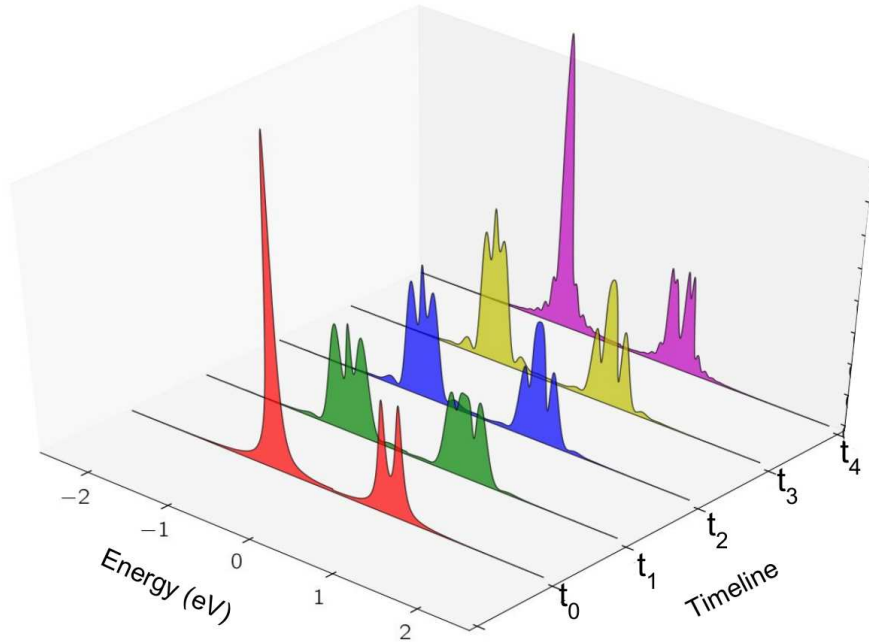


Figure 3.10.: Instantaneous local (donor) density of states for different times ( $t_0 = 10$  fs,  $t_1 = 25$  fs,  $t_2 = 30$  fs,  $t_3 = 35$  fs and  $t_4 = 60$  fs), with the same parameters as in figure 3.4.

These instantaneous densities of states as shown on Figure 3.10, indicate that the external field applied to the system induces a coupling of the molecular levels with the field modes, so that we not only have a rearrangement of the non-equilibrium molecular orbitals but also pulse-induced secondary maxima in the system spectral response due to the broad spectrum of the pulse. Due to the hybridization with states of the leads, molecular levels broaden, which allows us to regard the local molecular density of states as a sum of level Lorentzian envelopes. We observe that the instantaneous LDOS for  $t_1$ ,  $t_2$ ,  $t_3$  have a different

full width at half maximum compared to the LDOS at  $t_0$ . Moreover, the energy level spacing is changed as shown up with the dynamical Rabi shift. The pulse tends to distort and reshape the Lorentzian envelopes, which originates from field-induced coupling renormalization in the molecular device. These effects of renormalization and rearrangement of molecular orbitals are suppressed for strong coupling to leads due to state delocalization. This last point could be a problem of experimental interpretation since the broadening could hide extra molecular orbitals or even shifts.

## 3.5. Proposal of experimental measurement

### 3.5.1. Intramolecular couplings and terahertz frequencies

From an experimental point of view, it might be possible to directly measure the contact coupling of metallic electrodes to the molecule  $\Gamma$ , and the intermolecular coupling  $\beta$  at low temperatures, when molecular vibrations are weak and negligible. Measuring the contact coupling consist of doing a fitting of the off-pulse photocurrent with a decaying exponential  $\exp(-\eta t)$ , where  $\eta \sim \Gamma/\hbar$  (Figure 3.11a). One possible way to experimentally capture the value of the intermolecular coupling is to perform a Fast Fourier Transform (FFT) of the off-pulse photocurrent signal since its oscillation frequency should be about  $\sim \beta/\hbar$  (figure 3.11b). This last measure could also be possible with a two dimensional FFT of the time-coupling photocurrent. From FFT of different cuts in Figure 3.6 (left panel) at different values of  $\beta$  in the off-pulse regime (above  $25fs$ ), we estimate the numerical values of  $\beta$ , given in Table 3.1.

$\beta$ (input) in eV	0.1	0.2	0.3	0.35
$\beta$ (FFT) in eV	$0.08 \pm 0.03$	$0.209 \pm 0.04$	$0.24 \pm 0.065$	$0.34 \pm 0.05$

Table 3.1.: Comparison of input value  $\beta$  to the numerical value extracted from FFT.

The good agreement between the input values  $\beta$  and their output estimated from the simulated experiment validate our proposal of experimental measurement. For the measurement of  $\Gamma$  further investigations need to be pursued and determine how to adjust the exponential fitting depending on the external field shape and strength.

This analysis raises the question of "terahertz gap". The 'terahertz gap' has a frequency ranges from  $\sim 0.3$  THz to  $\sim 10$  THz, this range is said to be non-invasive, non-destructive, invisible, non-ionizing and biologically safe. Terahertz frequencies thus find applications in ultrafast nanodevices (high-speed wireless information transmission between electronic devices), biomedical imaging, cancer and pollutants detection and so on [96]. Our idea is that since we can

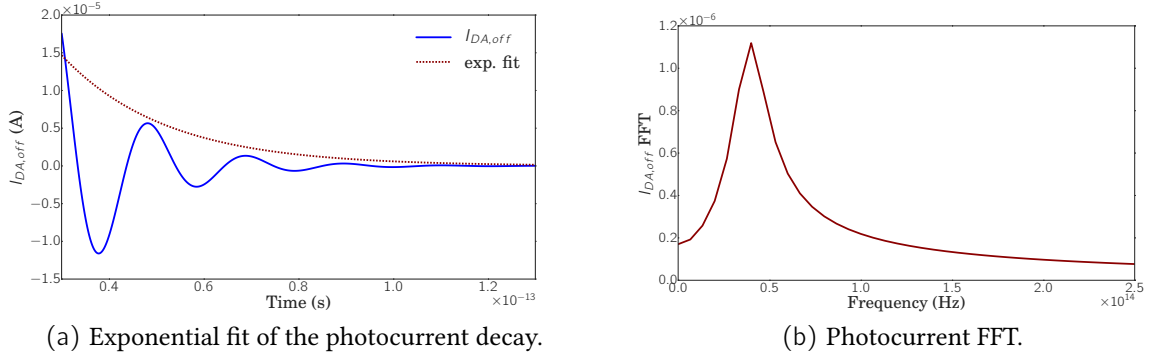


Figure 3.11.: Proposal of experimental measurement of  $\Gamma$  and  $\beta$  from off pulse photocurrent (a) exponential fit:  $\exp(-0.03 * t/\hbar)$  for  $\Gamma = 0.03\text{eV}$ , (b) FFT of the off pulse photocurrent for  $\beta = 0.1\text{eV}$ .

measure the intramolecular coupling from the photocurrent frequencies, we can consider designing the nanojunction in such a way that the device produces a desired frequency in the photocurrent. In that case, we propose to generate on demand, shape, and control terahertz signals. This might be an impressive advance regarding the expected applications with THz frequencies.

Finally, more realistic simulations including electron-electron scattering and molecular vibrations might lead to stronger damping of the oscillations described above. Electron-electron scattering nonetheless occurs on the timescale ranging from sub-picoseconds to attoseconds [97, 98], while the electronic oscillations have oscillation periods of tens of femtoseconds or less. Hence, if the ultimate goal of molecular electronics is to achieve switching times on the electronic timescale, the oscillations predicted here will be highly relevant in the limit of sub-picoseconds scattering timescale.

### 3.5.2. Rabi dynamics and tunneling competition

Regarding the dynamical Rabi shift of the energy levels, there is a limit in the ratio  $\Gamma/A$ , where the shift is no more visible. In fact whenever the dynamical energy level shift is smaller compared to the energy level broadening  $\sqrt{4\beta^2 + A^2} < 2\Gamma$ , the shift will be hidden or will manifest itself in the loss of smoothness and or symmetry of the Lorentzian shape of the local density of states. Weakly coupled systems are likely to generate dynamical Rabi shifts. Figure 3.12 shows the energy level splitting as a function of time, and its maximum gives the limit value of  $\Gamma$ ,  $\Gamma_0$ .

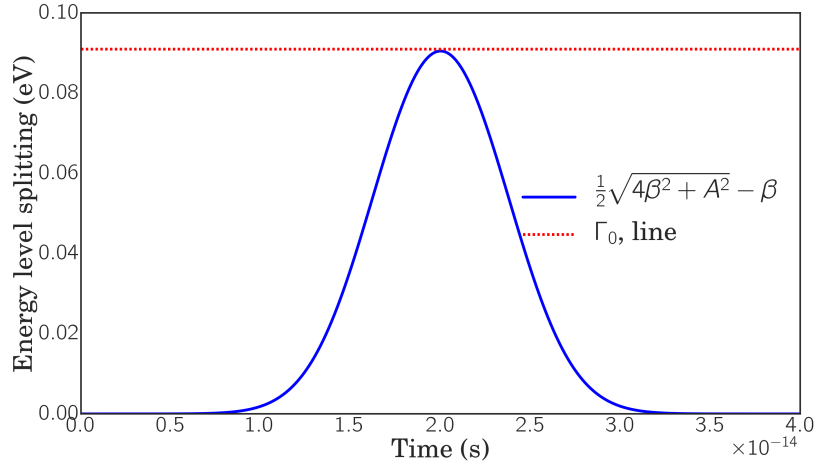


Figure 3.12.: Energy level splitting. For values of  $\Gamma$  above the  $\Gamma_0$  line, the splitting of the energy level is no more visible. Parameters are  $\beta = 0.1$  eV and  $A_0 = 0.5$  eV.

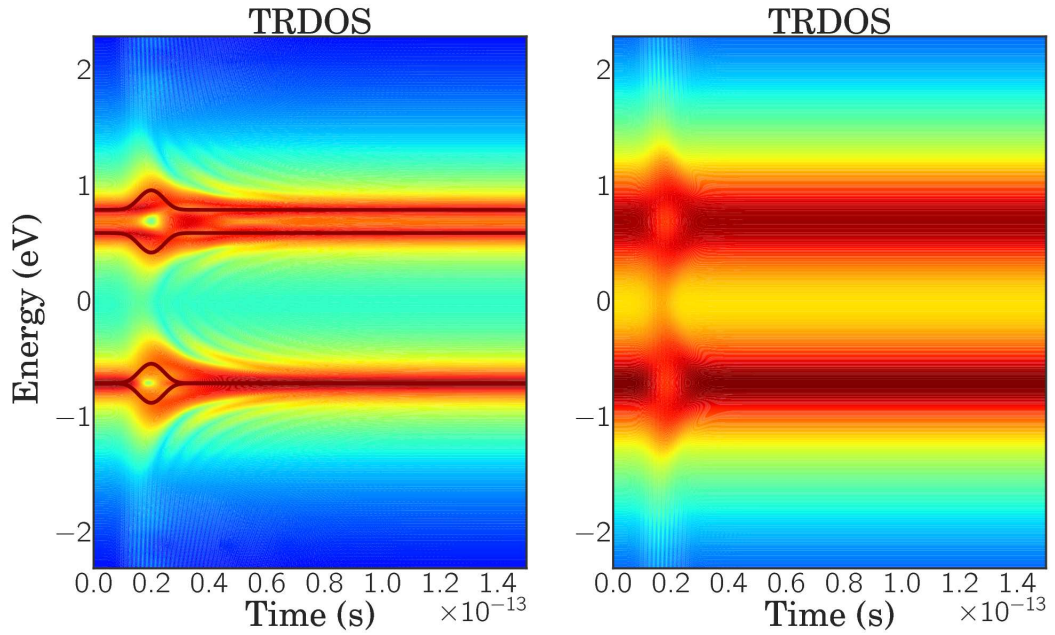


Figure 3.13.: Time-resolved local (donor) density of states. For values of  $\Gamma = 0.05\text{eV}$  (left panel) and  $\Gamma = 0.25\text{eV}$  (right panel).

Let us recall that the loss of energy splitting is characterized by the cancellation of the tunneling oscillations in the photocurrent, Figure 3.5 (C). The TRLDOS at strong broadening is represented on the right panel of Figure 3.13, where we



can see the two upper levels of the junction are merged in comparison to weak broadening shown in the left panel of Figure 3.13.

Let us get more insight into the global picture of the dynamics from Figure 3.14. Figure 3.14 represents limit values of  $\Gamma$ ,  $\Gamma_0$  as function of  $\beta$  for two values of the pulse amplitude. The upper and the lower regions of each curve plotted in Figure 3.14 show two distinct regimes of transport. The upper region ( $\Gamma > \Gamma_0$ ) correspond to the *direct* tunneling while the lower region correspond to the *oscillating* tunneling regime. Every couple of parameters ( $\beta, \Gamma$ ) chosen in any of these regions determine a transport mechanism type for carriers. In fact couple of parameters ( $\beta, \Gamma$ ) chosen below the curves gives rise to the oscillating tunnel transport otherwise it is a direct tunnel transport. Note that the two transport regimes are directly scaled by the pulse amplitude strength towards high ( $\beta, \Gamma$ ) values, for increasing  $A$  value. This last comment is critical in the improvement of the design and the efficiency of ultrafast optoelectronics.

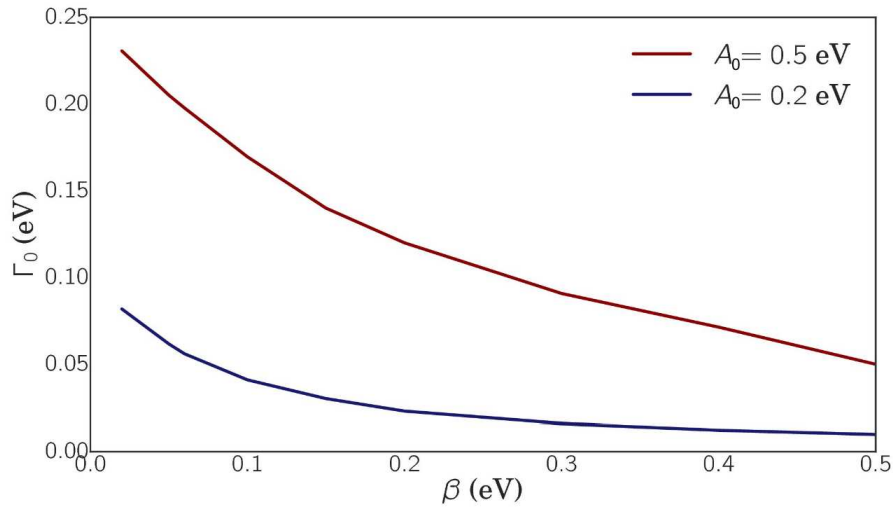


Figure 3.14.: Limit values  $\Gamma_0$  as function of  $\beta$  for two values of the pulse amplitude.

The diagrammatic sum up of our interpretation of charge dynamics in this simple D-A complex device is finally illustrated in Figure 3.15.



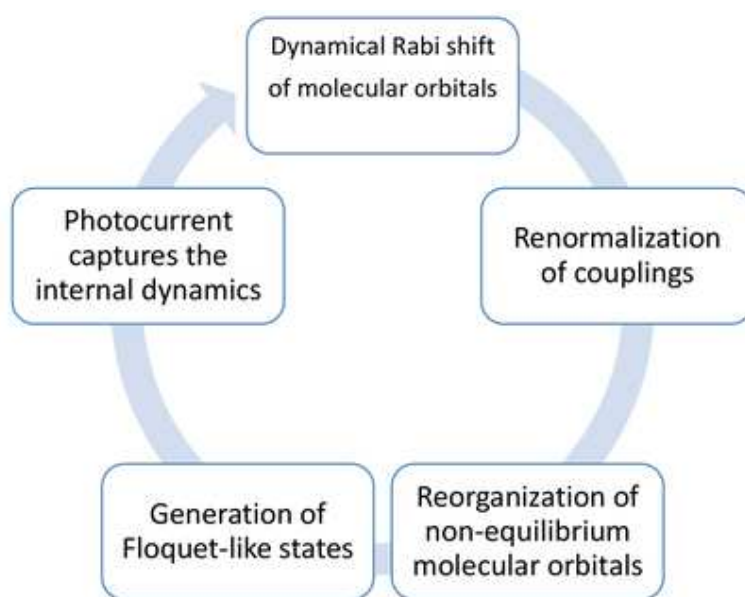


Figure 3.15.: Diagrammatic picture of the internal electronic structure dynamics inside the D-A molecular junction.

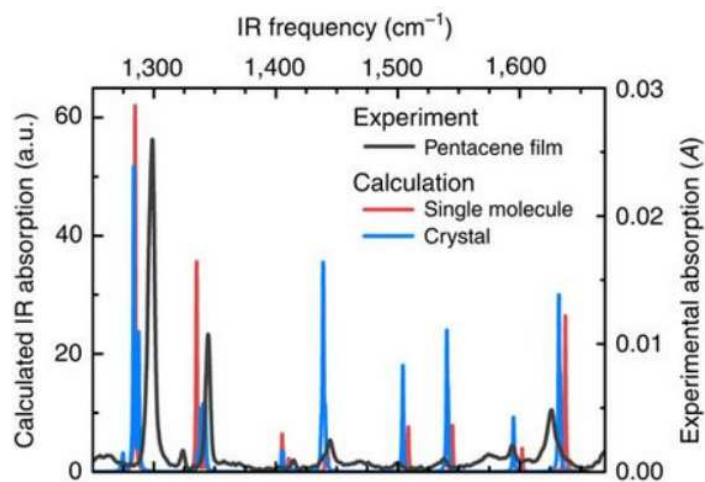


Figure 3.16.: Simulated infrared (IR) spectrum for the pentacene molecule (red) and crystal (blue), superimposed on the experimental spectrum for comparison from [93].

The overall point is that the experimental absorption spectrum of a molecule will depend on the width and the strength of the pulse with respect to its coupling to the reservoirs. As in Figure 3.16, where the simulated infrared spectra for a single pentacene molecule and for a crystal is compared to the experimental

infrared absorption, the discrepancy ( $\sim 10\text{cm}^{-1}$ ) might come from the numerical model not taking into account the ultrafast band structure bending. We agree with the authors on the argument that the intermolecular coupling is important in the photocurrent enhancement, but one should also consider electrode-molecule and intramolecular couplings renormalization.

### 3.6. Discussion

Regarding the dynamical Rabi shift and Floquet-like states generation, it has been shown in the case of a single oscillating level that the interaction of a molecular junction with an external time-dependent electromagnetic field leads often to two phenomena that have been used to control the tunneling in semiconducting molecular optoelectronics [99–101].

The first one is the coherent destruction of tunneling (CDT) [102, 103]. The dynamical Rabi shift induced by the fact that in the presence of a laser field, a pair of the nearest neighbor sites shifts up and down in opposite direction [104], could explain the CDT in semiconducting molecular devices. Meaning that whenever the right dynamical shift induces an overall zero mean value for the photocurrent, the integrated current will be null, so tunneling is destructed.

The second phenomenon is the photo-assisted tunneling (PAT) [95]. An external time translational symmetric field with frequency  $\omega$  can induce inelastic tunneling processes whenever electrons exchange a quantum of energy  $\hbar\omega$  with the radiation field in such a way that tunneling occurs through satellite states at energies  $E_i \pm n\hbar\omega$ , where  $n$  is an integer, positive for photon absorption and negative for photon emission.

Finally, what could be inferred concerning the photocurrent pump-push spectroscopy (PPPS) experiment? As described above, the PPP is a promising alternative to standard all optical spectroscopic methods as far as optoelectronic nanodevices are concerned and a hybrid spectroscopic method with electrical detection. It provides the possibility to access vibrational modes and their coupling to electronic dynamics. But the experimental realization requires an *IR* push as a probe, that could excite carriers in the two low-laying Rabi sidebands and not in the high laying levels as desired by the experiment. In fact, depending on the intermolecular coupling and the intensity of the external field, the generated Rabi sidebands could have a splitting about the *IR* push pulse energy. One could consider that PPPS experiments, regarding the efficiency of charge transfer in molecular junctions (Figure 3.17) could be improved because of possible loss mechanisms that could be induced by low-laying Rabi sidebands absorptions.

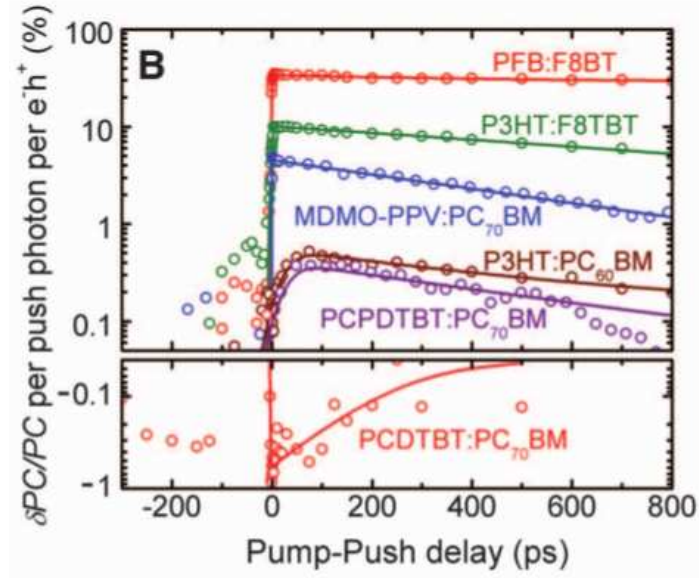


Figure 3.17.: Results of pump-push photocurrent experiments on a set of organic photovoltaic [105]. In this plot  $\delta PC/PC$  is the same as  $dJ/J$  in 3.1.

## Conclusion

The present study attempts to establish the time-resolved response of a D-A molecular complex to a femtosecond Gaussian-shape laser pulse within the proposed Keldysh's formalism based NEGF-WF technique. Definitely, applying an ultrashort laser pulse induces a dynamical energy level shift and generation of Rabi sidebands that induces Floquet-like states, both shown on Figure 3.9b. These Floquet-like states could be the anomalous edge states observed in weakly driven lattice systems [106]. The photocurrent is sensitive to the quasi-energy spectrum of the transient Floquet states and the Rabi sidebands. The TRLDOS shows a signature of oscillations similar to those in the photocurrent i.e. on-/off-pulse oscillations. In the present study, Floquet-like states have a weak amplitude in TRLDOS. However, these Floquet-like states could open new transport channels to be taken into account for transport processes, that could also control the directionality and the optimization of the photocurrent in molecular devices [59]. The dynamical Rabi shift and induced sidebands also manifest variations of tunneling parameters, which provides a coherent control of the field-induced photocurrent. An optical investigation could reveal the signature of these Rabi sidebands as blueshifted and redshifted frequencies in the absorption spectrum of such devices. Moreover, one could capture, generate, shape and control terahertz frequencies (even beyond) from external electromagnetic field induced intramolecular dynamics. Even though the experimental measurement of these transient photocurrents in the femtosecond time scale is not possible

up to date, the femtosecond carrier dynamics of the molecular junction could be captured from the direct photocurrent by means of photocurrent pump-push spectroscopy, where the delay between the pump and the push pulses allows to control the time resolution.

The major points are the possibility to measure the internal quantum molecular overlap strength and the transient dynamics of a junction while accessing the photocurrent. Inversely connected molecular nanojunctions could be used to generate terahertz frequencies and beyond on will just through the control of the nanojunction bridging. This work opens indeed a discussion on the relevance of transient dynamics in the understanding of time-resolved device operations and avenues towards ultrafast device design for future technologies.

## DRIVING ENERGY AND ULTRAFAST BOUND ELECTRON-HOLE PAIR DYNAMICS

Light-induced photoexcitations in organic semiconducting nanosystems generate bound electron-hole pairs, called excitons, and their separation into free charge carriers is a key cross-cutting issue for photovoltaics and molecular optoelectronics. There are two identified types of bound electron-hole pairs that could be generated in organic semiconducting devices such as photovoltaic solar cells upon photoexcitation. The exciton, that is generated immediately after light absorption in the absorbing molecule (donor), and the charge-transfer (CT) state is generated through the electron transfer from the absorber to the other molecule (acceptor) while the hole remains in the absorber. It is commonly accepted that reducing the binding energy of both the exciton and the CT state will improve the efficiency of such devices [107] or abnormally reduce the efficiency [108].

In these nanodevice types, excitons and CT states often have an important impact on transport properties. Exciton creation as described in Chapter 1 as resulting from the interaction of a photon with the organic material. The delocalization and transfer of the created exciton from one side to the other of the device is controlled by complex processes of charge and energy transfers. Key parameters in the process are transfer time, exciton binding energy, LUMO-offset energy in the case of a donor-acceptor junction. There are other parameters entering the dynamical process that have not been taken into account in this work. For instance, the exciton diffusion length that several techniques, from photoluminescence (PL) [109] to Forster resonance energy transfer theory [110], failed to agree on, because the diffusion length in a given material varies depending on the technique employed. The discrepancy might be due to the carrier mobility dependence on alternating field frequency in such a way that experimental direct current measurement of the exciton mobility may not be justified [111]. This confirms again that time-resolved techniques are necessary for understanding exciton dynamics in organic materials since these dynamics happen on time

scales of sub-picoseconds. These limitations added to the fundamental historical mismatch between the optical (about micrometer scale) and molecular-length scales, are barriers to the experimental investigations. But then numerical time-dependent simulation techniques could allow to break through these barriers and to explore a wide range of parametric configurations, providing pathways to experimental realizations. Describing the transport of excitons and CT states in nanodevices requires approaches that correctly take into account the interplay between the dynamical electronic structure and bound electron-hole dynamics. In order to deepen the analysis of these complex processes, we use here the extended Wave Function technique with electron-electron and electron-hole interactions as we developed in Chapter 2, to analyze the quantum dynamics of bound electron-hole pair in the same donor-acceptor molecular junction as the one basically investigated in Chapter 3. We study the impact of electron-hole interaction on the time-resolved local density of state, on the photocurrent, and on the driving energy of the junction. We also make proposals of experimental protocols of photocurrent spectroscopy, the measurement of the driving energy, pump-push photocurrent spectroscopy and determination of transfer characteristic timescales. The aim is to propose an efficient characterization of the electronic structure of molecular junctions, which offers control and shape of carrier transport dynamics, opening the way to new physical properties and optoelectronic nanodevices.

Let us recall here that a donor-acceptor junction can be built in planar or heterostructure configuration as shown on Figure 4.1 for the planar configuration. We assume here a planar configuration where excitonic interactions are weaker, but much more trackable [112]. Nonetheless, the methodology could be applied to a non-planar configuration.

This chapter is organized as follow. A first part describes impacts of excitons and CT states on the TRLDOS and their correlations to photocurrent. A second part is dedicated to the interplay between exciton binding and offset energies. Finally, the last part develops our proposals to identify characteristic time scales and implement ultrafast spectroscopic methods.

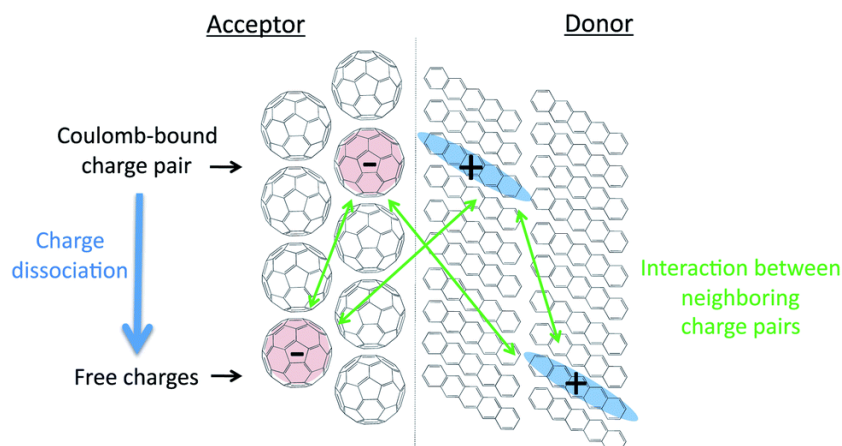


Figure 4.1.: Interactions that play a role in organic semiconducting junctions. Pentacene donor and fullerene acceptor from [112].

## 4.1. Impacts of electron-hole Coulomb interaction

In this section, we essentially lay the foundations we need to discuss impacts of excitonic effects on ultrafast dynamical process.

### 4.1.1. Model and method

The model used is the same as the one in chapter 3, except that electron-electron and electron-hole interactions are included. The system is an unbiased molecular junction, as schematically depicted in Figure 4.2. A molecular complex  $S$ , laterally connected on the left and the right sides to metallic leads through symmetric energy-independent contact self-energies  $\Gamma$ .

For convenience, we recall the generic description we used. The donor molecule is merely described by only two active orbitals, the HOMO and LUMO, denoted here  $\varepsilon_1$  and  $\varepsilon_2$ . Similarly, for the acceptor molecule, only the active LUMO is considered and denoted  $\varepsilon_3$ . In this model as previously,  $H_0$  and  $H_p(t)$  are  $3 \times 3$  matrices with non-zero elements  $H_{0_{ii}} = \varepsilon_i$ ,  $H_{0_{23}} = H_{0_{32}} = \beta$ , and  $H_{p_{12}}(t) = M(t)$  is the pulse-induced light-donor coupling. The pulse-induced light-donor coupling  $M(t)$  is defined as  $M(t) = \Theta(t)A(t) \cos(\omega t)$ , with  $\Theta(t)$  the Heaviside function and  $A(t) = A_0 \exp(-(t - t_c)^2/2\tau^2)$ . The following parameters are fixed all along this study,  $\varepsilon_1 = -0.7$  eV,  $\varepsilon_{2,3} = +0.7$  eV,  $\hbar\omega = \varepsilon_2 - \varepsilon_1 = 1.4$  eV,  $\tau = 5.0$  fs and the temperature to 10 K.

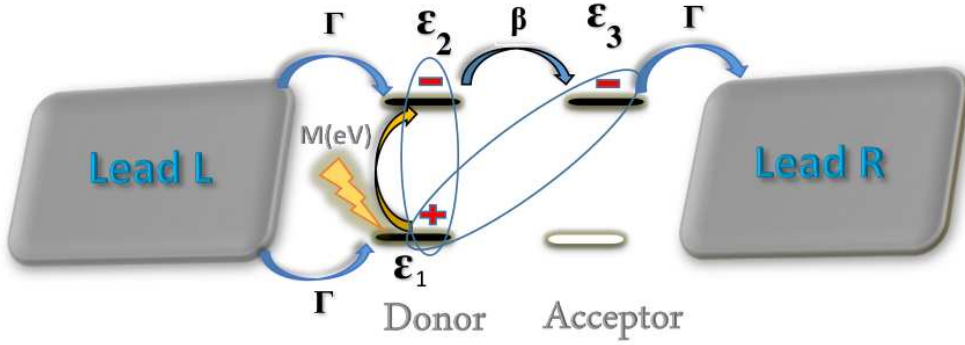


Figure 4.2.: Donor-acceptor junction including coulomb correlations;  $\varepsilon_1$  and  $\varepsilon_2$  are the atomic HOMO and LUMO of the donor, and  $\varepsilon_3$  the LUMO orbital of the acceptor.

The numerical technique is based on the extended Wave Function technique and its corresponding algorithm (2) given in Chapter 2. Algorithm (2) consists of computing self-consistently at each time point, including the stationary time point zero, the Hartree-Fock correction term to the Hamiltonian of the system. For the nanosystem considered here, the time-dependent Hartree-Fock self-energy is given by the following expression according to equation 2.91,

$$\Sigma_{11}^c(t) = \chi_{ex}n_2 + \chi_{ct}n_3 \quad (4.1)$$

$$\Sigma_{22}^c(t) = -(1 - n_1)\chi_{ex} \quad (4.2)$$

$$\Sigma_{33}^c(t) = -(1 - n_1)\chi_{ct}. \quad (4.3)$$

Parameters  $\chi_{ct}$  and  $\chi_{ex}$  are respectively the CT state and exciton couplings. Population  $n_i = \Im m G_{ii}^<(t, t)$  is the time-resolved carrier distribution on orbital  $i$ . In the Hartree-Fock self-energy terms considered, the contributions due to electron-electron type interactions are neglected. This simplification allows us to focus only on excitonic effects, without mixture with  $e - e$  type interactions.

Several experimental and theoretical studies estimated that excitons binding energy varies from 0.1 eV to 1.0 eV and CT binding energy is about  $\sim 0.1$  eV [113]. Despite the wide range of proposed mechanisms to explain charge generation process in organic semiconducting devices, from hot charge transfer [105] to exciton polarity [114], the generation of free charges in organic devices is still not fully understood.



### 4.1.2. Impact on time-resolved local density of states

The time-resolved local density of states on Figure 4.3a, shows the TRLDOS for  $\chi_{ct} = 0.3$  eV as compared to the reference  $\chi_{ct} = 0.0$  eV in the left panel. A straightforward analysis of Figure 4.3b reveals, as expected, that the generation of CT state induces a correction on the energy levels  $\varepsilon_2$  and  $\varepsilon_3$ , which corresponds to a gap correction in standard view. In fact, the presence of CT state corrects the hybridized energy levels by changing their splitting, which weakens or suppress the hybridization between LUMOs: the density of states of the anti-bonding molecular orbital is more high and its energy level is almost not affected with respect to the bonding orbital that is downshifted and less pronounced. Let us recall that the bonding and anti-bonding orbitals are formed from the hybridization of donor LUMO,  $\varepsilon_2$ , and acceptor LUMO,  $\varepsilon_3$ .

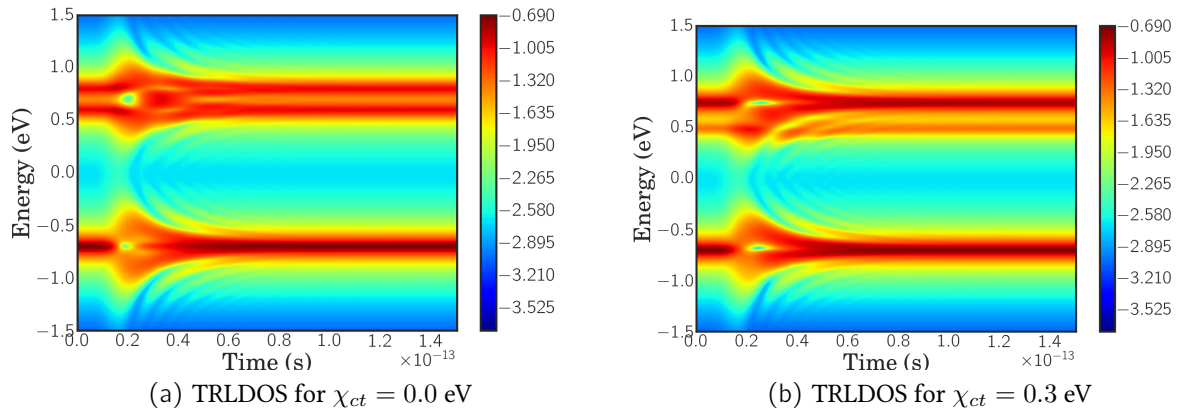


Figure 4.3.: Time-resolved local (donor) density of states:  $\chi_{ct} = 0$  eV (a) and  $\chi_{ct} = 0.3$  eV (b) with  $\chi_{ex} = 0.0$  eV.

On the other hand, the effects of exciton coupling  $\chi_{ex}$  in the donor seem to be similar to that of the CT state, but the opposite. Meaning that the hybridization is weakened and the molecular orbitals are localized on the donor and the acceptor with the bonding orbital dense compared to the anti-bonding orbital, as shown in Figure 4.4a. There is an overall downshift of the molecular orbitals induced by the exciton formation. Since the CT state and the exciton effects on the TRLDOS are opposite, they tend to compensate or compete when simultaneously present in the system, which is the most realistic case. This is shown on Figure 4.4b, where the symmetry is restored between the two peaks of the TRLDOS at the two LUMO hybridized levels.

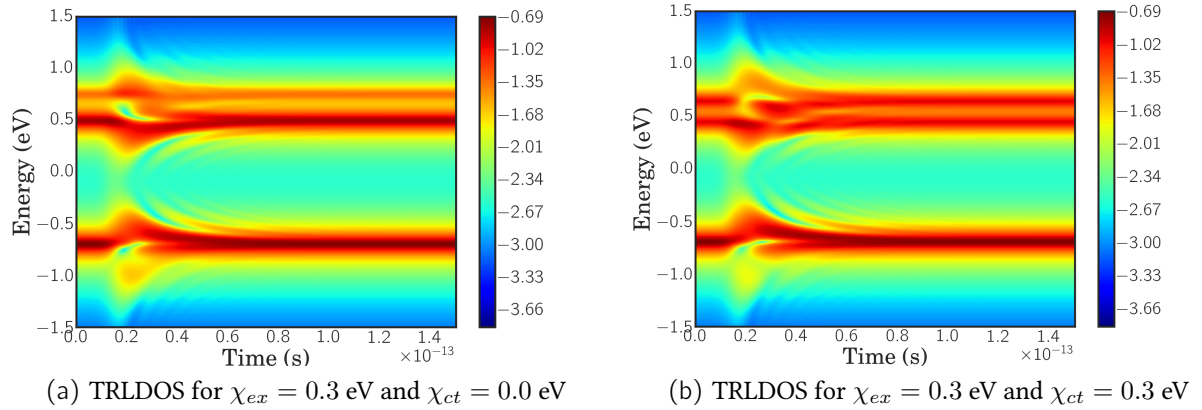


Figure 4.4.: Time-resolved local (donor) density of states.

### 4.1.3. Impact on the photocurrent

Now regarding the photocurrent represented in Figure 4.5, two effects occur when  $\chi_{ct}$  increases. Firstly, the on-pulse photocurrent frequency increases, and secondly, the photocurrent amplitude decreases. The increase in frequency describes the energy level adjustment due to CT state coupling. Since orbitals  $\varepsilon_2$  and  $\varepsilon_3$  of the molecular level spacing change with  $\chi_{ct}$ , there is a CT-induced renormalization of  $\beta$  which is proportional to the dynamical Rabi frequency in the rotating wave approximation limit. On the other hand, the decrease in the amplitude is due to the carrier binding with Coulomb interaction. Due to CT state, the rate of carrier flow is decreased, and hence the amplitude of photocurrent. One point to be noted in Figure 4.5 is the strong decrease in the peaks of the photocurrent with  $\chi_{ct}$ . This is due to the loss of hybridization. Indeed, there is an oscillating tunneling through both hybridized molecular orbitals (MO). Whenever  $\chi_{ct}$  is switched on, hybridization is no longer maximal, so that the less dense MO has a weaker tunneling rate compared to the most dense MO. The scenario is confirmed by the observation of the effect of  $\chi_{ex}$  on the photocurrent, pictured Figure 4.6. The increase of  $\chi_{ex}$  reduces the amplitude of the whole photocurrent as the effect of Coulomb electron-hole pair binding, but specifically, the amplitude of the second peak in the photocurrent is decreased or damped, and even suppressed for a high value of  $\chi_{ex}$ . This matches well with the previous analysis of TRLDOS, where we have shown the effect of  $\chi_{ex}$  on the hybridization strength, compared to the case of  $\chi_{ct}$ . The switch on of  $\chi_{ex}$  induces an increase of the interferences at the donor level with the increase of the on-top oscillation frequency.

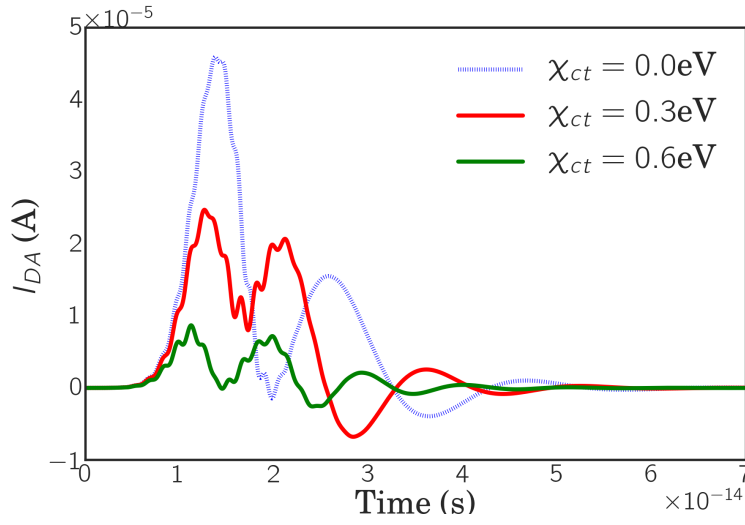


Figure 4.5.: Time-resolved photocurrent for  $\chi_{ct} = 0.0, 0.3$  and  $0.6$  eV with exciton coupling  $\chi_{ex} = 0$  eV.

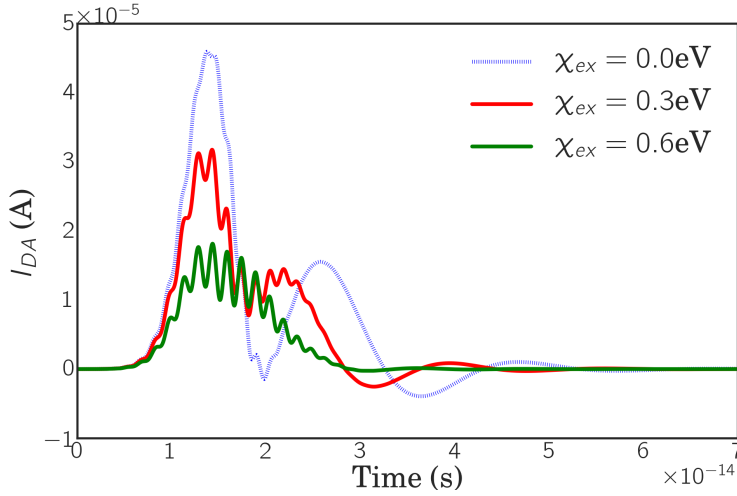


Figure 4.6.: Time-resolved photocurrent for  $\chi_{ex} = 0.0, 0.3$  and  $0.6$  eV with CT coupling  $\chi_{ct} = 0.0$  eV.

There is also a strong damping of the off-pulse oscillation. The damping mainly depends on the localization of the state on the donor or the acceptor. The damping could raise a confusion about the suppression of the second peak in the photocurrent. One can think that since the broadening induces a damping of the off-pulse oscillation, it could also suppress the second peak in the pho-

to current. But if that was the case, we would have gotten a smaller or even tiny peak, not totally suppressed.

In the realistic case where  $\chi_{ct}$  and  $\chi_{ex}$  are non-zero, all effects mix up, and there happens a competitive behavior of exciton and CT state in the transport mechanism. Figure 4.7 presents the time-resolved photocurrent for three configurations:  $\chi_{ct} < \chi_{ex}$ ,  $\chi_{ct} = \chi_{ex}$  and  $\chi_{ct} > \chi_{ex}$ . Whenever  $\chi_{ct} < \chi_{ex}$ , the exciton-induced effect takes over and vice versa, so in fact, there is a clear competitive behavior in the transport mechanism that is reflected in the photocurrent shown Figure 4.7. Especially, hybridization loss and resulting state localization is the major effect. Binding and anti-binding hybridization occur again for  $\chi_{ct} = \chi_{ex}$ , which is reflected in the photocurrent. Especially the molecular orbitals localization and their dissymmetric amplitudes are the major effects. Since for  $\chi_{ct} < \chi_{ex}$  there is a strong decrease in the second peak of the photocurrent as a consequence of the reduction of amplitude of the anti-bonding MO with respect to the bonding MO. The effect is reversed in the case  $\chi_{ct} > \chi_{ex}$ , where the bonding MO is denser. The compensation between bonding and anti-bonding MO arise when  $\chi_{ct} = \chi_{ex}$ , and is reflected in the photocurrent.

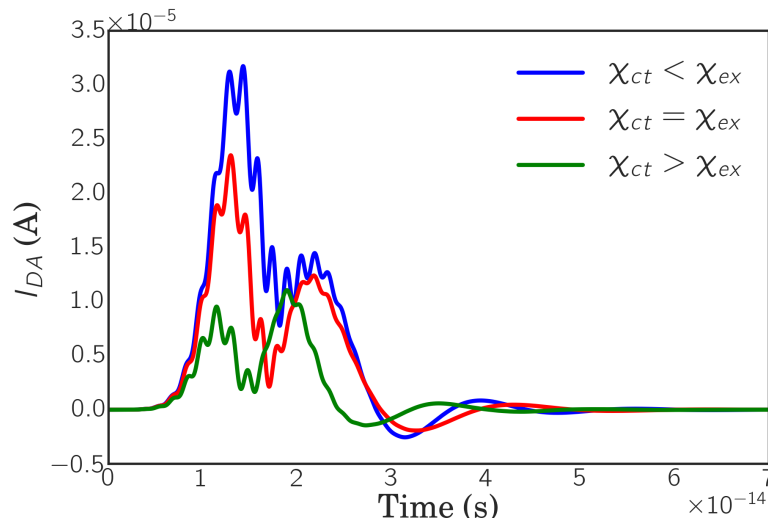


Figure 4.7.: Time-resolved photocurrent: exciton and CT state competition with  $\chi_{ex} = 0.3$  eV.

## 4.2. Analyzing charge transfer

### 4.2.1. Positioning of the study

According to the experimental design of donor-acceptor junctions for solar device applications, the practical case is  $\chi_{ct} < \chi_{ex}$ , because electron and hole are much closer in the exciton configuration than CT one, so the attraction strength is greater in the exciton than the CT state. Since the size of the donor and acceptor materials defines the separation between the electron and hole in the donor, we argue here that organic molecules or semiconducting materials with tiny donor size (for short diffusion length exciton) will tend to bring the CT state in competition with the exciton such that the global effect of electron-hole bound pairs on transport could be annihilated in such nanosystems. This observation resets the question of driving energy and exciton binding energy in a molecular junction, indeed the topic is actually a hot debate. Let us recall here that the *driving energy* is the energy offset of the donor and acceptor LUMOs, and that the Coulomb attraction energy between electrons and holes is known as the *exciton binding energy* ( $E_B \sim \chi_{ex}$ ). In inorganic semiconductors, dielectric constants,  $\epsilon$ , are of the order  $\geq 10$ , and induce a binding energy of around  $0.01eV$ . Such an exciton binding energy is smaller compared to the thermal background energy  $k_B T$  at room temperature which is around  $0.026eV$ , meaning that the electron and hole are easily separated at these temperatures. The case of organic semiconductors is radically different. Organic materials usually have smaller dielectric constants, of about  $2 - 4$ . As a result, exciton binding energies are typically much larger  $\sim 0.3 - 0.5eV$  and require a so-called driving energy in addition to the thermal energy to generate free charge carriers. This is why organic solar cells require an heterojunction, an interface between two different types of materials (donor and acceptor for instance). This heterojunction provides a difference in free energy that can drive charge separation in order to work properly[115].

In fact, some studies suggest that the most promising strategy for the design of efficient solar cells is to favor a low driving force for enhancing charge separation rate from the relaxed CT state [116]. Such an approach includes optimizing the parameters between acceptor and donor molecules, as inter-chromophore coupling, charge delocalization, and charge mobility, as well as reducing the reorganization energy [41, 117, 118]. Meanwhile, there are proposals for a large driving energy with wide band gap donor and low gap non-fullerene type acceptor [119]. Are these proposals in contradiction? Let us make a point on the question and get close to a consensus.

### 4.2.2. Dynamical driving energy and exciton binding

In this section, we want to give a sketch of insight into the interplay between exciton and CT state, and their contribution to charge in separation at D-A interfaces in nanoelectronics. There are several reviews in the literature with active contribution and contradictory opinions. But one striking element is that de-

pending on the material geometry, doping and gap, there is most of the time no agreement on the value of the driving energy inside the device, and neither on exciton binding. It is accepted in general that, whenever exciton binding energy is smaller than driving energy, excitons dissociate into free carriers. And the inverse will give an exciton dominated, free-carrier and exciton mixture [120].

The current contribution is to elucidate the effects of bound electron-hole pairs at junction interfaces through the correlation between driving energy and exciton binding energy, which will help to design efficient optoelectronics.

We introduce the Coulomb-induced shift of each energy level  $i$  defined from the Hartree-Fock self energy as

$$\Delta\varepsilon_i^{HF} = \Sigma_{ii}^c = \varepsilon_i^{HF} - \varepsilon_i, \quad (4.4)$$

where  $\varepsilon_i^{HF}$  is the energy level  $\varepsilon_i$  after correction,  $\Delta\varepsilon_i$  gives the direction of the shift induced by its sign and the amount of the shift.

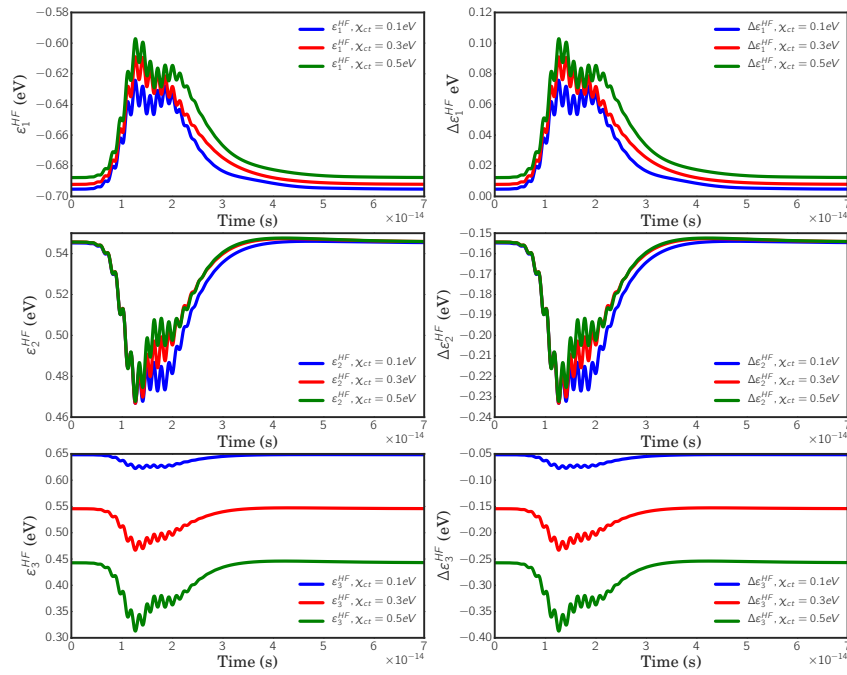


Figure 4.8.: CT state and exciton competition seen through energy level corrections. The three left panels ( $\varepsilon_1^{HF}$ ,  $\varepsilon_2^{HF}$  and  $\varepsilon_3^{HF}$ ) represent the time-dependent corrected energy levels induced by e-h pair coupling on  $\varepsilon_1$ ,  $\varepsilon_2$  and  $\varepsilon_3$  orbitals. The three right panels ( $\Delta\varepsilon_1^{HF}$ ,  $\Delta\varepsilon_2^{HF}$  and  $\Delta\varepsilon_3^{HF}$ ) are the corresponding energy corrections. We take  $\chi_{ex} = 0.3$  eV.

Figure 4.8 shows on its left panel the corrected energy levels of the D-A junction including excitonic effects with  $\chi_{ex} = 0.3$  eV. The right panel of the same figure shows the corresponding correction to each energy level. It is clear that as  $\chi_{ct}$  increases, both levels  $\varepsilon_2$  and  $\varepsilon_3$  are shifted downward, and  $\varepsilon_3$  is more strongly shifted as shown by the plot of  $\varepsilon_3^{HF}$  and  $\Delta\varepsilon_3^{HF}$  as function of  $\chi_{ct}$  with respect to  $\Delta\varepsilon_2^{HF}$ . On another side, the effect of the exciton binding strength is enhanced on level  $\varepsilon_2$ , since the variation of  $\varepsilon_2^{HF}$  and  $\Delta\varepsilon_2^{HF}$  as a function of time shows that whenever  $\chi_{ct} < \chi_{ex}$ , they are strongly shifted. The exciton binding energy as shown is a dynamical parameter, that varies as a function of time and pulse intensity.

In order to discuss charge separation, the key parameter is the change of  $\varepsilon_3^{HF}$  with respect to  $\varepsilon_2^{HF}$ :

$$\Delta\varepsilon_{32}^{HF} = \varepsilon_3^{HF} - \varepsilon_2^{HF} = -(1 - n_1)(\chi_{ct} - \chi_{ex}). \quad (4.5)$$

Such a quantity characterizes the dynamical energy shift between donor and acceptor LUMOS induced by e-h correlations, it is represented in Figure 4.9. We identify this shift as the dynamical driving energy governing how the junction responds when excited by the laser pulse.

Figure 4.9 confirms the competitive nature of the exciton and CT states. There are three distinct regimes for the device operation. For  $\chi_{ct} < \chi_{ex}$ , we have a positive exciton driving energy,  $\Delta\varepsilon_{32}^{HF} > 0$ ; for  $\chi_{ct} > \chi_{ex}$ , we have a negative exciton driving energy,  $\Delta\varepsilon_{32}^{HF} < 0$ . The buffering regime is when exciton and CT couplings compensate exactly,  $\chi_{ct} = \chi_{ex}$ , and the exciton induced driving energy is exactly canceled  $\Delta\varepsilon_{32}^{HF} = 0$ . The most realistic configuration is the first one, where we have a positive driving energy for  $\chi_{ct} < \chi_{ex}$ . It is also the most commonly used in the literature.

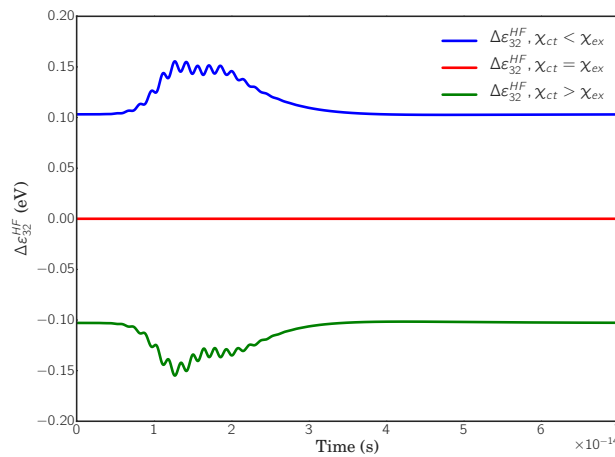


Figure 4.9.: Time-resolved driving energy  $\Delta\varepsilon_{32}^{HF}$  for  $\chi_{ex} = 0.3$  eV.

It shows once again the competitive nature of exciton and CT states in the nanosystem. Also, we can notice that the correction induced by the bound e-h pair interaction, under a time-dependent field applied, is time-dependent and depends on the field parameters and the internal quantum dynamics of the carriers, namely the carriers distribution on each energy level. A reminder, all field parameters are kept constants during this simulation. It could be interesting to think of deepening the study on the dependence of the exciton driving energy,  $\Delta\varepsilon_{32}^{HF}$ , depending on the field parameters and the nanojunction geometry.

To further analyse the effect of different gaps in donor and acceptor, we introduce an offset between the two LUMOs:

$$\delta_{DA} = \varepsilon_3 - \varepsilon_2. \quad (4.6)$$

We investigate the time-resolved photocurrent as a function of  $\delta_{DA}$  for two  $\chi_{ct}$  values, fixing  $\chi_{ex} = 0.3$  eV, as shown Figure 4.10. For positive values of the  $\delta_{DA}$  the photocurrent amplitude is higher compared to the region of negative  $\delta_{DA}$ , as shown in Figure 4.10. The global behavior of the photocurrent is the same for the two values of  $\chi_{ct}$ , but the whole response is shifted toward high  $\delta_{DA}$  values when  $\chi_{ct}$  increases.

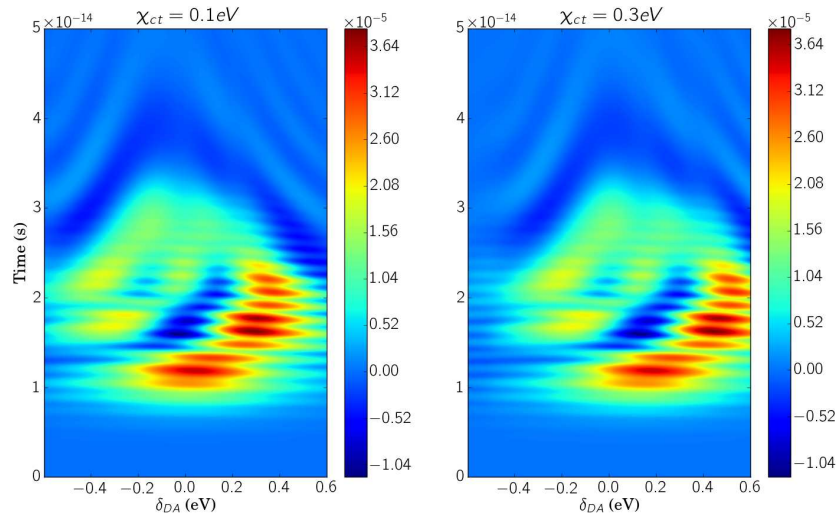


Figure 4.10.: Time-resolved photocurrent as a function of LUMO energy offset,  $\delta_{DA}$ , for  $\chi_{ct} = 0.1$  eV and  $0.3$  eV, with  $\chi_{ex} = 0.3$  eV.

The global dynamics is depicted in the photocurrent integrated over time shown Figure 4.11. It confirms that curves are shifted towards  $\delta_{DA}$  positive values as  $\chi_{ct}$  increases. There is almost a plateau around  $\delta_{DA} = 0.0$  eV where the photocurrent amplitude is almost insensitive to CT state and exciton binding.



Each curve also exhibits a peak inside the region of  $\delta_{DA}$  positive values: at this specific operating point, there is a compensation between the level offset and bound electron-hole effects. This counter-intuitive behavior was also observed in molecular photocells [108].

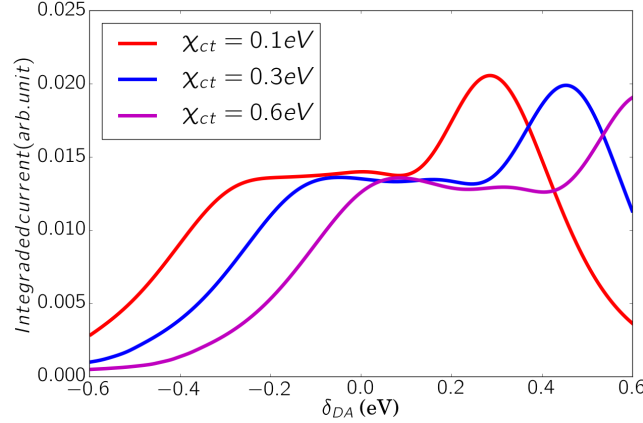


Figure 4.11.: Integrated photocurrent as a function of LUMO energy offset,  $\delta_{DA}$ , for  $\chi_{ct} = 0.1$  eV and 0.3 eV with  $\chi_{ex} = 0.3$  eV

### 4.2.3. Characteristic timescales of charge transfer

In this section, numerical simulations are deeper exploit to extract an “exciton to CT state” characteristic time.

We use the distribution of carrier population on each state as a function of time shown in Figure 4.12 (upper panel). We then form the product  $(1 - n_1)n_i$  that represents the probability of formation of the exciton for  $i = 2$  and of the CT state for  $i = 3$ , these are plotted in Figure 4.12 (lower panel).

Using the bound e-h pair distributions, we propose to evaluate physical quantities that could compare with experiments, as the photoinduced interfacial electron transfer time that may be interpreted as the time it takes to the exciton to be transferred to the D-A junction interface up to the formation of the CT state.

Since carriers flow from the donor to the acceptor oscillating as shown Figure 4.12, we thus roughly define the two times at which one may consider that exciton then CT state exist. The first time,  $\tau_{ex}$ , is the time at which the distribution  $(1 - n_1)n_2(t)$  reaches, on the leading edge, half its maximum value, that is closed to the average probability of exciton formation. The second time,  $\tau_{ct}$ , is defined similarly on the leading edge of the distribution  $(1 - n_1)n_3(t)$  as the average probability of CT state formation. The difference  $\tau_{tr} = \tau_{ct} - \tau_{ex}$  could be interpreted as the photoinduced interfacial electron transfer time.

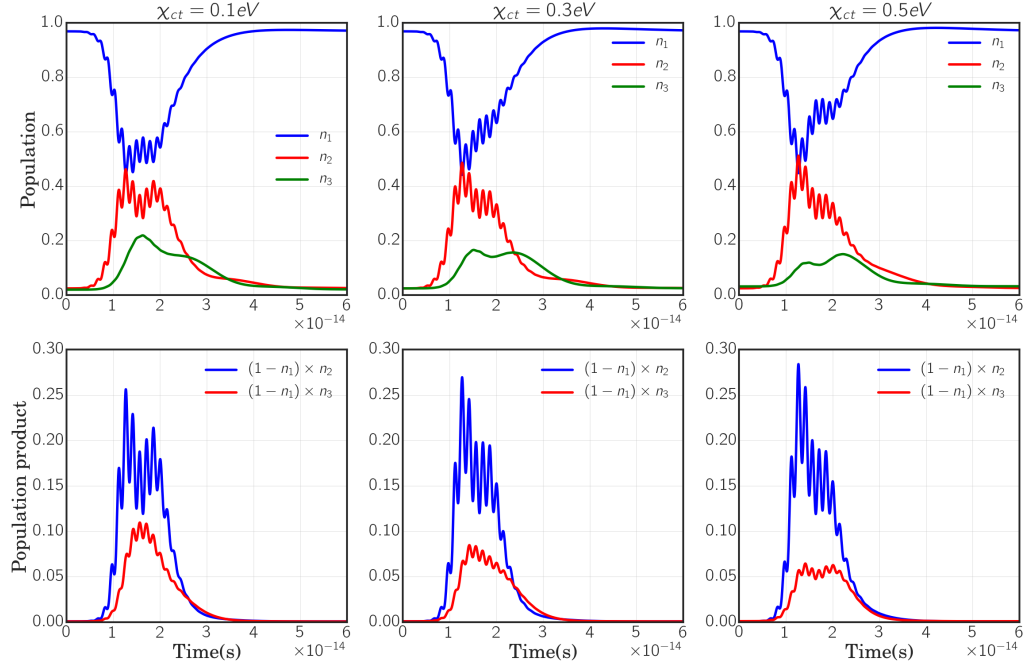


Figure 4.12.: Populations  $n_i$  and product distribution  $(1 - n_1)n_i$  as a function of time for three different values of  $\chi_{ct}$ . Parameter  $\chi_{ex}$  is set to 0.3 eV.

Figure 4.13 shows  $\tau_{tr}$  as a function of  $\chi_{ct}$ . The transfer time varies very little in the parameter range. The present investigation leads to an average value  $\langle \tau_{tr} \rangle$  of 3.5 fs. This value is in reasonable agreement with predictions for photoinduced charge transfer timescales. For some of them, the timescale was found to vary from a few femtoseconds to hundreds of picoseconds, depending on the sensitizer molecule [121], and others found that the initial stage to form the CT excitation occur on a timescale of tens of femtoseconds [14]. Still, there is an overlap in all predictions. However, the predictive value of  $\tau_{tr}$  obtained here might increased is nanosystems where vibrations could assist transport.

We finally propose to evaluate the lifetime of CT state,  $\tau_{lifetime}$ , by taking the width at half-maximum of the  $(1 - n_1)n_3$  distribution as a function of time from Figure 4.12. The CT lifetime is shown Figure 4.14 as a function of  $\chi_{ct}$ , the CT state binding strength. The CT state lifetime,  $\tau_{lifetime}$ , is found to be of the order of 18 – 20 fs. Figure 4.14 exhibits two regions: for  $\chi_{ct} < 0.3$  eV where  $\tau_{lifetime}$  is smaller compared to the region for  $\chi_{ct} > 0.3$  eV. Maximum is obtained for  $\chi_{ct} > 0.3$ , and the two regions correspond respectively to  $\chi_{ct} < \chi_{ex}$  and  $\chi_{ct} > \chi_{ex}$ .

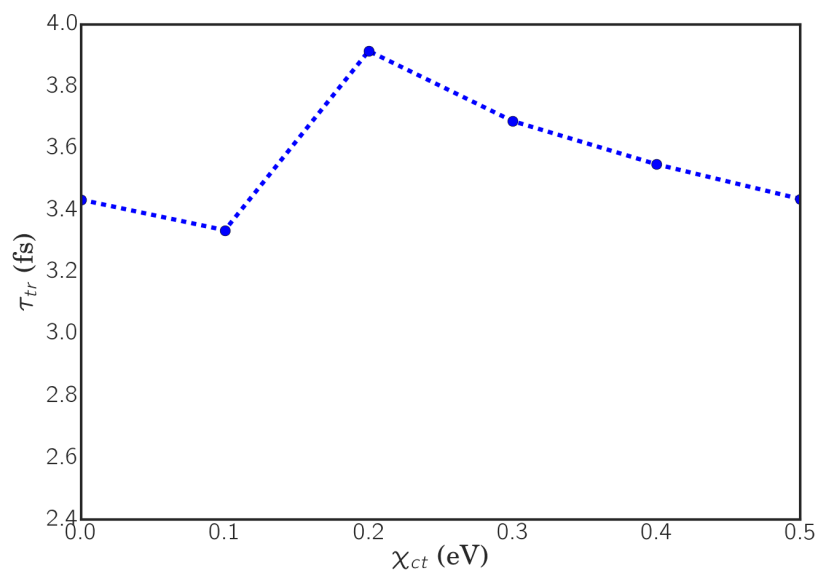


Figure 4.13.: Evolution of the photoinduced interfacial electron transfer time,  $\tau_{tr}$ , as function of  $\chi_{ct}$ , with  $\chi_{ex}$  set to 0.3 eV.

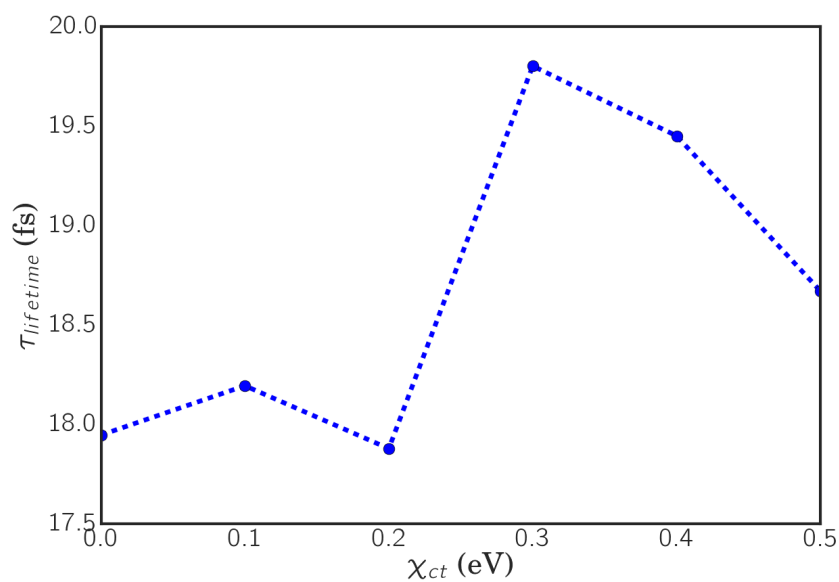


Figure 4.14.: Lifetime of CT state,  $\tau_{lifetime}$ , as function of  $\chi_{ct}$ , with  $\chi_{ex} = 0.3$  eV.

#### 4.2.4. Proposal for measuring of the driving energy

We expose a simple method to track energy level corrections induced by electron-hole correlations by means of photocurrent spectroscopy. In fact, the use of the photocurrent response of the system to a range of optical pump frequencies is a good way to track. It will provide us with information on the gap dynamics, and gives an insight into carrier distribution. For such an experiment we also need to consider the correction induced on the  $\varepsilon_1$  level, which is smaller but contribute to the global gap shrinking in the case studied in this paragraph. The time-resolved photocurrent of the molecular system as varying the laser frequency is shown on Figure 4.15. The laser energies at which the photocurrent is optimized, around  $\pm Eg \pm \varepsilon^{HF}$ , are shifted, and spanned differently as  $\chi_{ct}$  increases with respect to  $\chi_{ex}$ . The photocurrent integrated over time is maximal for a frequency equal to the gap of the donor system, as shown in Figure 4.16.

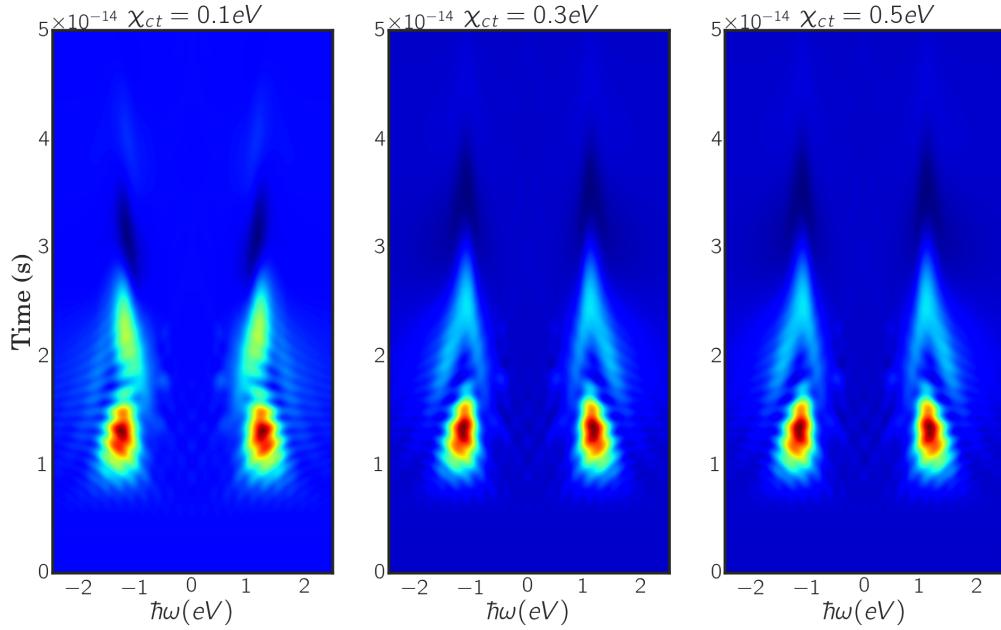


Figure 4.15.: Time-resolved photocurrent distribution as function of the gaussian pulse central energy,  $\hbar\omega$  for different  $\chi_{ct}$  with  $\chi_{ex} = 0.3$  eV.

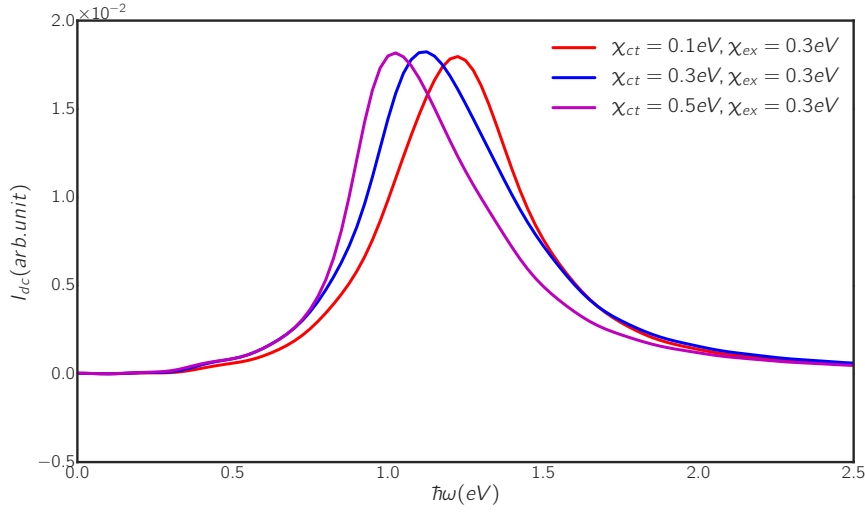


Figure 4.16.: Integrated photocurrent as function of the gaussian pulse central energy,  $\hbar\omega$ .

#### 4.2.5. Conclusions for molecular junction design

Coming back to the initial question of what controls carrier separation at a D-A nanojunction interface: two conclusions are clear, regarding the analysis in this section. First, the excitonic driving energy is not a constant parameter during carrier dynamics. We thus conclude that the notion of driving energy from the standard view should be revised. Secondly, not only the excitonic driving energy is an additional driving energy to HOMO-LUMO donor gap, and LUMOs energy-offset built-in during the design, but also it depends on the strength of the CT and exciton bindings and their competitive nature. We further infer from these calculations that there exists, for each nanosystem, a limit of the ratio between the CT and exciton binding strength, for which the excitonic induced driving energy compensates the static driving energy (energy-offset). Below and above that limit ratio, the nanosystem operates in two distinct and sometimes opposite regimes. Since the excitonic driving energy is time-dependent, it implies that the driving energy is not a known parameter to input during the design, but an output parameter to be found from dynamical simulations. Of course, for stationary transport applications, it is possible to take the static driving energy as an input parameter. Similarly for ultrafast experiments, it might be possible with the help of numerical simulations to predict the exact value of the driving energy. This finding gives at least a point of clarification. In fact, it tells us that depending on geometry and field parameters, some nanodevices might need the introduction of a static driving energy (HOMO-LUMO offset), and others not. For

example, there is a recent proposal to use non-fullerene acceptor materials and a wide bandgap (WBG) donor in order to create a well-matched donor-acceptor pair with a low band gap (LBG) non-fullerene small-molecule acceptor. This proposal provides a great potential to realize high-performance non-fullerene small-molecule organic solar cells [119]. Another study suggested that the strategy for the design of efficient solar cells may be to accept a low driving force in favor of optimizing the open-circuit voltage, and then to aim at enhancing the subsequent charge separation rate from the relaxed CT state [116]. In fact, taking an WBG donor and an LBG acceptor means an increase in the driving energy. Choosing low or high driving energy/force is considered regarding the geometry of the device, in order to have an excitonic binding energy smaller than the driving energy. Such nanosystems are optimized if one considers the dynamical nature of the excitonic induced driving energy and the two specific operating regimes that occur since it has been shown that charge transfer dynamics takes place on hundreds of femtosecond scale.

### 4.3. Two-pulse photocurrent simulations

In this section, we consider the optoelectronic response of the nanosystem to a sequence of two sequential pulses. We expect from this investigation to extract intramolecular dynamics understanding or parameters. The related method is the standard pump-probe spectroscopy technique but in this case, we measure the photocurrent instead of the absorption spectrum. This method also permits to track photoinduced correlation effects during dynamics. Additionally, a focus is made on how such dynamic is modified by bound electron-hole pair interactions.

We investigate the photoresponse of the junction to a sequence of pulse pairs as a function of the delay between the pump and the probe pulses, in order to study the impact of exciton and CT state on the integrated photocurrent,  $I^{dc}$ . Indeed, as the transient photocurrent might be difficult to measure in the terahertz regime, and even impossible with standard electronics on sub-picosecond timescales, the commonly measured photocurrent is the integrated one. For simplicity let us call the integrated photocurrent, *the direct current*, and define it as follow:

$$I^{dc} = \frac{1}{\Delta t} \int_0^{\Delta t} dt' I_{DA}(t'), \quad (4.7)$$

with  $\Delta t$  the time integration window.

By considering a pair of two identical excitation pulses with a delay time  $\tau_{del}$ , we monitor the photocurrent as shown on Figure 4.17.

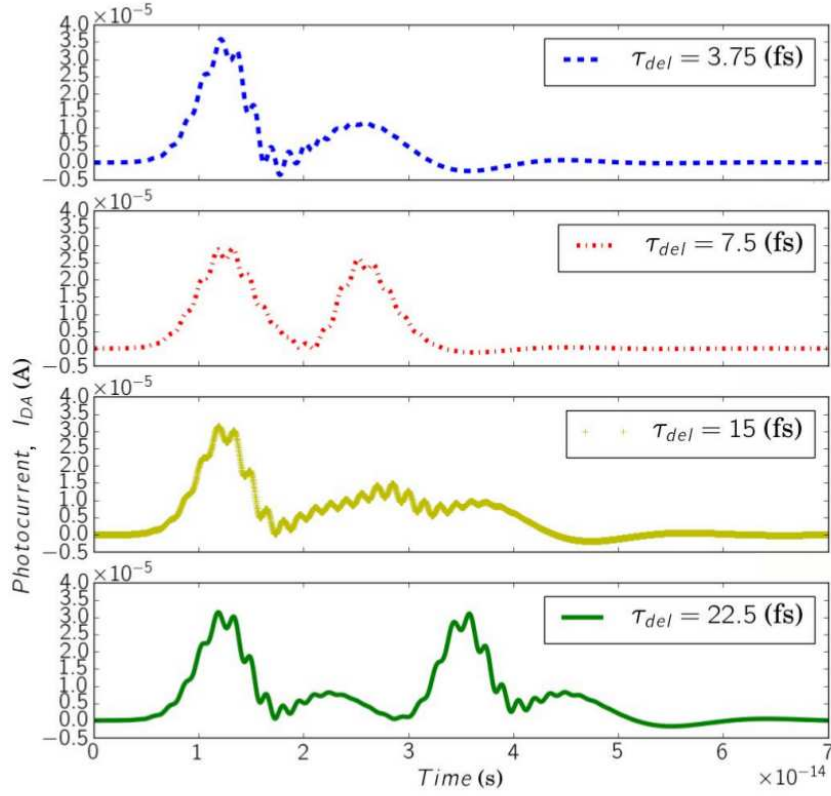


Figure 4.17.: Photocurrent response to a sequence of two pulses for different delays,  $\tau_{del}$ , with  $\chi_{ct} = 0.1\text{eV}$  and  $\chi_{ex} = 0.3\text{eV}$ .

For small delays  $\tau_{del} < 23\text{fs}$ , there are interferences of the wave functions inside the overlap of the two pulses. These interference effects induce the reduction of the current amplitude. But for larger delay, the nanosystem response to the pulse sequence is divided into two separated parts that correspond to the two separated nanosystem responses to each pulse. This is because the system has the time to relax before the second pulse arrives. Thus, there is no longer interference between the two signals. The map of the time-resolved photocurrent as a function of the delay shows these interference patterns in Figure 4.18. These maps reveal that the interference amplitude is increased as the CT binding is increased. In fact, the system has its own relaxation time called here  $\tau_{relax}$ . Whenever  $\tau_{del} < \tau_{relax}$ , there are interferences, and inversely when  $\tau_{del} > \tau_{relax}$ , the two pulses give independent responses.

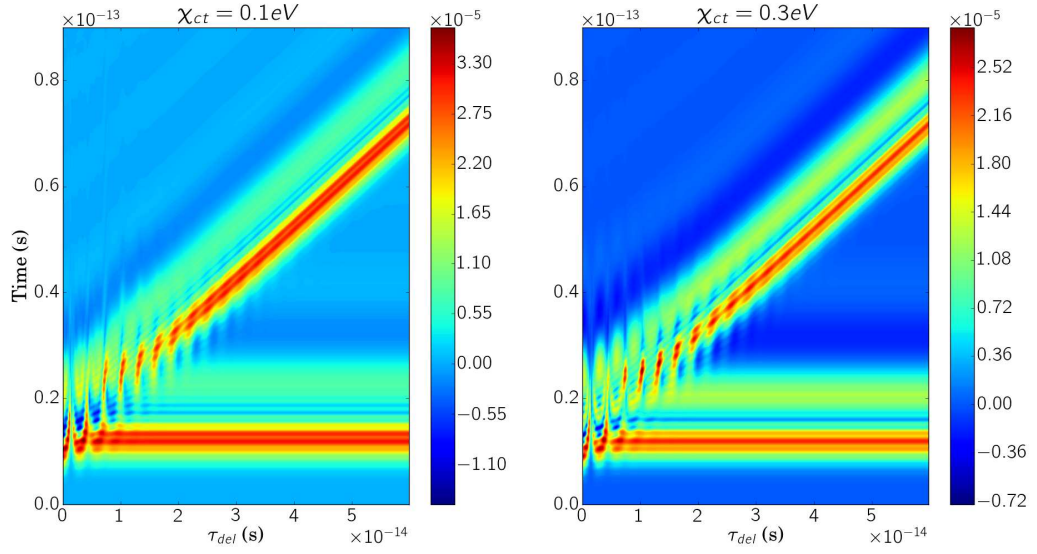


Figure 4.18.: Maps of the time-resolved photocurrent as function of the delay,  $\tau_{del}$ , for two values of  $\chi_{ct}$ , with  $\chi_{ex} = 0.3$  eV.

The information on carrier dynamics induced by the pulse sequence is contained in the limit  $\tau_{del} < \tau_{relax}$ , since physical information for  $\tau_{del} > \tau_{relax}$  could be obtained from a single pulse dynamics, as discussed above and in Chapter 3. By integrating over time the time-resolved photocurrent maps of Figure 4.18, we get the direct current,  $I^{dc}$ , as function of the delay,  $\tau_{del}$ , for three different values of  $\chi_{ct}$  ( $\chi_{ex}$  fixed), as presented Figure 4.19. As expected,  $I^{dc}$  amplitude is reduced when  $\chi_{ct}$  increases.

All plots exhibit a similar dynamics. First, an oscillation with a global increasing current, and next, a saturated regime with constant values for the direct photocurrent. This oscillatory part is analyzed from Fast Fourier Transform, as depicted in Figure 4.20. The oscillation frequency is a kind of beating frequency, and the drop of  $I^{dc}$  as  $\tau_{del}$  tends to zero is the modification in the resulting wave amplitude, thus the dynamical Rabi frequency. The different frequencies in Figure 4.20 correspond to the modification of the dynamical Rabi frequency, and thus a characteristic of the intramolecular LUMO tunneling oscillations. The oscillatory behavior corresponds in fact to interferences inside the donor material/molecule, which are clearly visible in Figure 4.18.

On the other hand, when the delay overrides the relaxation time,  $\tau_{del} > \tau_{relax}$ , the effect of the second pulse is to double the single pulse induced *direct current*,  $I_0^{dc}$ , and to reach an asymptotic value,  $I_{sat}^{dc} \simeq 2I_0^{dc}$ . This value  $2I_0^{dc}$  may be compared to  $I^{dc}(\tau_{del} = 0)$  that corresponds to the response of a single pulse but with a doubled amplitude. On Figure 4.19,  $I^{dc}(\tau_{del} = 0) < I_{sat}^{dc} \sim 2I_0^{dc}$ . This difference is effective for ballistic and weakly interacting systems. For instance, CT effects



are to considerably reduce the value of  $I_{sat}^{dc}$ . However, if  $\tau_{del}$  is of the same order of or smaller than  $\tau_{relax}$ , the current is different, but still smaller than  $2I_0^{dc}$ .

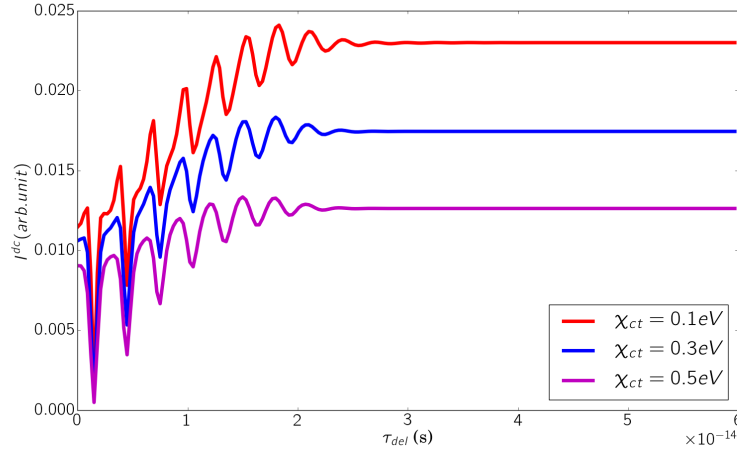


Figure 4.19.: Direct current,  $I^{dc}$ , for different  $\chi_{ct}$  values, with  $\chi_{ex} = 0.3eV$ .

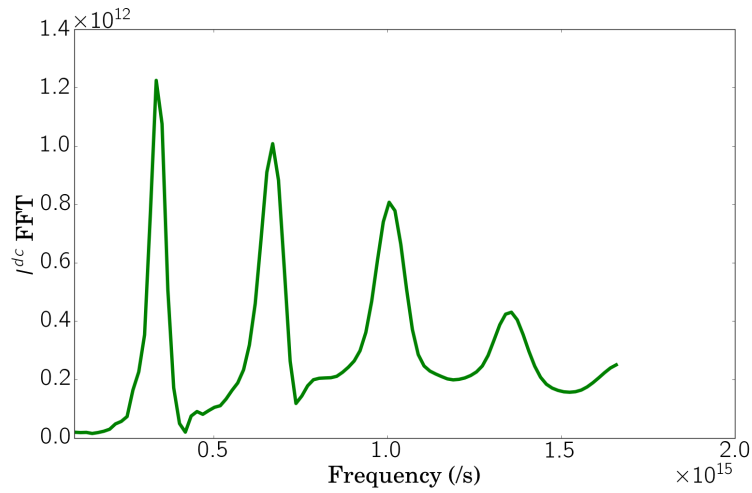


Figure 4.20.: Fast Fourier Transform (FFT) of  $I^{dc}$  oscillatory part.

## 4.4. Discussion

Additionally to what have been said so far, the integrated photocurrent,  $I^{dc}$ , as a function of the delay, shown on Figure 4.19, has a higher amplitude for the

configuration where exciton interaction is stronger with respect to the CT state interaction. Meaning that the transmission function of nanosystems in this configuration is better optimized. This observation is in line with our analysis, and corresponds to the most realistic situation in donor-acceptor nanojunction design, since usually, the exciton binding is greater than the CT state binding. So, one should control the dimensions of the donor material to fulfill this previous condition. Though one should consider the implication of this analysis regarding the configuration of the donor-acceptor junction. For planar configuration it might be easier to control the bound electron-hole pair separations, thus the binding energy. It should not be the case for bulk type heterojunction donor-acceptor blends since bound electron-hole pair separation varies a lot inside the material. In such a case, only the average binding energy of the junction should be considered and the donor-acceptor mixing ratio might be deterministic [122].

There are additional constraints to care about in the design of donor-acceptor junctions which are beyond the framework of this thesis. Exciton diffusion length, even not explicitly taking into account in this work, is an important parameter to consider. Indeed, depending on the exciton diffusion length, one wants to match the donor material length in such a way that recombination and other loss mechanisms can be avoided inside the donor material. In fact, if the donor material length is greater than the exciton diffusion length, exciton will not be able to reach the interface with the acceptor material, before it recombines. Such a situation generates reduction of the nanojunction efficiency. Hence globally, there is a compromise to find between the exciton diffusion length, the exciton binding strength, the driving energy and the donor-acceptor mixing ratio. This study shows that the main difficulty comes from the fact that a efficient design shall rely on working conditions, whatever they are stationary or time-dependent.

## Conclusion

In this Chapter, we focus on the time-resolved excitonic effects on carrier dynamics and on the internal nanojunction energy and time scales. We pointed out the competitive nature of the CT and local exciton dynamics regarding the strength of their binding and proposed a pathway for the choice of the LUMO energy splitting in order to optimize nanosystem efficiency. Finally, two contributions were also made towards experiments, using single and two pulse spectroscopic techniques.

## CONCLUSION

This work has promoted advances on three main aspects: theoretical development, numerical calculation, and applications to molecular optoelectronics. For the theoretical development, we investigated the NEGF based Wave Function technique and introduced its extended form (NEGF-WF) that accounts for an efficient treatment of bound electron-hole pair correlations in nanosystems. We have shown how one can compute photocurrent and time-resolved electron density within the proposed framework. On the theoretical side, the added value to the initial Wave Function technique is its extension to the treatment of Coulomb correlations at the Hartree-Fock level. After theoretical development, we proposed a non-exhaustive set of efficient and optimized algorithms for the numerical simulations. Using these algorithms, we have shown that it is possible to unravel some internal quantum properties of a nanojunction mainly through the time-resolved local density of states and the photocurrent. For instance, the coupling strength between the two molecules in a nanojunction could be measured from their signature in the frequencies of the oscillating photocurrent signal. Similarly, the coupling of the nanojunction to the contacts could be measured from the photocurrent damping. Aside from these experimental proposals, interesting physical effects have been revealed by the time-resolved density of states: the Floquet-like state generation and the dynamical Rabi shift of the energy levels. Finally, the effects of the electron-hole pair bonding to the dynamics is a modulation of interface driving energy, imposing operating regimes for charge transfer at donor-acceptor junctions. It also reveals counter-intuitively that highly efficient charge transfer bonding with respect to exciton bonding gives rise to efficient nanodevice. Moreover, it might be possible to capture, generate, shape and control terahertz frequencies from the intramolecular dynamics through an externally applied electromagnetic field.

The theoretical-numerical framework globally proposed might be applicable to ultrafast quantum transport in most nanosystems except when the molecular vibrations and bosonic interactions are too high. A continued extension of NEGF-WF methodology should include these interactions for a more precise description and a wide range of applicability.

The whole work provides us with a valuable tool for ultrafast quantum transport simulation. It also gives indeed an insight into the relevance of transient dynamics in the understanding of time-resolved optoelectronic nanodevice operations and opens the pathway towards ultrafast nanodevice design for future technologies.

## BIBLIOGRAPHY

1. MENTOVICH, E. D., ROSENBERG-SHRAGA, N., KALIFA, I., *et al.* Gated-Controlled Rectification of a Self-Assembled Monolayer-Based Transistor. *J. Phys. Chem. C* **117**, 8468–8474. ISSN: 1932-7447 (Apr. 2013) (cit. on p. [11](#)).
2. DIEZ-PEREZ, I., LI, Z., GUO, S., *et al.* Ambipolar Transport in an Electrochemically Gated Single-Molecule Field-Effect Transistor. *ACS Nano* **6**, 7044–7052. ISSN: 1936-0851 (Aug. 2012) (cit. on p. [11](#)).
3. XU, XIAO, YANG, X., *et al.* Large Gate Modulation in the Current of a Room Temperature Single Molecule Transistor. *J. Am. Chem. Soc.* **127**, 2386–2387. ISSN: 0002-7863 (Mar. 2005) (cit. on p. [11](#)).
4. LORTSCHER, E., GOTSMANN, B., LEE, Y., *et al.* Transport Properties of a Single-Molecule Diode. *ACS Nano* **6**, 4931–4939. ISSN: 1936-0851 (June 2012) (cit. on p. [11](#)).
5. AVIRAM, A. & RATNER, M. A. Molecular rectifiers. *Chemical Physics Letters* **29**, 277–283. ISSN: 0009-2614 (1974) (cit. on p. [11](#)).
6. MARCUS, R. A. Electron Transfer Reactions in Chemistry: Theory and Experiment (Nobel Lecture). *Angewandte Chemie International Editions in English* **32**, 1111–1121 (cit. on p. [11](#)).
7. LÖRTSCHER, E., CISZEK, J. W., TOUR, J., *et al.* Reversible and Controllable Switching of a Single-Molecule Junction. *Small* **2**, 973–977 (cit. on p. [12](#)).
8. KONISHI, T., KIGUCHI, M., TAKASE, M., *et al.* Single Molecule Dynamics at a Mechanically Controllable Break Junction in Solution at Room Temperature. *J. of the American Chemical Society* **135**. PMID: 23072537, 1009–1014 (2013) (cit. on p. [12](#)).
9. FÈVE, G., MAHÉ, A., BERROIR, J.-M., *et al.* An On-Demand Coherent Single Electron Source. **316**, 1169–72 (June 2007) (cit. on p. [12](#)).

10. BOCQUILLON, E., FREULON, V., BERROIR, J.-M., *et al.* Coherence and Indistinguishability of Single Electrons Emitted by Independent Sources. *Science*. ISSN: 0036-8075. doi:[10 . 1126 / science . 1232572](https://doi.org/10.1126/science.1232572). eprint: <http://science.sciencemag.org/content/early/2013/01/23/science.1232572.full.pdf>. <<http://science.sciencemag.org/content/early/2013/01/23/science.1232572>> (2013) (cit. on p. 12).
11. BRISKER, D. & PESKIN, U. Charge-transport-induced dissociation in donor-bridge-acceptor complexes. *The J. of Chemical Physics* **129**, 244709 (2008) (cit. on p. 12).
12. ESPOSITO, M. & GALPERIN, M. Self-Consistent Quantum Master Equation Approach to Molecular Transport. *The J. of Physical Chemistry C* **114**, 20362–20369 (2010) (cit. on p. 12).
13. POZNER, R., LIFSHITZ, E. & PESKIN, U. Charge Transport-Induced Recoil and Dissociation in Double Quantum Dots. *Nano Letters* **14**. PMID: 25259800, 6244–6249 (2014) (cit. on p. 12).
14. HOU, J., INGANAS, O., H. FRIEND, R., *et al.* Organic solar cells based on non-fullerene acceptors. **17**, 119–128 (Jan. 2018) (cit. on pp. 12, 74).
15. TEUSCHER, J., BRAUER, J. C., STEPANOV, A., *et al.* Charge separation and carrier dynamics in donor-acceptor heterojunction photovoltaic systems. *Structural Dynamics* **4**, 061503 (2017) (cit. on p. 12).
16. SELZER, Y. & PESKIN, U. Transient Dynamics in Molecular Junctions: Picosecond Resolution from dc Measurements by a Laser Pulse Pair Sequence Excitation. *J. Phys. Chem. C* **117**, 22369–22376. ISSN: 1932-7447 (Oct. 2013) (cit. on pp. 13, 16, 41, 47).
17. VOLKOVICH, R. & PESKIN, U. Transient dynamics in molecular junctions: Coherent bichromophoric molecular electron pumps. *Phys. Rev. B* **83**, 033403 (Jan. 2011) (cit. on p. 13).
18. PLATERO, G. & AGUADO, R. Photon-assisted transport in semiconductor nanostructures. *Physics Reports* **395**, 1–157. ISSN: 0370-1573 (May 2004) (cit. on pp. 13, 51).
19. GALPERIN, M. Photonics and spectroscopy in nanojunctions: a theoretical insight. *Chem. Soc. Rev.* **46**, 4000–4019 (13 2017) (cit. on p. 13).
20. KOHLER, S., LEHMANN, J. & HÄNGGI, P. Driven quantum transport on the nanoscale. *Physics Reports* **406**, 379–443. ISSN: 0370-1573 (2005) (cit. on p. 13).
21. STEFANUCCI, G. & van LEEUWEN, R. *Nonequilibrium Many-Body Theory of Quantum Systems* 620. ISBN: 9780521766173 (Mar. 2013) (cit. on p. 13).

22. NOVICENKO, V., ANISIMOVAS, E. & JUZELIUSAS, G. Floquet analysis of a quantum system with modulated periodic driving. *Phys. Rev. A* **95**, 023615 (2 Feb. 2017) (cit. on p. 13).
23. ECKARDT, A. & ANISIMOVAS, E. High-frequency approximation for periodically driven quantum systems from a Floquet-space perspective. *New Journal of Physics* **17**, 093039 (2015) (cit. on p. 13).
24. KWONG, N.-H. & BONITZ, M. Real-Time Kadanoff-Baym Approach to Plasma Oscillations in a Correlated Electron Gas. *Phys. Rev. Lett.* **84**, 1768–1771 (8 Feb. 2000) (cit. on p. 13).
25. GAO, Y. & GALPERIN, M. Simulation of optical response functions in molecular junctions. *The Journal of Chemical Physics* **144**, 244106 (2016) (cit. on p. 13).
26. WALSCHAERS, M., MULET, R. & BUCHLEITNER, A. Scattering theory of efficient quantum transport across finite networks. *Journal of Physics B: Atomic, Molecular and Optical Physics* **50**, 224003 (2017) (cit. on p. 13).
27. GASPARD, P. Scattering theory and thermodynamics of quantum transport. *Annalen der Physik* **527**, 663–683 (cit. on p. 13).
28. KNEZEVIC, I. & FERRY, D. K. Evolution of the reduced density matrix: a generalized projection-operator approach. *Microelectronic Engineering* **63**. 5th International Symposium on New Phenomena in Mesoscopic Structure, 105–108. ISSN: 0167-9317 (2002) (cit. on p. 13).
29. ÖZPINECI, A., LEITNER, D. M. & CIRACI, S. Reduced density matrix approach to phononic dissipation in friction. *Phys. Rev. B* **62**, 10558–10564 (15 Oct. 2000) (cit. on p. 13).
30. ZHENG, X., CHEN, G., MO, Y., *et al.* Time-dependent density functional theory for quantum transport. *eng. J Chem Phys* **133**, 114101. ISSN: 1089-7690 (Sept. 2010) (cit. on p. 13).
31. HUTZEN, R., WEISS, S., THORWART, M., *et al.* Iterative summation of path integrals for nonequilibrium molecular quantum transport. *Phys. Rev. B* **85**, 121408 (Mar. 2012) (cit. on p. 13).
32. HARTLE, R., COHEN, G., REICHMAN, D. R., *et al.* Decoherence and lead-induced interdot coupling in nonequilibrium electron transport through interacting quantum dots: A hierarchical quantum master equation approach. *Phys. Rev. B* **88**, 235426 (Dec. 2013) (cit. on p. 13).
33. JAUHO, A.-P., WINGREEN, N. S. & MEIR, Y. Time-dependent transport in interacting and noninteracting resonant-tunneling systems. *Phys. Rev. B* **50**, 5528–5544 (Aug. 1994) (cit. on pp. 13, 14, 18, 30).
34. LUDOVICO, M. F., MOSKALETS, M., SÁNCHEZ, D., *et al.* Dynamics of energy transport and entropy production in ac-driven quantum electron systems. *Phys. Rev. B* **94**, 035436 (3 July 2016) (cit. on p. 13).

35. LUDOVICO, M. F., LIM, J. S., MOSKALETS, M., *et al.* Dynamical energy transfer in ac-driven quantum systems. *Phys. Rev. B* **89**, 161306 (16 Apr. 2014) (cit. on p. 13).
36. KRYACHKO, E. S. & LUDEÑA, E. V. Density functional theory: Foundations reviewed. *Physics Reports* **544**. Density functional theory: Foundations reviewed, 123–239. ISSN: 0370-1573 (2014) (cit. on p. 13).
37. COHEN, A. J., MORI-SÁNCHEZ, P. & YANG, W. Challenges for Density Functional Theory. *Chemical Reviews* **112**. PMID: 22191548, 289–320 (2012) (cit. on p. 13).
38. LIEBMAN, J. F. A Review of “Time-Dependent Density-Functional Theory: Concepts and Applications”. *Molecular Crystals and Liquid Crystals* **569**, 165–166 (2012) (cit. on p. 13).
39. BURKE, K., WERSCHNIK, J. & GROSS, E. K. U. Time-dependent density functional theory: Past, present, and future. *The J. of Chemical Physics* **123**, 062206 (2005) (cit. on p. 13).
40. JASKOLSKI, W. & AYUELA, A. Coulomb edge effects in graphene nanoribbons. *Solid State Communications* **196**, 1–7. ISSN: 0038-1098 (2014) (cit. on p. 13).
41. BELTAKO, K., MICHELINI, F., CAVASSILAS, N., *et al.* Dynamical photo-induced electronic properties of molecular junctions. *The J. of Chemical Physics* **148**, 104301 (2018) (cit. on pp. 13, 69).
42. GALPERIN, M., RATNER, M. A. & NITZAN, A. Raman scattering in current-carrying molecular junctions. *eng. J Chem Phys* **130**, 144109. ISSN: 1089-7690 (Apr. 2009) (cit. on p. 13).
43. OCHOA, M. A., SELZER, Y., PESKIN, U., *et al.* Pump–Probe Noise Spectroscopy of Molecular Junctions. *J. Phys. Chem. Lett.* **6**, 470–476. ISSN: 1948-7185 (Feb. 2015) (cit. on p. 13).
44. WHITE, A. J., FAINBERG, B. D. & GALPERIN, M. Collective Plasmon-Molecule Excitations in Nanojunctions: Quantum Consideration. *J. Phys. Chem. Lett.* **3**, 2738–2743. ISSN: 1948-7185 (Oct. 2012) (cit. on p. 13).
45. GAURY, B., WESTON, J., SANTIN, M., *et al.* Numerical simulations of time-resolved quantum electronics. *Physics Reports* **534**, 1–37. ISSN: 0370-1573 (Jan. 2014) (cit. on pp. 14, 15, 17, 28, 31, 32, 45).
46. COCKER, T. L., JELIC, V., GUPTA, M., *et al.* An ultrafast terahertz scanning tunnelling microscope. *en. Nat Photon* **7**, 620–625. ISSN: 1749-4885 (Aug. 2013) (cit. on p. 14).
47. PIVRIKAS, A., SARICIFTCI, N. S., JUSKA, G., *et al.* A review of charge transport and recombination in polymer/fullerene organic solar cells. *en. Prog. Photovolt: Res. Appl.* **15**, 677–696. ISSN: 1099-159X (Dec. 2007) (cit. on p. 14).



48. BRAUER, J. C., MARCHIORO, A., PARAECATTIL, A. A., *et al.* Dynamics of Interfacial Charge Transfer States and Carriers Separation in Dye-Sensitized Solar Cells: A Time-Resolved Terahertz Spectroscopy Study. *J. Phys. Chem. C* **119**, 26266–26274. ISSN: 1932-7447 (Nov. 2015) (cit. on p. 14).
49. BAKULIN, A. A., NEUTZNER, S., BAKKER, H. J., *et al.* Charge Trapping Dynamics in PbS Colloidal Quantum Dot Photovoltaic Devices. *ACS Nano* **7**, 8771–8779. ISSN: 1936-0851 (Oct. 2013) (cit. on p. 14).
50. GABOR, N. M., ZHONG, Z., BOSNICK, K., *et al.* Ultrafast Photocurrent Measurement of the Escape Time of Electrons and Holes from Carbon Nanotube *p-i-n* Photodiodes. *Phys. Rev. Lett.* **108**, 087404 (8 Feb. 2012) (cit. on p. 14).
51. BAKULIN, A. A., SILVA, C. & VELLA, E. Ultrafast Spectroscopy with Photocurrent Detection: Watching Excitonic Optoelectronic Systems at Work. *J. Phys. Chem. Lett.* **7**, 250–258. ISSN: 1948-7185 (Jan. 2016) (cit. on p. 14).
52. JAKOWETZ, A. C., BOHM, M. L., ZHANG, J., *et al.* What Controls the Rate of Ultrafast Charge Transfer and Charge Separation Efficiency in Organic Photovoltaic Blends. *J. Am. Chem. Soc.* **138**, 11672–11679. ISSN: 0002-7863 (Sept. 2016) (cit. on p. 14).
53. ONO, S. & OHNO, K. Minimal model for charge transfer excitons at the dielectric interface. *Phys. Rev. B* **93**, 121301 (Mar. 2016) (cit. on p. 14).
54. PRINS, F., BUSCEMA, M., SELDENTHUIS, J. S., *et al.* Fast and Efficient Photodetection in Nanoscale Quantum-Dot Junctions. *Nano Lett.* **12**, 5740–5743. ISSN: 1530-6984 (Nov. 2012) (cit. on p. 14).
55. ALSULAMI, Q. A., MURALI, B., ALSINAN, Y., *et al.* Remarkably High Conversion Efficiency of Inverted Bulk Heterojunction Solar Cells: From Ultrafast Laser Spectroscopy and Electron Microscopy to Device Fabrication and Optimization. en. *Adv. Energy Mater.* **6**, n/a–n/a. ISSN: 1614-6840 (June 2016) (cit. on p. 14).
56. MICHELINI, F., CREPIEUX, A. & BELTAKO, K. Entropy production in photovoltaic-thermoelectric nanodevices from the non-equilibrium Green's function formalism. en. *J. Phys.: Condens. Matter* **29**, 175301. ISSN: 0953-8984 (2017) (cit. on p. 14).
57. NEMATİ ARAM, T., ANGHEL-VASILESCU, P., ASGARI, A., *et al.* Modeling of molecular photocells: Application to two-level photovoltaic system with electron-hole interaction. *The J. of Chemical Physics* **145**, 124116. ISSN: 0021-9606 (Sept. 2016) (cit. on p. 14).

58. NEMATI ARAM, T., ERNZERHOF, M., ASGARI, A., *et al.* The impact of long-range electron-hole interaction on the charge separation yield of molecular photocells. *The J. of Chemical Physics* **146**, 034103. ISSN: 0021-9606 (Jan. 2017) (cit. on p. 14).
59. KUPERMAN, M. & PESKIN, U. Field-induced inversion of resonant tunneling currents through single molecule junctions and the directional photoelectric effect. *The J. of Chemical Physics* **146**, 092314. ISSN: 0021-9606 (Jan. 2017) (cit. on pp. 14, 47, 59).
60. HERTEL, I. V. & RADLOFF, W. Ultrafast dynamics in isolated molecules and molecular clusters. en. *Rep. Prog. Phys.* **69**, 1897. ISSN: 0034-4885 (2006) (cit. on p. 14).
61. COMPTON, R., FILIN, A., ROMANOV, D. A., *et al.* Dynamic Rabi sidebands in laser-generated microplasmas: Tunability and control. *Phys. Rev. A* **83**, 053423 (May 2011) (cit. on pp. 14, 50).
62. COCHRANE, K. A., SCHIFFRIN, A., ROUSSY, T. S., *et al.* Pronounced polarization-induced energy level shifts at boundaries of organic semiconductor nanostructures. en. *Nature Communications* **6**, 8312. ISSN: 2041-1723 (Oct. 2015) (cit. on p. 14).
63. CAVASSILAS, N., MICHELINI, F. & BESCOND, M. Modeling of nanoscale solar cells: The Green's function formalism. *J. of Renewable and Sustainable Energy* **6**, 011203 (Oct. 2013) (cit. on p. 15).
64. BELTAKO, K., CAVASSILAS, N. & MICHELINI, F. State hybridization shapes the photocurrent in triple quantum dot nanojunctions. English. *Appl. Phys. Lett.* **109**. WOS:000383787400045, 073501. ISSN: 0003-6951 (Aug. 2016) (cit. on p. 15).
65. XIANG, D., WANG, X., JIA, C., *et al.* Molecular-Scale Electronics: From Concept to Function. *Chem. Rev.* **116**, 4318–4440. ISSN: 0009-2665 (Apr. 2016) (cit. on p. 15).
66. EVERS, F. & VENKATARAMAN, L. Preface: Special Topic on Frontiers in Molecular Scale Electronics. *The J. of Chemical Physics* **146**, 092101. ISSN: 0021-9606 (Mar. 2017) (cit. on p. 15).
67. ZHU, X.-Y. Charge Transport at Metal-Molecule Interfaces:- A Spectroscopic View. *The J. of Physical Chemistry B* **108**, 8778–8793 (2004) (cit. on p. 16).
68. DJUKIC, D., THYGESEN, K. S., UNTIEDT, C., *et al.* Stretching dependence of the vibration modes of a single-molecule Pt – H<sub>2</sub> – Pt bridge. *Phys. Rev. B* **71**, 161402 (16 Apr. 2005) (cit. on p. 17).
69. K. NIELSEN, S., NOAT, Y., BRANDBYGE, M., *et al.* Conductance of single-atom platinum contacts: Voltage-dependence of the conductance histogram. *Phys. Rev. Lett.* **67**, 245411 (June 2003) (cit. on p. 17).

70. HEURICH, J., CUEVAS, J. C., WENZEL, W., *et al.* Electrical Transport through Single-Molecule Junctions: From Molecular Orbitals to Conduction Channels. *Phys. Rev. Lett.* **88**, 256803 (25 June 2002) (cit. on p. 17).
71. FALEEV, S. V., LÉONARD, F., STEWART, D. A., *et al.* Ab initio tight-binding LMTO method for nonequilibrium electron transport in nanosystems. *Phys. Rev. B* **71**, 195422 (19 May 2005) (cit. on p. 17).
72. MERA, H., KAASBJERG, K., NIQUET, Y.-M., *et al.* Assessing the accuracy of Kohn-Sham conductances using the Friedel sum rule. **81**, 035110 (Jan. 2010) (cit. on p. 17).
73. THYGESEN, K. S. & RUBIO, A. Conserving GW scheme for nonequilibrium quantum transport in molecular contacts. *Phys. Rev. B* **77**, 115333 (11 Mar. 2008) (cit. on p. 17).
74. CAVASSILAS, N., MICHELINI, F. & BESCOND, M. Multiband quantum transport simulations of ultimate p-type double-gate transistors: Effects of hole-phonon scattering. *Journal of Applied Physics* **109**, 073706 (2011) (cit. on p. 17).
75. CAVASSILAS, N., MICHELINI, F. & BESCOND, M. Modeling of nanoscale solar cells: The Green's function formalism. *Journal of Renewable and Sustainable Energy* **6**, 011203 (2014) (cit. on p. 17).
76. MAHAN, G. D. *Many-Particles Physics* (Physics of Solids and Liquids, 2000) (cit. on pp. 17–19, 22, 23, 25).
77. DATTA, S. *Electronic Transport in Mesoscopic Systems*. Cambridge University Press (2009) (cit. on pp. 18, 19, 23).
78. ANANTRAM, M. P., LUNDSTROM, M. S. & NIKONOV, D. E. Modeling of Nanoscale Devices. *eprint arXiv:cond-mat/0610247*. eprint: [cond-mat/0610247](https://arxiv.org/abs/cond-mat/0610247) (Oct. 2006) (cit. on p. 18).
79. LEE, Y., LANNOO, M., CAVASSILAS, N., *et al.* Efficient quantum modeling of inelastic interactions in nanodevices. *Phys. Rev. B* **93**, 205411 (20 May 2016) (cit. on p. 19).
80. GELL-MANN, M. & LOW, F. Bound States in Quantum Field Theory. *Phys. Rev.* **84**, 350–354 (2 Oct. 1951) (cit. on p. 22).
81. JAUHO, A.-P., WINGREEN, N. S. & MEIR, Y. Time-dependent transport in interacting and noninteracting resonant-tunneling systems. *Phys. Rev. B* **50**, 5528–5544 (8 Aug. 1994) (cit. on p. 25).
82. LAKE, R. & DATTA, S. Nonequilibrium Green's-function method applied to double-barrier resonant-tunneling diodes. *Phys. Rev. B* **45**, 6670–6685 (Mar. 1992) (cit. on p. 28).

83. SETTNER, M., POWER, S. R., LIN, J., *et al.* Patched Green's function techniques for two-dimensional systems: Electronic behavior of bubbles and perforations in graphene. *Phys. Rev. B* **91**, 125408 (Mar. 2015) (cit. on pp. 28, 32).
84. LATINI, S., PERFETTO, E., UIMONEN, A.-M., *et al.* Charge dynamics in molecular junctions: Nonequilibrium Green's function approach made fast. *Phys. Rev. B* **89**, 075306 (7 Feb. 2014) (cit. on p. 28).
85. BRUUS, H. & FLENSBERG, K. *Many-body quantum theory in condensed matter physics - an introduction* (Oxford University Press, United States, 2004) (cit. on p. 31).
86. J.W. HAUG, H. & JAUHO, A.-P. *Quantum Kinetics in Transport and Optics of Semiconductors* (Springer series in solid-state sciences 123, 2008) (cit. on p. 31).
87. BARENCO, A. & DUPERTUIS, M. A. Quantum many-body states of excitons in a small quantum dot. *prb* **52**, 2766–2778 (July 1995) (cit. on p. 34).
88. VOVCHENKO, V., ANCHISHKIN, D., AZEMA, J., *et al.* A new approach to time-dependent transport through an interacting quantum dot within the Keldysh formalism. *J. of Physics: Condensed Matter* **26**, 015306 (2014) (cit. on p. 35).
89. STARKE, R. & KRESSE, G. Self-consistent Green function equations and the hierarchy of approximations for the four-point propagator. *Phys. Rev. B* **85**, 075119 (7 Feb. 2012) (cit. on p. 35).
90. PESKIN, U. & GALPERIN, M. Coherently controlled molecular junctions. *The J. of Chemical Physics* **136**, 044107. ISSN: 0021-9606 (Jan. 2012) (cit. on p. 40).
91. ZHANG, H., MIYAMOTO, Y., CHENG, X., *et al.* Optical field terahertz amplitude modulation by graphene nanoribbons. *Nanoscale* **7**, 19012–19017 (45 2015) (cit. on p. 40).
92. LI, Y., MOL, J., C. BENJAMIN, S., *et al.* Interference-based molecular transistors. **6**, 33686 (July 2016) (cit. on p. 40).
93. BAKULIN, A., LOVRINCIC, R., YU, X., *et al.* Mode-selective vibrational modulation of charge transport in organic electronic devices. **6**, 7880 (Aug. 2015) (cit. on pp. 40, 41, 57).
94. CROY, A. & SAALMANN, U. Propagation scheme for nonequilibrium dynamics of electron transport in nanoscale devices. *Phys. Rev. B* **80**, 245311 (Dec. 2009) (cit. on p. 45).
95. LI, G., FAINBERG, B. D. & SEIDEMAN, T. Optically induced transport through semiconductor-based molecular electronics. *The J. of Chemical Physics* **142**, 154111 (2015) (cit. on pp. 50, 58).

96. PAWAR, A. Y., SONAWANE, D. D., ERANDE, K. B., *et al.* Terahertz technology and its applications. *Drug Invention Today* **5**, 157–163. ISSN: 0975-7619 (2013) (cit. on p. 53).
97. GMACHL, C., FROLOV, S. V., NG, H. M., *et al.* Sub-picosecond electron scattering time for  $\lambda = 1.55 \mu\text{m}$  intersubband transitions in GaN/Al-GaN multiple quantum wells. *Electronics Letters* **37**, 378–380. ISSN: 0013-5194 (Mar. 2001) (cit. on p. 54).
98. CHEN, C., TAO, Z., CARR, A., *et al.* Distinguishing attosecond electron–electron scattering and screening in transition metals. *Proceedings of the National Academy of Sciences* **114**, E5300–E5307 (2017) (cit. on p. 54).
99. KORNBLUTH, M., NITZAN, A. & SEIDEMAN, T. Light-induced electronic non-equilibrium in plasmonic particles. *The J. of Chemical Physics* **138**, 174707 (2013) (cit. on p. 58).
100. GALPERIN, M. & NITZAN, A. Current-Induced Light Emission and Light-Induced Current in Molecular-Tunneling Junctions. *Phys. Rev. Lett.* **95**, 206802 (20 Nov. 2005) (cit. on p. 58).
101. POPESCU, B., WOICZIKOWSKI, P. B., ELSTNER, M., *et al.* Time-Dependent View of Sequential Transport through Molecules with Rapidly Fluctuating Bridges. *Phys. Rev. Lett.* **109**, 176802 (17 Oct. 2012) (cit. on p. 58).
102. KOHLER, S., CAMALET, S., STRASS, M., *et al.* Charge transport through a molecule driven by a high-frequency field. *Chemical Physics* **296**. The Spin-Boson Problem: From Electron Transfer to Quantum Computing ... to the 60th Birthday of Professor Ulrich Weiss, 243–249. ISSN: 0301-0104 (2004) (cit. on p. 58).
103. KOHLER, S., LEHMANN, J. & HÄNGGI, P. Driven quantum transport on the nanoscale. *Physics Reports* **406**, 379–443. ISSN: 0370-1573 (2005) (cit. on p. 58).
104. VASA, P., WANG, W., POMRAENKE, R., *et al.* Real-time observation of ultra-fast Rabi oscillations between excitons and plasmons in metal nanostructures with J-aggregates. **7**, 128–132 (May 2013) (cit. on p. 58).
105. BAKULIN, A. A., RAO, A., PAVELYEV, V. G., *et al.* The Role of Driving Energy and Delocalized States for Charge Separation in Organic Semiconductors. *Science* **335**, 1340–1344. ISSN: 0036-8075 (2012) (cit. on pp. 59, 64).
106. RUDNER, M. S., LINDNER, N. H., BERG, E., *et al.* Anomalous Edge States and the Bulk-Edge Correspondence for Periodically Driven Two-Dimensional Systems. *Phys. Rev. X* **3**, 031005 (3 July 2013) (cit. on p. 59).
107. HILDE D. DE GIER Ria Broer, R. W. A. H. *On the relation between local and charge-transfer exciton binding energies in organic photovoltaic materials* 2015. doi:10.1117/12.2187872. <<https://doi.org/10.1117/12.2187872>> (cit. on p. 61).

108. NEMATİ ARAM, T., ANGHEL-VASILESCU, P., ASGARI, A., *et al.* Modeling of molecular photocells: Application to two-level photovoltaic system with electron-hole interaction. *The Journal of Chemical Physics* **145**, 124116 (2016) (cit. on pp. 61, 73).
109. MIKHENKO, O. V., CORDELLA, F., SIEVAL, A. B., *et al.* Temperature Dependence of Exciton Diffusion in Conjugated Polymers. *The J. of Physical Chemistry B* **112**. PMID: 18729397, 11601–11604 (2008) (cit. on p. 61).
110. K., M. T., A., M. K., A., L. W., *et al.* Connecting Molecular Structure and Exciton Diffusion Length in Rubrene Derivatives. *Advanced Materials* **25**, 3689–3693 (cit. on p. 61).
111. LI, Z., ZHANG, X. & LU, G. Exciton diffusion in disordered small molecules for organic photovoltaics: insights from first-principles simulations. *J. of Physics: Condensed Matter* **26**, 185006 (2014) (cit. on p. 61).
112. GORCZAK, N., SWART, M. & GROZEMA, F. Energetics of charges in organic semiconductors and at organic donor-acceptor interfaces. **2**, 3467–3475 (May 2014) (cit. on pp. 62, 63).
113. CLARKE, T. M. & DURRANT, J. R. Charge Photogeneration in Organic Solar Cells. *Chemical Reviews* **110**. PMID: 20063869, 6736–6767 (2010) (cit. on p. 64).
114. ROLCZYNSKI, B. S., SZARKO, J. M., SON, H. J., *et al.* Effects of Exciton Polarity in Charge-Transfer Polymer/PCBM Bulk Heterojunction Films. *The J. of Physical Chemistry Letters* **5**. PMID: 26273865, 1856–1863 (2014) (cit. on p. 64).
115. DYER-SMITH, C. & NELSON, J. in *Practical Handbook of Photovoltaics (Second Edition)* (eds MCEVOY, A., MARKVART, T. & CASTAÑER, L.) Second Edition, 543–569 (Academic Press, Boston, 2012). ISBN: 978-0-12-385934-1. doi:<https://doi.org/10.1016/B978-0-12-385934-1.00016-7>. <<http://www.sciencedirect.com/science/article/pii/B9780123859341000167>> (cit. on p. 69).
116. UNGER, T., WEDLER, S., KAHLE, F.-J., *et al.* The Impact of Driving Force and Temperature on the Electron Transfer in Donor–Acceptor Blend Systems. *The Journal of Physical Chemistry C* **121**, 22739–22752 (2017) (cit. on pp. 69, 78).
117. VANDEWAL, K., BENDUHN, J., SCHELLHAMMER, K. S., *et al.* Absorption Tails of Donor:C60 Blends Provide Insight into Thermally Activated Charge-Transfer Processes and Polaron Relaxation. *Journal of the American Chemical Society* **139**. PMID: 28068763, 1699–1704 (2017) (cit. on p. 69).
118. KOCHERZHENKO, A. A., LEE, D., FORSUELO, M. A., *et al.* Coherent and Incoherent Contributions to Charge Separation in Multichromophore Systems. *The Journal of Physical Chemistry C* **119**, 7590–7603 (2015) (cit. on p. 69).



119. YANG, L., ZHANG, S., HE, C., *et al.* New Wide Band Gap Donor for Efficient Fullerene-Free All-Small-Molecule Organic Solar Cells. *Journal of the American Chemical Society* **139**. PMID: 28081597, 1958–1966 (2017) (cit. on pp. [69](#), [78](#)).
120. BITTNER, E. R., RAMON, J. G. S. & KARABUNARLIEV, S. Exciton dissociation dynamics in model donor-acceptor polymer heterojunctions. I. Energetics and spectra. *The Journal of Chemical Physics* **122**, 214719 (2005) (cit. on p. [70](#)).
121. WÖRNER, H. J., ARRELL, C. A., BANERJI, N., *et al.* Charge migration and charge transfer in molecular systems. *Structural Dynamics* **4**, 061508 (2017) (cit. on p. [74](#)).
122. SUTTY, S., WILLIAMS, G. & AZIZ, H. Role of the donor material and the donor–acceptor mixing ratio in increasing the efficiency of Schottky junction organic solar cells. *Organic Electronics* **14**, 2392–2400. ISSN: 1566-1199 (2013) (cit. on p. [82](#)).

## ANNEXES



## A. TRLDOS stationary limit

In this appendix, we demonstrate that Eq. (3.7) gives

$$TRLDOS_i(E) = LDOS_i(E) = -\frac{1}{\pi} \text{Im } G_i^r(E)$$

in the stationary limit. For a time-independent problem, Eq. (2.65) reduces to  $\Psi_{\alpha E}(t) = e^{-iEt/\hbar} \Psi_{\alpha E}^{st}$  and time translational invariance implies that two-time statistical functions  $G(t, t')$  only depends on the two-time difference  $(t - t')$ . We thus develop

$$G_i^<(E) = \int d(t - t') e^{+iE(t-t')} G_i^<(t - t')$$

using Eq. (2.68), and we obtain

$$\begin{aligned} G_i^<(E) &= \int \frac{dE'}{2\pi} \sum_{\alpha} i f_{\alpha}(E') \left[ \Psi_{\alpha E'}^{st}(i) \Psi_{\alpha E'}^{st\dagger}(i) \right] \\ &\quad \times \int d(t - t') e^{+i(E-E')(t-t')} \\ &= \sum_{\alpha} i f_{\alpha}(E) \left[ \Psi_{\alpha E}^{st}(i) \Psi_{\alpha E}^{st\dagger}(i) \right]. \end{aligned}$$

Similarly,

$$G_i^>(E) = -\sum_{\alpha} i(1 - f_{\alpha}(E)) \left[ \Psi_{\alpha E}^{st}(i) \Psi_{\alpha E}^{st\dagger}(i) \right].$$

From  $LDOS(E) = -\frac{1}{\pi} \text{Im } G^r(E) = -\frac{1}{2\pi} \text{Im } [G^>(E) - G^<(E)]$ , we conclude

$$LDOS_i(E) = \text{Im} \left[ \frac{i}{2\pi} \sum_{\alpha} \Psi_{\alpha E}(i, t) \Psi_{\alpha E}^{\dagger}(i, t) \right]$$

which does not depend on time, and coincides with the proposed definition of  $TRLDOS$ .

## B. List of publications

- 1 - [Time-resolved quantum transport for optoelectronics](#)  
Conference Paper Dec 2017 2017 IEEE International Electron Devices Meeting (IEDM)  
F. Michelini, K. Beltako, M. Bescond and L. Raymond
- 2 - [Dynamical photo-induced electronic properties of molecular junctions](#)  
Article Sept. 2017 The Journal of Chemical Physics  
K. Beltako, F. Michelini, N.Cavassilas and L. Raymond
- 3 - [Entropy production in photovoltaic-thermoelectric nanodevices from the non-equilibrium Green's function formalism](#)  
Article Oct. 2016 Journal of Physics Condensed Matter 29(17)  
F. Michelini, A. Crépieux and K. Beltako
- 4 - [State hybridization shapes the photocurrent in triple quantum dot nanojunctions](#)  
Article Aug. 2016 Applied Physics Letters 109(7):073501  
K. Beltako, N.Cavassilas and F. Michelini
- 5 - [Energy and entropy currents for nanoscaled optoelectronics](#)  
Conference Paper Mar 2016 SPIE OPTO  
F. Michelini K. Beltako and A. Crépieux
- 6 - [Competitive hybridization in quantum dot-based nanodevices](#)  
Conference Paper Mar 2016 SPIE OPTO  
K. Beltako, N.Cavassilas and F. Michelini
- 7 - [Analyzing energy conversion in nanoscale optoelectronics](#)  
Article Feb 2016 SPIE Newsroom  
F. Michelini K. Beltako and A. Crépieux